ABSTRACT

Title of Document: RETRIEVAL OF ICE CLOUD PARAMETERS USING DMSP SPECIAL SENSOR MICROWAVE IMAGER/SOUNDER.

Ninghai Sun, Doctor of Philosophy, 2010

Directed By: Professor Zhanqing Li, Department of Atmospheric and Oceanic Science

Clouds exert a profound influence on both the water balance of the atmosphere and the earth's radiation budget (Stephens 2005; Stephens and Kummerow 2007). Among the global distribution, 30% of them are ice clouds (Riedi *et al.* 2000). It is important to improve our knowledge of the ice cloud properties in order to determine their influence to the global ecosystem. For ice clouds with millimeter-size ice particles, which are generally found in anvil cirrus and deep convections, microwave and millimeter wave length satellite measurements are suitable for the ice cloud microphysical property retrieval because of its strong ability to penetrate deeper into dense ice clouds. For these types of ice clouds, brightness temperatures at the top of the atmosphere are analytically derived as a function of vertically integrated ice water content (i.e. ice water path), effective particle diameter, and bulk volume density. In general, three brightness temperature measurements are needed to retrieve the three ice cloud microphysical parameters. A two-stream radiative transfer theory was

applied to data from the Advanced Microwave Sounding Unit (AMSU) and the Moisture Humidity Sensor (MHS) in order to generate global ice water paths operationally. This research further applied the model and theory to derive ice water path (IWP) from the Special Sensor Microwave Imager/Sounder (SSMIS) onboard the Defense Meteorological Satellite Program (DMSP) F-16 satellite. Compared to AMSU/MHS, which have field of views (FOV) varying with scan position, SSMIS scans the Earth's atmosphere at a constant viewing angle of 53^{o} and therefore offers a uniform FOV within each scan. This unique feature allows for improved global mapping and monitoring of ice clouds so that a more accurate and realistic IWP and ice particle effective diameter distribution is expected. A direct application of SSMIS-derived ice water path is its relationship with surface rain rate as derived previously for AMSU and MHS instruments. Here, SSMIS-derived rain rate was compared to the AMSU and MHS rainfall products and hourly synthetic precipitation observations from rain gauges and surface radar. Results show that SSMIS surface precipitation distribution is spatially consistent and does not have apparent artificial boundary near coastal zones as previously seen in other algorithms. Also, the ice water path associated with a severe storm reasonably delineates the strong convective precipitation areas and has a spatial variation consistent with surface precipitation. From retrieved instantaneous surface precipitation, a tropical and subtropical oceanic precipitation anomaly time series is constructed from 5 year's worth (2005-2009) of SSMIS data. This data record is also linked to the previous constructed SSM/I 15-year (1992-2006) data record to provide a longer term climate study by satellite observations. In future studies, refined algorithms for the estimate of ice cloud base

temperature and ice particle bulk volume density are going to be developed to improve the accuracy of IWP retrieval under various cloud vertical distributions. Meanwhile, a better inter-sensor cross calibration scheme is the key to make satellite measurements more useful in climate change study.

THE RETRIEVAL OF ICE CLOUD PARAMETERS USING DMSP SPECIAL SENSOR MICROWAVE IMAGER/SOUNDER.

By

Ninghai Sun

Dissertation submitted to the Faculty of the Graduate School of the
University of Maryland, College Park, in partial fulfillment
of the requirements for the degree of
Doctor of Philosophy
2010

Advisory Committee:
Professor Zhanqing Li, Chair
Dr. Fuzhong Weng
Professor Rachel Pinker
Professor Ross J. Salawitch
Professor Robert Hudson
Professor Shunlin Liang

Dedication

I would like to dedicate this Doctoral dissertation to my family. There is no doubt in my mind that without their continued support and counsel I could not have completed this process.

Acknowledgements

My Ph.D training at University of Maryland at College Park has been an exciting and fruitful journey, full of great memories of working with faculty, staff, and students. There is a long list of names I would like to thank. At the top of the list are my thesis advisor and academic research supervisor, Dr. Fuzhong Weng and Professor Zhanqing Li. No words can express my appreciation for their guidance in my work and thesis. During the past years, Dr. Fuzhong Weng and Professor Zhanqing Li not only provided me tremendous support and enthusiasm in my research, but more importantly, also showed me a scrupulous attitude toward scientific research and thea demand for perfection in conducting research, which will benefit me for all my life.

I would like to thank my thesis committee members, Professor Ross J. Salawitch, Rachel Pinker, Robert Hudson, and Shunlin Liang, who dedicated much of their time to read my thesis drafts and give me many valuable comments on my research. Especially, I would like to express my appreciation to Professor Ross J. Salawitch for his constructive suggestions and great insights on my dissertation.

I want to thank my working colleague in NOAA, Dr. Banghua Yan. By discussing and working together, we have successfully implemented and distributed the NOAA/NESDIS DMSP F-16 SSMIS operational recalibration program to external groups. I also want to thank our atmospheric and oceanic science department for providing solid Ph.D training and a stimulating environment for my studies. I also want to thank members in the UMD group for providing the validation data and comments in the final discussion. Additionally, I want to thank all the faculty from

whom I have taken classes and worked with as teaching assistant, and the staff who have made my daily life smooth. I spent the best years of my life within our department full of joy and excitement. Finally, I want to thank my parents and my wife, Yi Huang. Their encouragement, support, and love during the past years have been my solid support, which has kept me warm for completing this journey of pursuing my Ph.D degree.

Table of Contents

List of Tables

List of Figures

Chapter 1: Introduction

Clouds play a vital role in Earth's climate and radiation energy budget, and influence weather and climate prediction through their horizontal and vertical distribution, as well as their optical properties. To understand how clouds affect the climate and vital feedbacks within the Earth system, it is important to study the transfer of radiation through and within clouds. Several satellite experiments, such as the Earth Radiation Budget Experiment (ERBE) (Barkstrom 1984; Barkstrom and Smith 1985) and the Clouds and the Earth's Radiant Energy System (CERES) (Wielicki *et al.* 1996), focused on obtaining quantitative measurements of the instantaneous effects of clouds on the top-of-the-atmosphere (TOA) radiation balance. From 1983 onward, the International Satellite Cloud Climatology Program (ISCCP) (Rossow and Schiffer 1991, 1999) began processing satellite visible (*VIS*) and infrared (*IR*) radiance data, and for the first time provided the global distribution of total cloud cover and related optical properties. These satellite measurements are an important source of information for testing models related to TOA fluxes and other properties of the climate system. However, very limited information is offered by these measurements for understanding the net effects of clouds on atmospheric and surface radiation budgets.

At the TOA, the radiation budget is determined by the net shortwave flux and the outgoing longwave radiation (OLR). The effects of clouds in internally heating and cooling the atmosphere are imbedded in this whole process. Understanding how clouds partition the absorption of radiation between the surface and atmosphere requires a global surface radiation budget climatology, in combination with TOA

fluxes (Stephens 2005). A major limitation in the determination of atmospheric and surface radiation budgets is the lack of cloud input properties and other information needed in radiative transfer calculations. Nevertheless, the growing use of satellite measurements has greatly helped in the estimation of global cloud effects on the radiative budget.

In general, the net thermal effect of clouds occurs as a residual of the cooling associated with reduced solar radiation reaching the surface and the warming of the atmosphere by the absorptive effects of clouds on longwave radiation (Stephens *et al.* 1994; Rossow and Zhang 1995; Zhang *et al.* 1995). Cloud effects may vary over different geographical locations. At low latitudes and compared to clear-sky conditions, clouds heat the atmosphere through the increased absorption of surface upwelling infrared radiation and emission at colder temperatures despite the reduction in solar shortwave radiation reaching the surface due to cloud reflection. Clouds at higher latitudes play almost an opposite role in the radiation budget at the TOA (Rossow and Zhang 1995). Such cloud-related heating/cooling effects enhance the latitudinal temperature gradient and are responsible for the reinforcement of the mean atmospheric meridional circulation. The vertical distribution of clouds is another important factor in determining heating/cooling effects. Compared to clear-sky conditions, high cold clouds tend to warm the atmosphere, particularly at low latitudes, whereas low clouds enhance the cooling of atmosphere, particularly at high latitudes (Slingo and Slingo 1988).

Ice clouds represent 30% of the global cloud distribution (Riedi *et al.* 2000). Based on their formation mechanism, two types of clouds are recognized. One is

cirrus clouds, which are formed by deposition from water vapor forming ice crystals at high altitudes. Due to the sparseness of moisture in the surrounding air, cirrus clouds tend to be very thin. The other commonly observed ice cloud is associated with deep convection. Convective clouds develop because of instability in the boundary layer. An updraft associated with deep convection may raise water vapor from lower levels of the atmosphere to above the freezing level (around -20^{o}C) where ice particles are formed. During this updraft process, liquid phase cloud droplets are also observed. A common characteristic of both ice cloud types is that the cloud-top pressure is lower than 300 mb. However, even with similar cloud-top pressures, their radiative properties are quite different due to their distinctive optical properties. Cirrus clouds have relatively small optical thicknesses and can absorb IR radiation from the lower atmosphere underneath, but they emit radiation at colder temperatures which is a typical greenhouse effect. Cirrus clouds also reflect shortwave solar radiation due to their high albedo, thereby reducing the solar energy reaching the Earth's surface. The net effect is still under debate. Deep convective ice clouds generally have large optical depths because of their large vertical extent. The interaction among ice clouds, the ambient atmosphere, and the surface environment is a major uncertainty in the estimation of the resulting radiative properties. In addition, deep convective clouds are commonly associated with heavy precipitation. Latent heat release and consumption occurring either directly in clouds or in the ensuing precipitation may further complicate any estimation of cloud properties.

Cloud parameterization is an important part of general circulation models (GCM) and global numerical weather prediction (NWP) models when estimating the

impact of clouds on global climate and weather systems. Numerical studies have shown that the net radiative flux largely depends on the optical thickness of clouds (Stephens and Webster 1981; Liou 1986; Stephens 2005). Recent versions of most NWP models now include ice water content (IWC) as a prognostic variable, and provide estimates of this quantity for high-level clouds (Buehler *et al.* 2007; Liou *et al.* 2008). Ice particle size (*De*) is another important quantity used in NWP microphysical parameterizations. It determines the cloud radiative effect per mass and the ice cloud lifetime (through the particle fall speed). Global quantitative measurements of microphysical parameters, vertically integrated cloud ice mass (or ice water path, hereafter *IWP*), and ice particle size in ice clouds are critical for the validation of global climate models as well as for understanding the nature of climate change.

Many earlier studies focused on better understanding cirrus cloud properties (Liou 1986; Stone *et al.* 1990; Fu and Liou 1993; Minnis *et al.* 1993a; Evans *et al.* 1998; Mace *et al.* 2001; Heymsfield *et al.* 2002; Mace *et al.* 2005). In these studies, cirrus cloud microphysical and bulk properties, as well as their climate impacts, were explored using observations from different satellites, surface radars, and lidars. Results demonstrated that the parameterization of cirrus cloud radiative properties in GCMs and NWP models may significantly help improve simulation accuracy and prediction ability.

The retrieval of deep convective cloud ice parameters as well as studies of their climate impacts have also been broadly examined (Spencer *et al.* 1983; Hakkarinen and Adler 1988; Vivekanandan *et al.* 1991; Evans and Stephens 1995b;

Liu and Curry 1998; Deeter and Evans 2000; Weng and Grody 2000; Zhao and Weng 2002; Evans *et al.* 2005). Due to the much larger optical depth of such clouds, as described earlier, different methodologies and algorithms needed to be developed to help resolve the difficulties faced in retrievals of deep convective cloud ice parameters. For example, deep convection is generally associated with severe or damaging storms where heavy precipitation is observed. It is important to distinguish the ice particle scattering effect from liquid water emission effects when they are mixed together because their radiative impacts offset each other. In addition, in 50-60% of cases, there is the coexistence of multiple layers of clouds (Hahn *et al.* 1982; Warren *et al.* 1985; Tian and Curry 1989), which may further complicate the situation (Chang and Li 2005a). However, as more advanced instrumentation is installed on new satellites, it is possible for the community to improve the understanding of deep convective ice cloud properties using more extensive and accurate observational information.

In this study, deep convective ice cloud parameters, including *IWP* and precipitation-sized ice particle effective diameter (*De*), will be retrieved by simplifying the radiative transfer model using a one-layer two-stream assumption (Weng and Grody 2000). The retrieval algorithm will be then applied to a new-generation conically scanning microwave instrument, the Special Sensor Microwave Imager/Sounder (SSMIS), onboard the Defense Meteorological Satellite Program (DMSP) F-16 satellite. It should be mentioned that this is the first time that a conically scanning instrument has included microwave channels from 19 to 183.31 GHz with temperature and water vapor sounding capabilities. Two channels at 91.655

GHz and 150/183.31 ± 6.6 GHz will be used for the study of ice cloud parameters. At these two channels, the optical impact of cirrus ice particles is negligible due to their relatively smaller particle size with respect to the wavelength. Furthermore, these wavelengths can penetrate fairly deeply into convective clouds, where the majority of precipitation-sized ice particles exist and where the effect of surface radiation is minimal. Such features make these two microwave channels suitable candidates for deep convective ice cloud parameter retrievals. In this retrieval algorithm, both *IWP* and D_e are retrieved simultaneously from dual millimeter-wavelength measurements for a given particle bulk volume density ρ_{ice}. This algorithm has been made operational for generating IWP from the Advanced Microwave Sounding Unit (AMSU) and the moisture humidity Sounder (MHS) and has proven effective in the estimation of deep convection ice particle properties (Zhao and Weng 2002; Weng *et al.* 2003). The surface rainfall rate (*RR*) from deep convective clouds can also be derived based on its correlation with ice scattering. Case studies suggested that the *RR* algorithm performs well, particularly for heavy precipitation associated with severe or damaging weather conditions, such as with hurricanes and squall lines. It is also important to note that the rainfall rate of deep convective clouds involves mostly liquid phase drops, which are common over the western Pacific Ocean warm pool. So rainfall rate might not be accurately retrieved because the *IWP/De* retrieval algorithm is a scattering-based approach and liquid cloud droplets are more emissive than scattering.

This dissertation is organized as follows. First, a detailed review is given regarding the historical development of ice cloud parameter retrievals using different

spectral emission regions. A brief introduction to the DMSP SSMIS instrument is then presented. To provide quality retrievals, the SSMIS temperature data record (TDR) is then evaluated for its accuracy and calibrated in order to remove instrument contamination. An assessment of SSMIS imaging channels at lower frequencies is made by comparing SSMIS-derived products to those from the DMSP F-15 satellite. A two-stream radiative transfer approximation is presented with detailed retrieval steps and case studies, followed by discussion of the retrieval of ice cloud parameters To evaluate the retrieval quality, results from error analyses and validation will be presented. The rainfall rate retrieval algorithm which is based on correlation between rainfall rate and ice scattering will also be presented. SSMIS rainfall rate retrievals are then going to be used for the construction of global precipitation climate data records (CDR) for climate change analysis.

The quality of SSMIS data at all imaging and window channels will be qualitatively assessed by comparing the SSMIS-derived products with those from the heritage SSM/I retrieval algorithms.

Chapter 2: Review of Ice Cloud Parameter Retrievals

Global measurements of ice cloud parameters are best determined from satellite platforms because of their high altitude and wide spatial coverage. Many studies regarding the remote sensing of ice clouds at various wavelengths for the purpose of inferring ice cloud optical and microphysical properties have been conducted.

The ice-phase microphysical process in a cloud is greatly complicated by the variety of forms of the ice phase, as well as by the numerous physical processes that determine the crystal forms (Rogers and Yau 1989). Ice crystals might form once a cloud extends to altitudes where the temperature is colder than 0^{o}C. There are two phase transitions leading to ice formation. One is the freezing of a liquid droplet, and the other is direct deposition of vapor to the ice phase. Both homogeneous and heterogeneous nucleation of ice crystals is possible in either phase transition.

Homogeneous freezing of ice from a pure liquid droplet is analogous to the nucleation of liquid in the vapor phase. Theoretical and empirical results indicate that droplets will freeze spontaneously at temperatures lower than about -35 to -40^{o}C, depending somewhat on the size of the drops being subjected to the low temperature. Theoretical estimates confirm that the homogeneous deposition nucleation process only occurs at temperatures below -65^{o}C and at supersaturation levels around 1000%. These conditions cannot be simultaneously met in natural clouds so this process does not exist in practice. Observations confirm that appreciable numbers of ice crystals usually appear in a cloud at temperatures between 0^{o}C and -40^{o}C. Since

homogeneous nucleation does not occur in this temperature range, the crystals are considered to be formed by heterogeneous processes. Water in contact with most materials freezes at temperatures warmer than -40^{o}C, while deposition occurs on most surfaces at supersaturating and supercooling levels less than the homogeneous nucleation values. Thus the probability of heterogeneous nucleation of freezing or deposition depends strongly on supersaturating and supercooling levels as well as on the properties of the foreign material that triggers the formation of ice crystals. Nucleation mechanisms include condensation nucleation, immersion freezing, contact nucleation, and deposition nucleation. A given particle might nucleate in different ways, depending on the ambient conditions and its history in the cloud. Thus it is difficult to distinguish between the four nucleation processes.

Once ice crystals are nucleated through some mechanism, they then grow in one of the following ways: (1) by riming if relatively large crystals experience collision-coalescence processes with super cooled liquid cloud droplets; or (2) by aggregation if collision and coalescence happens among ice crystals; or (3) by vapor deposition if the environment is supersaturated with respect to ice. Some observations confirm that ice particle concentration may be orders of magnitude greater than the number of ice nuclei due to ice enhancement processes. The strongest contender for an ice enhancement process in clouds is one that involves water droplets freezing. When a supercooled droplet collides with an ice particle, it is possible for liquid water to be trapped in the interior of the droplet and to form an ice shell over the surface of the droplet. Water expands as it freezes so may crack the ice shell, t creating numerous small ice splinters. This is the reason why ice clouds associated with high

liquid water content (LWC) generally have high ice particle concentrations. On the other hand, thin cirrus clouds have very low LWC at high altitudes so ice particle growth occurs through vapor deposition and aggregation among particles. Low ice particle concentrations are quite common in thin cirrus compared to other water-ice mixed cumulus clouds. Additionally, with different ambient temperatures and water vapor contents, an ice crystal can also grow into different shapes, such as hexagonal plates, columns, dendrites, and so on. During some stage of the riming process, the original shape of the ice crystal may disappear and this rimed particle is called graupel. In vigorous convective clouds containing high LWC, riming can produce hailstones varying in size from several millimeters to centimeters. So-called spongy hailstones are commonly formed and contain ice particles with different densities.

The wide range of ice particle shapes, sizes, densities, and mixed liquid water contents may greatly affect ice cloud optical properties at different wavelengths. Thus different remote sensing methods at different sensing frequencies must be developed in order to correctly retrieve ice cloud parameters. Visible or IR frequencies are most useful for measuring particles with sizes on the order of tens of micrometers; millimeter frequencies are not able to detect ice particles at such small sizes because of the larger wavelength. However, for thick anvil cirrus or the upper portions of deep convective clouds that generally contain larger particles such as graupel and hail, microwave channels are more suitable for retrievals. The larger wavelengths make it possible to penetrate deep into clouds for cloud microphysical information while visible and IR channels reach their optical limitations under these circumstances.

Therefore, it is critical to carefully select remote sensing bands and sensing modes when inferring cloud microphysics for different cloud types.

In this chapter, a brief review of past work done concerning ice cloud parameter retrievals is presented and categorized according to spectral band(s) and sensing mode (passive/active). Advantages and limitations of each category are also summarized to emphasize the importance of channel selections for different ice cloud types.

(a) Passive Visible (*VIS*)/Infrared (*IR*) Bands

Measurements at 0.75 μm (visible - *VI S*) and at 2.76 μm (near-infrared – *nIR*) are used to infer cloud properties (Nakajima and King 1990). The Moderate Resolution Imaging Spectroradiometer (MODIS) on board the National Aeronautics and Space Administration (NASA) Earth Observing System (EOS) Terra and Aqua platforms (Minnis *et al.* 1993b; Rolland *et al.* 2000; King *et al.* 2003; Platnick *et al.* 2003)measures reflected solar radiances at 0.75 and 2.16 μm. These radiances are linked to the optical thickness and effective particle radius of optically thick stratiform clouds through the principle that the reflection function of clouds at non-absorbing channels in the visible wavelength region is primarily a function of cloud optical depth, whereas the reflection function at water (or ice) absorbing channels in the near-infrared wavelength region is a function of cloud particle size. This principle does not apply well to optically thin clouds.

To resolve the cloud overlap problem in ice cloud parameter retrievals, a new method (Chang and Li 2005a, b) was developed to effectively detect cirrus over water

clouds using Terra/MODIS CO_2-slicing channels and the visible (0.65 μm) and infrared (11 μm) window channels. The results, after preliminary validation, indicate that this new dual-layer algorithm can overcome some major shortcomings of the conventional single-layer algorithms and can provide more accurate information about cloud-layer structure.

The International Satellite Cloud Climatology Project (ISCCP) (Rossow and Schiffer 1991, 1999) attempts to provide a global spatial and temporal distribution of clouds by using several geostationary and polar-orbiting satellites that measure radiances from clouds in the visible and thermal infrared (*IR*) channels. In the ISCCP cloud analysis procedure, the image pixels are first separated into cloudy and clear scenes by the cloud algorithm. Radiances from each scene are then compared to calculations from a radiative transfer model that simulates radiances that should be measured by satellites as a function of surface visible reflectance and temperature (clear scenes), and cloud optical thickness and cloud-top temperature (cloudy scenes). The key assumption used in detecting cloudy pixels is that radiances in clear scenes are less variable than in cloudy scenes and that it is the clear scenes that compose the "darker" and "warmer" parts of the *VIS* and *IR* radiance distributions, respectively. After estimates of clear radiances are obtained for each place and time, the entire radiance data set is re-examined and each radiance value is compared to its corresponding clear value. The differences are compared to the uncertainties in estimating the clear radiances: if the differences are larger than the uncertainty and in the "cloudy direction" at either wavelength (colder *IR* or brighter *VIS*), then the pixel is labeled cloudy. The measured radiance of each identified pixel is then compared to

the radiative transfer model calculations that include the effects of the atmosphere, surface, and clouds. However, the restriction of satellite-measured radiances to two wavelengths limits the number of parameters that can be determined from the observations. Clouds represented in the model simulation are assumed to be single thin layers uniformly covering the image pixel and composed of droplets with a specified average size and size distribution. Therefore, the retrieved optical thickness and temperature parameters in the ISCCP dataset are not adequate in providing accurate cirrus cloud ice water content (*IWC*) information.

The character of these *VIS/nIR/IR* frequency channel measurements limits their capability of addressing some key issues. For example, it is difficult to distinguish ice from water cloud optical depth using only *VIS/IR* channels. Also, due to the high land emissivity, low optical depth clouds cannot be measured over brighter land surfaces. Additionally, these solar reflection methods only work during daytime. Solar techniques can only retrieve particle sizes near cloud tops, leading to overestimation of the *IWP* due to the small particle size, and are highly sensitive to non-spherical particle shapes because of back- and side-scattering effects. Therefore, a number of gross assumptions about ice particle shape, size distribution, and cloud spatial homogeneity are required to convert radiances to optical depths to *IWP*.

(b) Passive Infrared (*IR*) Band

The data from multichannel imagery sources, particularly the Advanced Very High Resolution Radiometer (AVHRR) onboard the National Oceanic and Atmospheric Administration (NOAA) operational satellites as well as other similar

channels, are also widely used to retrieve cirrus cloud parameters (Szejwach 1982; Pollinger and Wendling 1984; Runheng and Liou 1984; Arking and Childs 1985; Inoue 1985; Wu 1987; Ackerman and Smith 1990; Liou *et al.* 1990; Stone *et al.* 1990; Ou *et al.* 1993; Ou *et al.* 1995; Giraud *et al.* 1997; Ou *et al.* 1999; Stubenrauch *et al.* 1999). These thermal infrared methods use the brightness temperature difference between different AVHRR IR channels to simultaneously determine cirrus cloud-top temperature, IR effective emissivity, mean effective particle size, and optical depth. In addition to AVHRR *IR* channels, Geostationary Operational Environmental Satellite (GOES) channels, such as the 3.9 μm and 12.7 μm bands, are used to build relationships between this brightness temperature difference and optical depth, as well as microphysics. However, some methods, like using single-channel data to infer the optical depth, require the estimation of both cloud-base radiance and cloud emission from external data sources such as from radiosondes and lidars. Ice crystal sizes cannot be determined from this kind of retrieval. Some bi-spectral methods make use of the brightness temperature difference from multiple channels that are least affected by the presence of water vapor, i.e. 3.7 and 10.9 μm channels, to derive the effective distinction ratio, which is a function of ice crystal size distribution. Ice water path (*IWP*) can then be estimated. However, thermal infrared methods easily saturate for moderate optical depths and can only determine particle size (and hence *IWP*) for small crystal sizes. In addition, thermal infrared techniques require accurate knowledge of cloud temperature.

(c) Passive Microwave Band

Millimeter-wave and sub-millimeter-wave ice cloud remote sensing techniques have been developed over the past decades (Vivekanandan *et al.* 1991; Evans and Stephens 1995b; Liu and Curry 2000; Weng and Grody 2000; Evans *et al.* 2005). A theoretical study on the sensitivity of frequencies up to 410 GHz to water vapor, precipitation, and liquid and ice clouds was performed (Gasiewski 1992). The theoretical investigations were then extended by considering non-spherical ice particles at frequencies up to 340 GHz. This showed that the brightness temperature depression depends strongly on particle size and ice water path (Evans and Stephens 1995b). It is also shown that retrievals of both particle size and ice water path could be done with multiple widely-spaced frequencies. In another theoretical study, brightness temperatures up to 880 GHz from observed particle size distributions and several non-spherical ice particle shapes were modeled (Evans *et al.* 1998). This study considered the fact that there is absorption by water vapor, and proposed a method to use the 183-GHz frequency band with matched water vapor transmission to provide the upwelling atmospheric emission background. A simple two-channel algorithm based on brightness temperature depression was used to estimate retrieval errors due to particle shape and size distribution. However, the study did not consider the variability of the height of ice clouds, vertically non-uniform cirrus clouds, liquid water clouds, or atmospheric variability. Thus, the results were not accurate. Observational studies (Wilheit *et al.* 1982; Wu and Weinman 1984; Hakkarinen and Adler 1988; Spencer *et al.* 1989; Adler *et al.* 1990; Liu and Curry 1998; Bennartz and Bauer 2003) have shown that the brightness temperature near 85 GHz is strongly depressed due to the presence of precipitation- sized ice particles. A time-dependent

cloud model was used to examine the temporal evolution of the cloud droplet size distribution and its impact on the microwave brightness temperature (Mugnai and Smith 1988). Further simulations show that the scattering process is also very sensitive to the distribution of the ice particle size (Mugnai and Smith 1988; Smith and Mugnai 1988; Evans and Stephens 1995a; Evans *et al.* 2005). Brightness temperatures simulated at millimeter to sub- millimeter wavelengths are found to be very sensitive to ice clouds having a relatively low *IWP* (Gasiewski 1992; Evans and Stephens 1995b). Measurements made at 150, 220, and 340 GHz display different spatial characteristics for non-raining anvil cirrus and precipitating clouds, while both visible and thermal infrared measurements show very little variations within the clouds (Heymsfield *et al.* 1996; Weng *et al.* 1997).

Compared to *VIS/IR* techniques, microwave radiometers offer a number of potential advantages for measuring *IWP.* They can penetrate deep into dense clouds and provide more information for the estimation of ice cloud bulk properties, especially for precipitation-sized ice particles commonly associated with deep convective cloud systems. Microwave radiation interacts with ice particles primarily through scattering so that emission and cloud temperatures are relatively unimportant. The microwave emission emerging from a precipitating cloud top and lying in a radiometer's field of view (*FOV*) represents the culmination of a complex interaction between emitted microwave radiation and its ongoing extinction through overlapping regions of liquid, melting phase, and ice. Since most ice clouds are above the absorbing part of the atmosphere, they simply modulate the upwelling microwave radiation from below. Furthermore, microwave radiative transfer is linear in behavior

so the signal is directly proportional to optical depth and cloud spatial inhomogeneity effects are less important. The effects of particle shape and size distribution are also important for microwave remote sensing of ice clouds because they determine the relation between optical depth and *IWP*. They are more amenable to calculation because the particle sizes are comparable to or smaller than the wavelength. Microwave methods are also complementary to *VIS* and *IR* methods, in that microwave radiation is sensitive to larger ice crystals and to thicker cloud layers, whereas *VIS/IR* radiation is more sensitive to smaller particles and ice clouds with low *IWP*.

Vivekanandan (1991) quantitatively inferred microphysical parameters through simulations of brightness temperatures at 37 and 85 GHz. The possibility of using the brightness temperature difference between these two frequencies to estimate integrated ice water path was investigated and it was found that brightness temperatures monotonically decrease as the cloud microwave optical thickness increases. However, the relationship between *IWP* and brightness temperature difference may also change due to the variation of particle bulk densities. In addition, over convective cores, both the 37 and 85 GHz weighting functions may peak higher into the ice region due to stronger scattering by the largest ice particles, thereby underestimating the total ice water path. For *IWP* greater than 1 g/m^3, a simple ice exponential size distribution with bulk ice density independent of size, and with fixed limits of integration independent of the ice content present, does not characterize well many ice characteristics. The ice crystal size distribution also plays a key role in their methodology because of its influence on scattering processes. The two channels must

also have the same viewing angle because the scattering effects are closely dependent upon this condition. It has also been shown that the sensitivity of brightness temperatures at sub-millimeter frequencies to *IWP* is nearly independent of cloud temperature and the details of the underlying atmosphere due to the higher scattering effects.

To provide a theoretical understanding of the microwave signatures for ice clouds, the relation between brightness temperature and the similarity parameter and transmittance was studied using simulated data (Weinman and Schols 1992). However, no elaboration on how the relationship can be used for satellite remote sensing of ice clouds was presented.

Upper tropospheric (UT) ice water contents are also retrieved from Earth Observing System Microwave Limb Sounder (EOS MLS) measurements on the Aura platform (launched on July 15, 2004) (Wu *et al.* 2006; Read *et al.* 2007; Wu *et al.* 2008). In the retrieval algorithm, the difference between measured radiance and model-estimated clear-sky radiance at different pressure levels is used to flag cloud conditions. The UT IWC is then retrieved from an empirical relationship constructed from the results of 1-D cloudy-sky radiative transfer simulations. However, their retrieval is largely dependent on how accurately the model identifies cloud conditions. Because the retrieval is only made from 240 GHz observations at pressures lower than 215 hPa, retrieval of ice water content with large ice particles associated with deep convection may easily be saturated because of its optical limit. Studies using MLS measurements (Su *et al.* 2006a) have discovered that UT ice water content associated with deep convection increases sharply with sea surface

temperature (SST), when SST is over 300 K. Meanwhile, UT water vapor rises as ice water content increases, leading to an enhanced positive water vapor feedback. Both European Center for Medium-Range Weather Forecast (ECMWF) analysis and simulations from atmosphere-ocean coupled general circulation models (GCMs) support the existence of such correlations (Su *et al.* 2006b). However, the lack of an onboard calibration system in EOS MLS (Cofield and Stek 2006) cannot provide real time instrument performance monitoring and may introduce uncertainties in the application of the data, particularly when sunlight directly illuminates the antenna in each orbit.

The Millimeter-wave Imaging Radiometer (MIR) (Racette *et al.* 1996) with frequencies at 89, 150, 183, and 220 GHz is used to derive IWP (Liu and Curry 1998, 1999; Deeter and Evans 2000; Weng and Grody 2000). The IWP and particle size in tropical cirrus anvils are retrieved using the MIR channel combinations of 150/220 GHz and 89/150 GHz (Liu and Curry 1998). Some significant brightness temperature depressions were observed from Arctic cirrus using a new channel at 340 GHz (Wang *et al.* 2001). The algorithm is modified further to derive IWP in tropical cloud systems using satellite microwave data (Liu and Curry 1999). Although the *IWP* algorithm works well for cirrus clouds in the tropics, an uncertainty arises due to the unknown particle size. Weng and Grody (2000) proposed an algorithm to derive both IWP and ice particle effective diameter (*De*) using dual millimeter wavelength measurements. For a given particle bulk volume density, the brightness temperature at microwave frequencies can be uniquely related to *IWP* and *De* through a two-stream radiative transfer model solution. The algorithm was tested with

measurements obtained from MIR and the Advanced Microwave Sounding Unit (AMSU) (Zhao and Weng 2002). The retrieved *IWP* and *De* display a reasonable spatial distribution comparable to radar and infrared measurements.

(d) Active Cloud Radar and Lidar

Radar technology is also widely used for remotely sensing cloud microphysical parameters. It can provide long-term higher resolution measurements of cloud properties. However, radars measure the equivalent reflectivity factor (Ze) of cloud properties, but not the mass. The accuracy of the retrieved ice mass or ice precipitation rates from radar reflectivity is highly dependent on the algorithms used. These algorithms are usually developed on the basis of *in situ* observations or ground measurements, or in combination with radar and *in situ* measurements. The development of a parameterization based on both radar and aircraft *in situ* data is not trivial due to the difference in sampling volume and time lag. By comparing various IWC-Ze power-law relationships based on aircraft and radar measurements against an explicit cloud microphysics model simulation (Sassen and Wang 2002), it was found that these power-law relationships do not always fit. One study (Brown *et al.* 1995) also showed that the IWC retrieval using a 94-GHz radar can be accurate within a factor of 2 if Ze alone is used, and it can be improved if the mean ice particle effective size is included in the algorithm. The inclusion of the temperature profile can also improve the accuracy of IWC retrievals (Liu and Illingworth 2000).

Launched on April 28, 2006, CloudSat carries the first W-band (94 GHz) cloud profiling radar (CPR) as its only payload instrument (Stephens *et al.* 2002;

Stephens *et al.* 2008). This unique instrument has an ability to sense condensed cloud particles while coincidently detecting precipitation and providing a vertical cross-section of cloud structures.

Preliminary comparisons of lidar and backscattering properties were first conducted during the early 90s (Intrieri *et al.* 1990; Uttal *et al.* 1990). One of the first studies on the retrieval of cloud properties by the combination of lidar and radar measurements was developed by Intrieri et al. (1993). The method employs the wavelength-dependent difference in backscattering between a carbon dioxide lidar at 10.6 μm, an X-band radar at 3.2 cm, and a Ka-band radar at 8.6 mm to determine the ice particle effective diameter. The theoretical and observed backscattering coefficients are also compared by assuming that all cloud particles are spherical solid ice and limiting the lidar retrievals to an optical depth of 1. Later, radar and lidar data are used to describe cloud structure (Mace *et al.* 1998). Studies (Flamant *et al.* 2000) on cirrus conclude that such radar-lidar combinations have difficulty in retrieving small particles with effective diameters smaller than 20 μm due to the limitation in radar sensitivity. Other approaches that constrain lidar extinction retrievals by using radar information (Donovan and Lammeren 2001; Donovan and Coauthors 2001; Okamoto *et al.* 2003; Tinel *et al.* 2005) were also developed.

It is noteworthy that active remote sensing instruments can only carry a very limited number of channels for observations. The scan position is also limited to a fixed short range, which makes the coverage significantly smaller compared to passive instruments. Therefore, the satellite microwave radiometer is the most suitable instrument for deep convective cloud ice property retrievals.

Different methods and satellite channels need to be carefully chosen to infer ice cloud parameters for different cloud types. Thin cirrus clouds are better observed by satellite IR channels because they have smaller ice particle sizes and optical depths. Microphysical properties of ice clouds from deep convective systems and anvil cirrus, which are composed of larger ice particles, are better estimated from microwave channels which can penetrate within and through clouds and which are sensitive to cloud vertical and horizontal structure information. This study focuses on the retrieval of ice cloud parameters from the DMSP SSMIS instrument. In the next chapter, this instrument and its calibration issues will be first discussed before proceeding to its use in retrieving ice cloud parameters.

Chapter 3: Calibration and Validation of DMSP SSMIS

In October 2003, the first Special Sensor Microwave Imager Special (SSMIS) was launched aboard the Air force Defense Meteorological Satellite Program (DMSP) F-16 Spacecraft to obtain synoptic maps of critical atmospheric, oceanographic, and land parameters to support Numerical Weather Prediction (NWP) as well as other civilian users. As the first of five instruments scheduled for launch over the next decade, the SSMIS integrates the imaging capabilities of the heritage DMSP conically scanning Special Sensor Microwave/Imager (SSM/I) sensor with the cross-track microwave Special Sensor Microwave Temperature (SSM/T) and Special Sensor Microwave Humidity (SSM/T-2) sounders into a single conically scanning 24-channel instrument with extended sounding capability to profile the mesosphere (10-0.03mb). As such, the SSMIS represents the most complex operational satellite passive microwave imager/sounding sensor ever flown, while at the same time offering new capabilities associated with radiometer channels having common fields of view (*FOV*), uniform polarizations, and fixed spatial resolutions across the scan swath (1700 km), and bringing with it new challenges as well.

In this chapter, after briefly introducing SSMIS scan geometry and channel frequencies, calibration issues of F-16 SSMIS will be described to provide a in-depth understanding on the advantages of such new generation microwave instrument. Imaging channel data quality is also evaluated by comparing same products from DMSP F-15 SSM/I (Sun and Weng 2008) to prove that F-16 SSMIS data are suitable for operational applications.

3.1 Introduction to DMSP SSMIS

As shown in Fig. 3.1, the DMSP F-16 spacecraft flies in a circular sun-synchronous near-polar orbit at an altitude of approximately 833 km with an inclination of 98.9 degrees, an orbit period of 101.8 min, and a local time ascending node of 19:54.

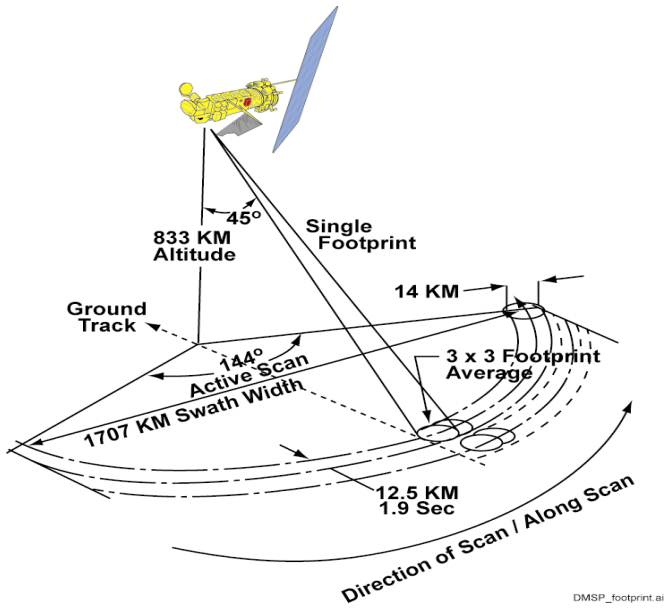

Figure 3.1: DMSP F-16 SSMIS Scan Geometry (from SSMIS Technical Report)

The passbands and polarizations selected from SSMIS are based largely on the heritage sensors SSM/T, SSM/T-2, and SSM/I as shown in Table 3.1.

Table 3.1: DMSP F-16 SSMIS Channel Characteristics (SSMIS Technical Report)

Channel	Center Freq.(GHz)	3-db Width (MHz)	Freq. Stab.(MHz)	Pol.	NEDT (K)	Sampling Interval(km)
1	50.3	380	10	V	0.34	37.5
2	52.8	389	10	V	0.32	37.5
3	53.596	380	10	V	0.33	37.5
4	54.4	383	10	V	0.33	37.5
5	55.5	391	10	V	0.34	37.5
6	57.29	330	10	RCP	0.41	37.5
7	59.4	239	10	RCP	0.40	37.5

8	150	1642(2)	200	H	0.89	12.5
9	183.31±6.6	1526(2)	200	H	0.97	12.5
10	183.31±3	1019(2)	200	H	0.67	12.5
11	183.31±1	513(2)	200	H	0.81	12.5
12	19.35	355	75	H	0.33	25
13	19.35	357	75	V	0.31	25
14	22.235	401	75	V	0.43	25
15	37	1616	75	H	0.25	25
16	37	1545	75	V	0.20	25
17	91.655	1418(2)	100	V	0.33	12.5
18	91.655	1411(2)	100	H	0.32	12.5
19	63.283248±0.285271	1.35(2)	0.08	RCP	2.7	75
20	60.792668±0.357892	1.35(2)	0.08	RCP	2.7	75
21	60.792668±0.357892 ±0.002	1.3(4)	0.08	RCP	1.9	75
22	60.792668±0.357892 ±0.0055	2.6(4)	0.12	RCP	1.3	75
23	60.792668±0.357892 ±0.016	7.35(4)	0.34	RCP	0.8	75
24	60.792668±0.357892 ±0.050	26.5(4)	0.84	RCP	0.9	37.5
Notes	(1) Sampling refers to along-scan direction based on 833km spacecraft altitude. (2) NEDT for instrument temperature 0C and calibration target 260K with integration times of 8.4 msec for Channels 12-16; 12.6 msec for Channels 1-7, 24; and 25.2 msec for Channels 19-23 and 4.2 msec for Channels 8-11, 17-18. (3) Number of sub-bands is indicated by (n) next to individual 3-db width. (4) RCP denotes right-hand circular polarization.					

The center frequencies, bandwidths, and frequency stabilities of the lower air temperature sounding channels (LAS), 1-7, are similar to those employed by SSM/T, whereas the humidity sounding frequencies, passbands, and stabilities, of Channels 8-11, are nearly the same as SSM/T-2. The horizontal polarization (H-POL) was selected for the sounding channels sensing the surface emissions. However, the F-16 SSMIS (S/N 02) is incorrectly designed with vertical polarization (V-POL) in LAS channels 1 to 5. For subsequent SSMIS Flight units, these channel will be configured

as H-POL. Based on the success of the SSM/I instrument, the SSM/I frequencies and polarizations were selected, with the exception of changing 85.5 to 91.655 GHz to reduce hardware complexity, along with the SSM/I conical scan geometry and external calibration approach. The 6 upper air temperature sounding channels (UAS), 19-24, near the 60 GHz oxygen absorption band are actually sensing the right hand circular polarization (RCP) of the upwelling partially polarized energy (Table 3.1).

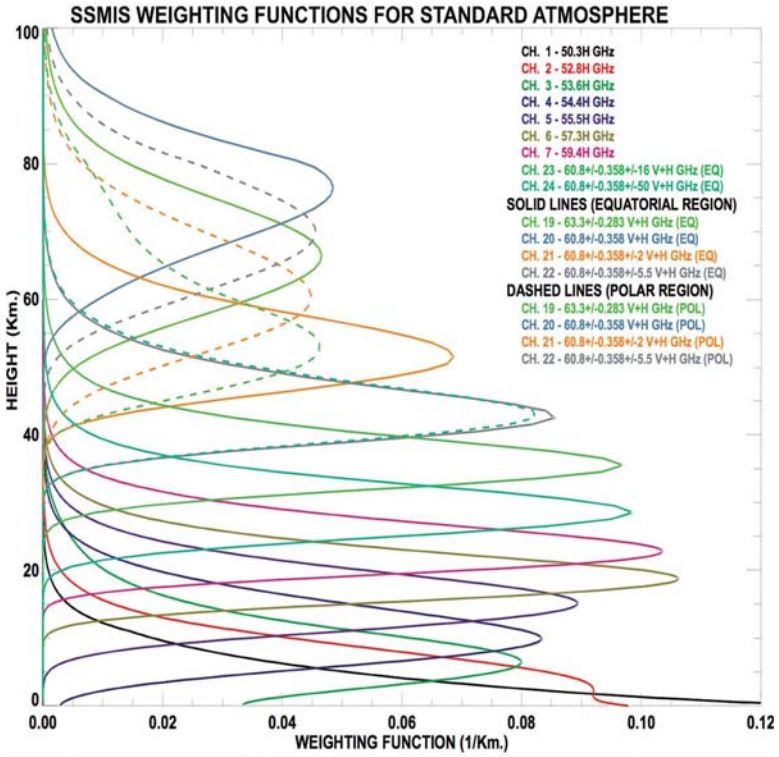

Figure 3.2: DMSP F-16 SSMIS LAS/UAS Weighting Function for Standard Atmosphere (from SSMIS Technical Report)

Presented in Fig. 3.2 are the SSMIS LAS and UAS weighting functions for the standard atmosphere. With its 24 channels, the SSMIS combines the capabilities of the SSM/I and the existing Advanced Microwave Sounding Unit (AMSU-B) on a single platform and alleviates the difficulty of aligning scenes from separate conical and cross-track scanning instruments.

3.2 Reclibration of DMSP SSMIS Temperature Data Records (TDR)

After preliminary analysis of the SSMIS TDR distributed by the Fleet Numerical Meteorology and Oceanography Center (FNMOC), it was found that the original TDRs display notable anomalies compared to radiative transfer model simulations (Kunkee *et al.* 2008; Yan and Weng 2008). In this section, an introduction to SSMIS TDR calibration in different subunits will be given. It was found that the TDR bias existing in one subunit may not be present in others, which further complicates the calibration procedure.

3.2.1 Calibration of Sounding Channels

Shown in Fig. 3.1 is the TDR bias between observations and model simulations. The radiative forward model adopted here is the community radiative transfer model (CRTM) developed at Joint Center for Satellite Data Assimilation (JCSDA). The model assessment is built on a 0.3x0.3 degree global grid, which means that SSMIS orbital data have been interpolated onto the same resolution grid points. The forward model input field is generated from the National Center for Environmental Prediction (NCEP) Global Forecast System (GFS) 1x1 degree 26-layer 6-hour forecast output. Because the GFS data are generated every 6 hours, four global fields need to be interpolated onto the same resolution SSMIS grid points, both spatially and temporally, for instrument evaluation purposes.

For sounding channels, surface effects only play a very limited role in the forward simulation so that the surface emissivity deficiencies in the radiative transfer

model, particularly over land, will be minimized. The input temperature profile covers the height from the atmospheric lower surface boundary up to 10 mb, so that the CRTM essentially captures the top of atmosphere (TOA), while the water vapor profile derived from the relative humidity only extends up to 100 mb. The CRTM surface input includes the surface type, wind speed, wind direction, coastal percentage, skin temperature, and surface pressure. In addition, because the model simulation exports brightness temperature rather than antenna temperature, the SSMIS TDR data actually undergo an antenna pattern correction (APC), which will be introduced in the next section, so that the bias purely contains the error independent of pre-launch identified hardware problems.

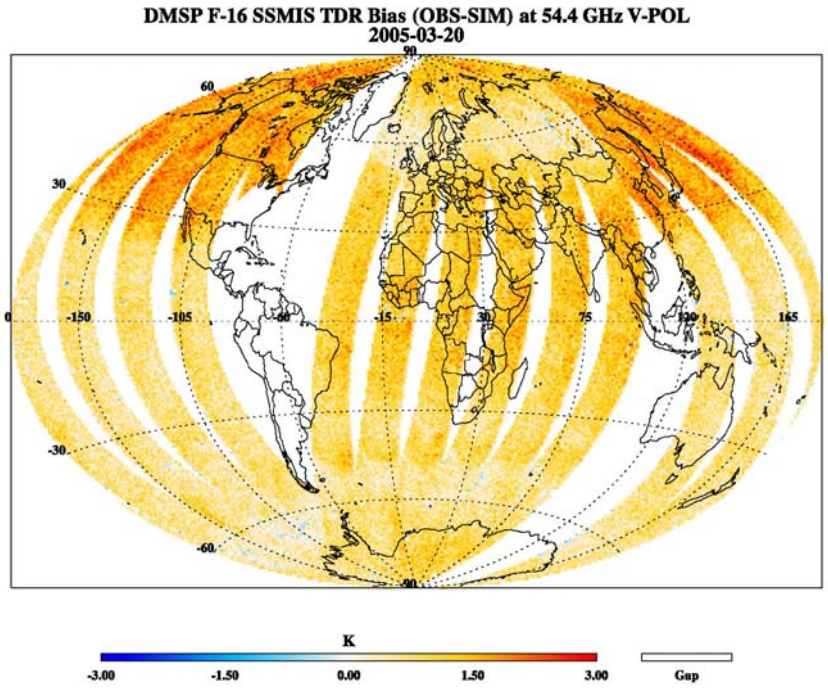

Figure 3.3: DMSP F-16 SSMIS TDR bias at 54.4 GHz V-POL

It is clearly shown in Fig. 3.3 that the brightness temperature bias between observations and simulations can reach as large as 2.5 K in lower atmospheric sounding (LAS) channel 4 (54.4 GHz). The bias in the ascending node case presents a

different pattern compared to that for the descending node. Generally the bias gradient for the ascending node is higher than that for the descending node. The maximum bias always happens when the satellite flies northward after it reaches about 25-30^{O}N. The bias for the descending node becomes larger when passing southward and passing 40 ^{O}N. Further study also indicates that all other LAS channels present a similar anomaly distribution pattern, but the scale of the associated anomalies may depend on the channel frequency, as well as the season. It is also found that the bias "jump" latitude changes with the time, showing an annual oscillation around 30^{O}N. Because the average local equatorial crossing time of ascending scanning is around 19:40, it is believed that such anomalies may be related to the solar heating of reflector when the instrument emerges from earth's or the spacecraft's shadow (Fig. 3.4a) and from the effects of warm load solar intrusions (Fig. 3.4b). The reflector emission occurs for all scenes where the reflector and scene temperature differ, but its impact is larger when the reflector emerges from shadows and the solar elevation angles are impinging from below the canister top, resulting in a dramatic jump in the reflector face temperature of 70 K or more. Therefore, to remove the TDR anomaly, both the warm count anomaly and the reflector emission need to be corrected. However, due to the different effects of both sources, different methods will be used in the SSMIS TDR recalibration procedure.

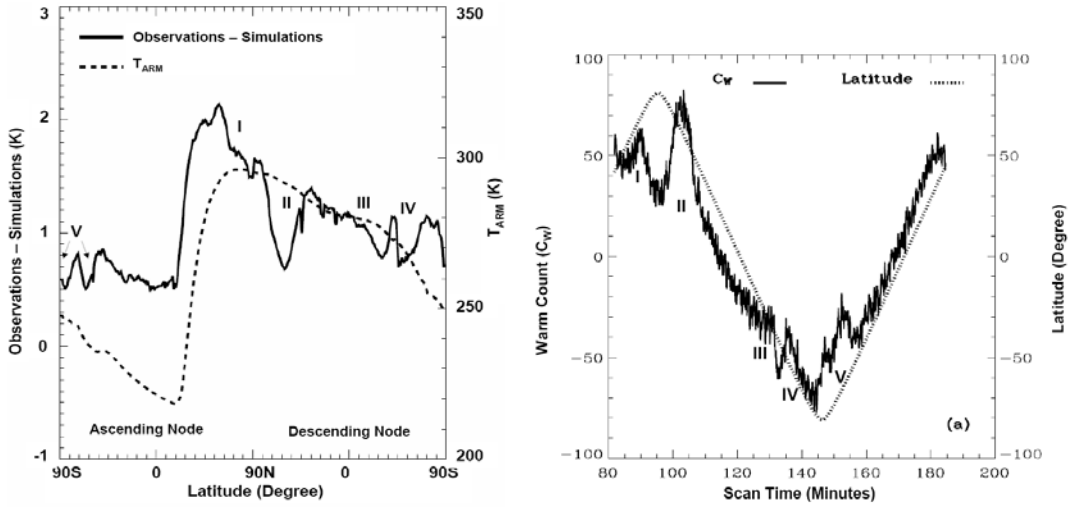

Figure 3.4: DMSP F-16 SSMIS (a) main reflector arm temperature variation (left), and (b) warm calibration count variation (right) at 54.4 GHz V-POL (Yan and Weng 2007)

The warm calibration count anomalies are primarily corrected by applying fast Fourier Transformation (FFT). Due to the distinctive features of warm calibration count variation, designated by the markers I through V in Figure 3.4b, preservation of the major spectrum of FFT decomposition components can effectively remove the anomaly, as shown in Fig. 3.5.

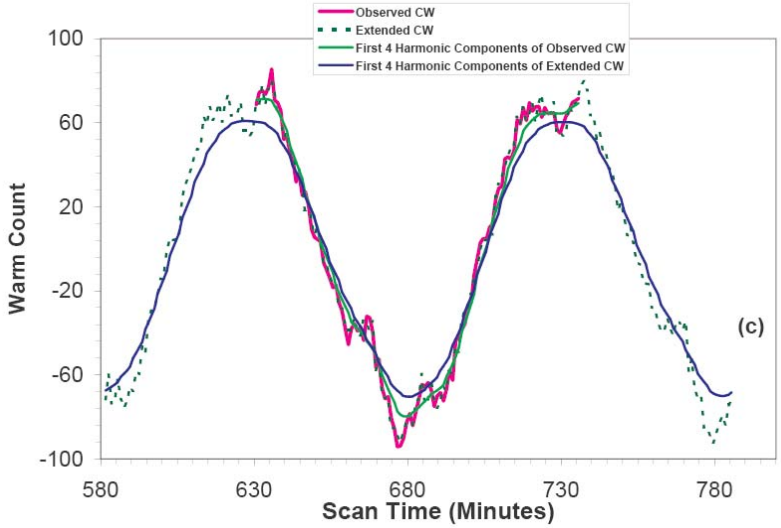

Figure 3.5: Comparison between observed warm calibration count and FFT re-composite (Yan and Weng 2007)

After obtaining the bias of warm calibration count from FFT, the TDR bias then needs be calculated from the calibration equation, as shown in Eq. 3.1.

$$\Delta T_A = -\left[\frac{T_A - T_C}{C_W - C_C}\right]\Delta C_W - \left[\frac{T_W - T_A}{C_W - C_C}\right]\Delta C_C \quad , \quad (3.1)$$

where, T_A, T_C, and T_W are the antenna temperature (TDR), cosmic background temperature, and warm load PRT temperature, respectively. C_W and C_C are warm and cold calibration counts. A cold calibration target bias is also occasionally detected and can be up to as large as 10 counts. Therefore, the cold calibration count bias correction is also included as the second term in the above equation using a similar FFT detection method. Therefore, the error introduced by the warm calibration count solar intrusion can be identified.

The correction of antenna emissions is a little more complicated because the main reflector face temperature cannot be directly observed. In our recalibration method, the antenna emission contamination will be removed by the applying reflector emissivity at different channels to the reflector temperature, which is estimated from the reflector arm temperature T_{ARM} using the following equation:

$$\Delta T_A = \varepsilon_R (T_R - T_A) \quad , \quad (3.2)$$

where, T_A and T_R are the antenna brightness temperature (TDR) and main reflector temperature, and ε_R is the reflector emissivity. Because no main reflector temperature is directly measured, the reflector arm temperature will be used to estimate the reflector face temperature from an empirical function generated by training datasets. However, it is noteworthy that there are time delays between changes in the reflector face temperature and arm temperature. Therefore, there might be a little difference between the real reflector face temperature and derived reflector temperature at any

given time. Considering the small value of the emissivity, such differences can be ignored.

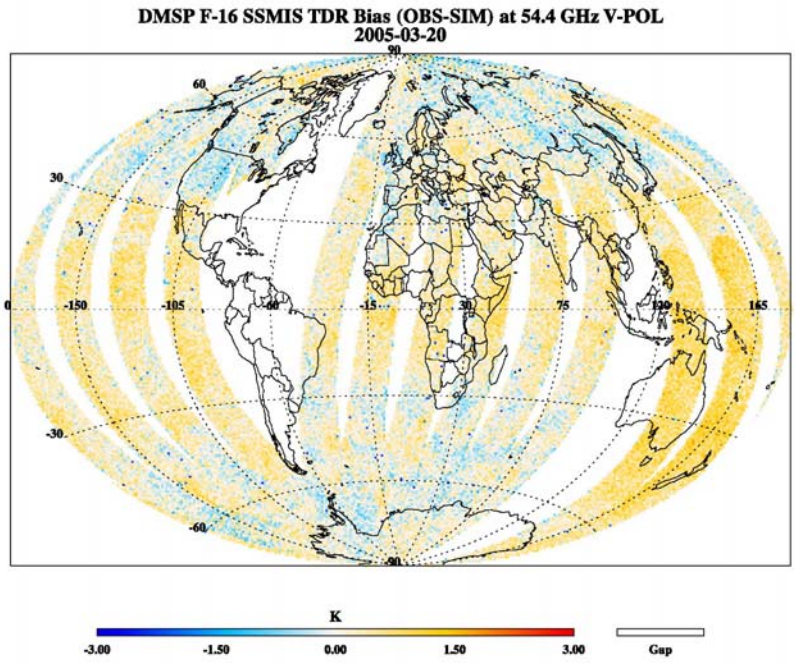

Figure 3.6: Same as in Fig. 3.3, but after recalibration

After both recalibration procedures (correction of warm load solar intrusion and reflector emission), the anomalies presented in the original TDR bias figure (Fig. 3.3) are significantly reduced, as shown in Fig. 3.6.

3.2.2 Calibration of Imaging Channels

For SSM/I-like channels, especially those below 40 GHz, the problems faced are quite different from that of the sounding channels. For 91.655 GHz channels, which have been shifted from 85.5 GHz in SSM/I due to the frequency dependence in the main reflector emissivity, there might be residual biases that affect the TDR in a more significant manner. Such biases could in turn cause residual error in the product retrievals. Because of the uncertainties of surface emissivity in the forward model, it

is difficult to accurately simulate the brightness temperature in these imaging channels. To better identify the bias, the F-16 SSMIS TDR data sets are matched with similar channels from the F-15 spacecraft's SSM/I using the Simultaneous Conical Overpassing (SCO) method (Cao *et al.* 2005). In our SCO match, the spatial window is set to 12.5 km and temporal window is set to 60 seconds. It is also should be mentioned that the SCO match-up data are generally located at the higher latitudes (between 70° and 80°) in both hemispheres due to the matching method. Over these areas, the surface type of coincident TDR pairs could be sea ice, snow, water, or permafrost. Because the spatial window is set to 12.5 km, it is possible that one of the matched data may be from land and the other from ocean. Such situations may affect the SCO technique's accuracy. Therefore, the coincident pairs with extreme high TDR bias will be dropped to ensure the SCO method quality. To minimize the geophysical difference, the matched data are also categorized as either Antarctic and Arctic. The SCO comparison results for year 2005, shown in Table 3.2, indicate that the TDR biases exist in all SSM/I-like channels. The maximum bias can reach up to 3.7 K, occurring in the 22.235 GHz water vapor channel over the Antarctic. It is also found that the SCO biases from the Arctic and Antarctic areas are also different. For example, the mean bias for the 19.35 GHz V-POL case is 0.9 K in the Arctic but is 1.2 K in the Antarctic region. It is also worth mentioning again that for the SSMIS 91.655 GHz channels, the central frequencies were shifted from their original 85.5 GHz for SSM/I so that the SCO TDR biases of these two channels could additionally include the frequency shifting impacts and the contribution of instrumental antenna emission and scattering from the atmosphere.

Table 3.2: DMSP F-16 SSMIS and F-15 SSM/I TDR bias by SCO (Yan and Weng 2008)

Frequency (GHz)	Arctic Samples: 5901		Antarctic Sample: 9540		Cloud Free Samples: >100,000	
	Bias	STDEV	Bias	STDEV	Bias	STDEV
19.35 (V)	0.9	0.8	1.2	0.8	1.4	2.0
19.35 (H)	-0.3	0.6	0.0	0.6	0.2	3.6
22.235 (V)	3.2	1.6	3.7	1.6	3.6	3.5
37 (V)	2.7	1.1	2.8	1.0	3.0	1.9
37 (H)	0.6	1.4	0.4	1.4	1.0	3.9
91.655 (V)	-0.2	1.4	-0.2	1.3	-0.1	2.4
91.655 (H)	-0.1	1.6	-0.1	1.6	0.6	4.0

After systematic analysis, several possible error sources are proposed, which include:

(a) Observation earth incidence angle (EIA);

(b) Instrument antenna pattern difference;

(c) Anomalies associated with calibration parameters;

(d) Nonlinearity impacts in the calibration equation.

The error caused by EIA is caused by the satellite drifting problem. The EIA of both F-16 SSMIS and F-15 SSM/I were set to 53.2° at their launching times. As time passes, the scan angle might incur slight differences after several years of operation. However, model simulations have shown that the brightness temperature variation is only 0.2 K with 1 degree of EIA change. Therefore, biases due to variations of the EIA have very limited impact on the TDR bias overall.

The TDR actually contains earth-located sets of brightness temperature directly converted from the original sensor counts. However, due to the sensor hardware limitations, e.g. feedhorn spillover loss and unavoidable leaks of the vertical polarization signal onto the horizontal polarization receiver, an antenna pattern correction (APC) is needed to correct such errors and obtain usable sensor brightness temperatures (known as Sensor Data Records or SDRs). The Antenna Pattern Function (APF) coefficients for F-15 and F-16 SSM/I-like channels are not the same, which might affect the bias determination between the two instruments.

Table 3.3 presents the contribution of the APC difference to the mean antenna temperature bias at frequencies from 19.35 to 37.0 GHz, which may vary from -1.99 K to 1.6 K near polar areas. The results for the 91.655 GHz channels are not shown here because the bias of the SSMIS 91.655 GHz channels also contains the frequency shift effects. Thus, the antenna pattern difference has significant impacts on the antenna temperature bias.

Table 3.3: TDR bias between F16 and F15 due to APC difference (Yan and Weng 2008)

Frequency (GHz)	ΔT_A **(K)**
19.35 (V)	-0.72
19.35 (H)	0.17
22.235 (V)	-1.99
37.0 (V)	-0.18
37.0 (H)	1.60

Similar to the earlier description, an effect like the main reflector emission bias in the LAS TDR data may also exist for these SSM/I-like high frequency

channels. In order to identify the impacts of reflector emission, the SCO matching restrictions were broadened to collect more coincident pairs. Time differences of less than 10 minutes are used. In addition, only cloud free pairs over the ocean between 60^{O}N and 60^{O}S are used for analysis. The collected matchup data are averaged longitudinally. However, by comparing the longitudinally averaged biases, no significant latitude dependent bias patterns can be found, which indicates that the reflector emission contaminating the LAS antenna temperature has little impact on SSM/I-like channels.

The antenna temperature can theoretically be obtained using the following calibration equation (Mo 2007)

$$T_A = T_C + \frac{T_W - T_C}{C_W - C_C}(C_S - C_C) + \mu\left(\frac{T_W - T_C}{C_W - C_C}\right)^2 (C_S - C_C)(C_S - C_W) \quad , \quad (3.3)$$

where, T_A, T_C, and T_W are antenna temperature, cosmic background temperature, and warm load PRT temperature, respectively. C_W, C_C, and C_S are warm calibration, cold calibration, and scene counts. The third term in Eq. 3.3 is the nonlinear calibration term. μ is the nonlinear parameter, which is proportional to the radiometric counts from the earth view scene.

To calculate the nonlinear parameter, the SCO coincident pairs from F-15 and F-16 collected close to the Arctic and Antarctic regions are separated. Assuming each SCO pair observes exactly the same location at the same time, the antenna temperature difference, after removing the APC bias, is supposed to be exclusively due to the nonlinear term in the calibration equation. Therefore, the nonlinear parameters can be obtained from the calibration equations of the two satellites over the Antarctic and Arctic regions. Table 3.4 gives the nonlinear parameters for five

channels from both F-15 SSM/I and F-16 SSMIS. Because the two 91.655 GHz channels on SSMIS contain frequency shifting effects in the SCO matching, the nonlinear parameters calculated using above method are not as reliable as for the other channels, and no nonlinear parameters are available for these two channels.

Table 3.4: Nonlinear parameters in calibration equation for F-15 SSM/I and F-16 SSMIS at channels from 19.35 to 37.0 GHz (Yan and Weng 2008)

Frequency(GHz)	Nonlinear Parameter (μ)	
	F-15	F-16
19.35 (V)	-7.0449E-6	1.0913E-5
19.35 (H)	-1.1059E-6	-1.0825E-6
22.235 (V)	-5.4371E-5	6.7848E-5
37.0 (V)	-5.6897E-5	7.1057E-5
37.0 (H)	-1.7801E-5	2.2946E-5

The results show that all nonlinear parameters are on the scale of 10^{-5}, which will be equivalent to about 1 K in the 22.235 and 37.5 GHz channel nonlinear terms, but only 0.3 K for the 19.35 GHz channels. Furthermore, if we combine both linear and nonlinear calibration terms in the calibration equation (Eq. 3.3) for the TDR, the SSM/I-like channels antenna temperature biases are significantly reduced and the mean bias is lower than 0.3 K (Yan and Weng 2008).

3.3 Footprint Matching of SSMIS TDRs

As shown in Table 3.1, the SSMIS TDR data are actually collected at different resolutions. In each scan, there are 180 scenes for the environmental (ENV) channels, but 90 scenes for imaging (IMG) channels, only 60 scenes for LAS channels, and just

30 scenes for UAS channels. Even for the IMG channels, the geophysical locations of channel 12-14 (19.35 GHz V/H-POL and 22.235 GHz V-POL) are different from those of channel 15-16 (37.0 GHz V/H-POL). Fig. 3.7 plots all the varisou latitudes and longitudes of a single scan footprint.

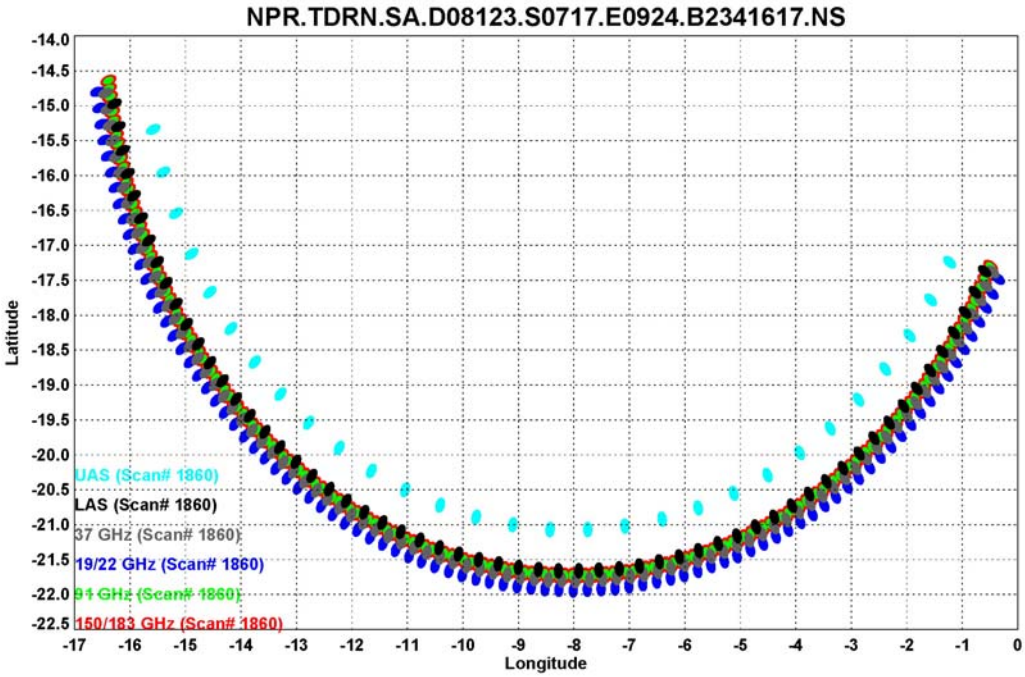

Figure 3.7: DMSP F-16 SSMIS TDR single scan geophysical locations of different channels

In this study, both the ENV and IMG channels' (Channel 8-18) brightness temperature information will be used to derive *IWP*. It is necessary to match different resolution channels to a uniform resolution for better retrieval quality. After comparing the latitude and longitude of different resolution channels, it is found that the best results are to match all other target channels to the 37.0 GHz channel footprint.

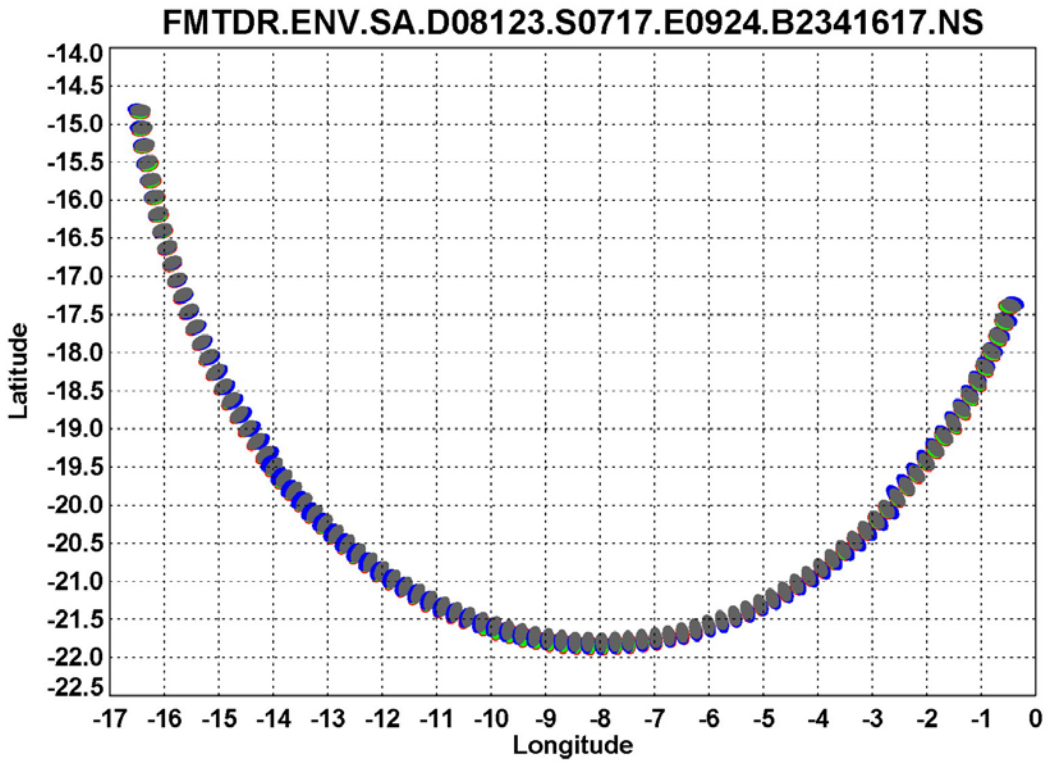

Figure 3.8: Same as in Figure 3.7, but after footprint matching based on 37.0 GHz resolution (Sun and Weng 2009)

Fig. 3.8 is the footprint matching result using Channels 15/16 (37.0 GHz) as the base footprint. For each scan, the scan before and after are grouped and the FOV with the closest geophysical location will be taken. After footprint matching, most scattered scan FOVs are centered within a very nearby geophysical area, if not the exact same location. It is also noteworthy that the identical FOV size given in the plot is for visualization purposes. In fact, the FOVs of lower frequency channels are much larger than higher frequency ones. The designated footprint size is indicated in Table 3.1.

3.4 Evaluation of SSMIS ENV/IMG Channels by Heritage Retrieval Algorithms

3.4.1 SSMIS TDR Antenna Pattern Correction (APC)

TDR data actually contain earth-located sets of brightness temperature directly converted from the original sensor counts. However, due to the sensor hardware limitations, e.g. feedhorn spillover loss and unavoidable leak of vertical polarization signal onto the horizontal polarization receiver, an antenna pattern correction (APC) is used to help identify and reduce such errors and obtain usable sensor brightness temperatures (also known as Sensor Data Records or SDRs). In our study, the APC algorithm consists of a linear correction for the feedhorn spillover loss and cross-polarization coupling, as shown in Eq. (3.4).

$$TB_{v(h)} = \frac{[TA_{v(h)} - a_{v(h)} TA_{h(v)}]}{\eta_{v(h)}(1 - a_{v(h)})} \quad , \qquad (3.4)$$

where

$TB_{v(h)}$ = SDR at vertical (horizontal) polarization,

$TA_{v(h)}$ = TDR at vertical (horizontal) polarization,

$\eta_{v(h)}$ = Feedhorn spillover factor, and

$a_{v(h)}$ = Cross-polarized coupling coefficient.

Because the maximum cross-polarization occurs when the SSMIS views a cloudless dry atmosphere over a calm ocean surface, $a_{v(h)}$ approaches zero in the LAS and UAS

channels. Only the spillover correction term is kept in the APC linear equation for those channels. The DMSP F-16 SSMIS has a larger than expected correction for antenna cross polarization effects even though the APC for SSMIS was originally intended to correct primarily for antenna spillover. In our study, the DMSP F-16 SSMIS SSM/I-like lower frequency channels' linear mapping coefficients and APC are take from Yan and Weng 2008. Because some SSM/I heritage algorithms were developed using 85.5 GHz observations, linear mapping coefficients for converting 91.655 GHz to 85.5 GHz were kindly provided by Naval Research Laboratory (NRL) to make the heritage retrieval algorithms directly applicable to SSMIS data when 85.5 GHz observations are involved.

Due to the different sampling resolution of SSM/I-like channels, we first produce global gridded data at a resolution of 0.3x0.3 degrees and then separate the data into two files corresponding to ascending and descending nodes. Next, a set of empirical linear remapping coefficients are applied to F-16 SSM/I-like channels. Eq. (3.5) is used to make these channel signatures closer to the corresponding heritage SSM/I channels.

$$TA'_{ichan} = \alpha_{ichan} + \beta_{ichan} TA_{ichan} \quad , \qquad (3.5)$$

where

TA'_{ichan} = remapped antenna brightness temperature,

TA_{ichan} = original antenna brightness temperature, and

$\alpha_{ichan}, \beta_{ichan}$ = remapping coefficients.

Note that such a remapping also includes the mapping of F-16 SSMIS 91.655 GHz to SSM/I 85.5 GHz so as to minimize the effects of the channel frequency shift, thereby allowing existing F-15 SSM/I retrieval algorithms to be used with F-16 data. Finally, the TDR to SDR conversion will be implemented by applying the linear APC algorithm to the remapped TDRs, as shown in Eq. (3.4).

3.4.2 Applications of Heritage Retrieval Algorithms

The retrieval algorithms used to generate environmental products were previously developed by the SSM/I Cal/Val science teams and have been widely used at NOAA since the 1990s, as described in Ferraro *et al.* (1996). The products used in this evaluation include total precipitable water (TPW), cloud liquid water path (LWP), snow and sea ice coverage, land surface temperature (LST), rainfall rate (RR), and land emissivity, as presented in Table 3.5. In addition to comparing the global pattern profiles of the retrieval data, we also analyze the differences by plotting scatter diagrams for TPW, LWP, LST, and land emissivity retrievals in order to provide a more straightforward sense of whether heritage retrieval algorithms are fit for the application to F-16 SSM/I-like channels, and whether the F-16 SSMIS TDR recalibration algorithm performs well.

To demonstrate the product retrieval quality and stability, data between December 2005 and February 2006 (DJF) are processed. By evaluating these products from hydrometeor (TPW, LWP, and RR) and land surface products (LST, emissivity), as well as snow and ice cover, we may not only better understand the quality of DMSP F-16 SSMIS retrievals. In this section, each product will be illustrated, and statistical analyses of several products will also be given.

Table 3.5: Summary of Validation Heritage Retrieval Algorithms

Parameter	Channels (GHz)	Units	Area	Reference
Total Precipitable Water (TPW)	19.35V, 22.235V, 37.0V	mm	Ocean	Alishouse *et al.* 1990
Cloud Liquid Water (LWP)	19.35V, 22.235V, 37.0V, 85.5H	mm	Land	Weng and Grody 1994; Weng *et al.* 1997
Snow Cover	19.35V/H, 22.235V, 37.0V, 85.5V		Land	Grody 1991; Grody and Basist 1996
Sea Ice Cover	19.35V/H, 22.235V, 37.0V/H, 85.5V		Ocean	unpublished
Land Surface Temperature (LST)	22.235V, 37.0V, 85.5V	K	Land	Weng and Grody 1998
Rain Rate (RR)	19.35V, 22.235V, 37.0V, 85.5V	mm/hr	All	Grody 1991; Ferraro and Marks 1995
Land Emissivity	19.35V/H, 22.235V, 37.0V/H, 85.5V/H		Land	Weng *et al.* 2001; Yan and Weng 2003

A. Total Precipitable Water (TPW)

The water vapor path retrieval, also known as total precipitable water (TPW), has been constructed globally over the ocean from passive microwave instruments since 1987 when the first SSM/I was launched aboard the DMSP F-8 vehicle. The algorithm has been updated from Alishouse *et al.* (1990) by using brightness temperatures at 19.35V, 22.235V, 37.0V, and 85.5V (all frequencies in GHz). As one of the most accurate parameters retrieved by passive microwave sensors, the error is only around 10% on a globally averaged basis compared with radiosonde observations (Alishouse *et al.* 1990). In our study, a slight modification is applied to the original algorithm in order to obtain more accurate results under extreme weather conditions.

$$TPW = 232.89 - 0.1486(TB_{19v}) - 0.3695(TB_{37v}) - [1.8291 - 0.006193(TB_{22v})]TB_{22v}, \quad (3.6a)$$

$$TPW_{corrected} = -3.753 + 1.507(TPW) - 0.1933(TPW)^2 + 0.00219(TPW)^3, \quad (3.6b)$$

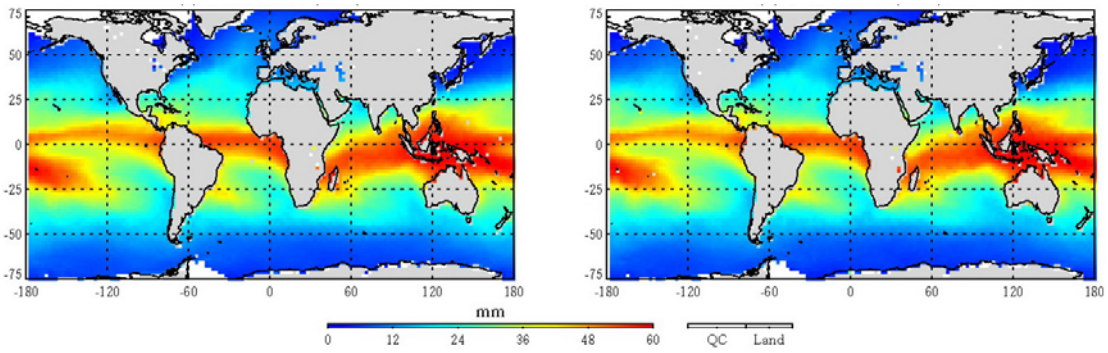

Figure 3.9: Totoal precipitatble water (TPW) retrieved from F-16 SSMIS (left) and F-15 SSM/I (right)

In the retrieval process, TPW is first calculated using the first equation in Eq. (3.6a). Simultaneously, a scattering index (SI) is also computed (the details of this index will be introduced in the discussion of rain rate retrieval). Whenever the scattering index is greater than 10 K, meaning the possible existence of precipitation, an additional cubic correction is applied via the second equation in Eq. 3.6b to get a corrected TPW.

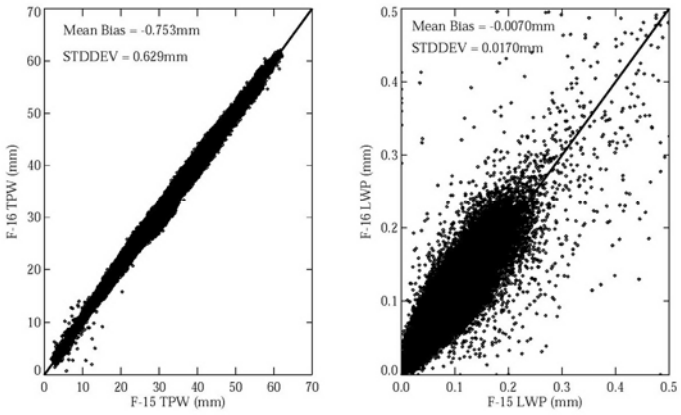

Figure 3.10: Scatter plot of (a) TPW (left) and (b) LWP (right) from DMSP F-15 SSM/I and DMSP F-16 SSMIS Imaging Channels

Plotted in Fig. 3.9 are the TPW data retrieved from F-16 (left) and F-15 (right), respectively. Please note that no TPW is retrieved over sea ice due to its high and variable emissivity. From both figures, we can observe many similar features and phenomena associated with the Inter-tropical Convergence Zone (ITCZ), South Pacific Convergence Zone (SPCZ), and South Atlantic Convergence Zone (SACZ). Fig. 3.10(a) gives a statistical comparison between TPW retrievals from F-16 and F-15. The mean bias, standard deviation (STDEV), and root mean square (RMS) of corresponding parameters are given in Table 3.6. The statistical results indicate that the preprocessing of F-16 SSMIS data produces good quality TPW data from the imager channels at 19.35, 22.235, and 37.0 GHz.

Table 3.6: Statistical Analysis of Retrieval Bias for Selected Parameters

Parameter	Mean Bias	STDEV	RMS
TPW	-0.753 mm	0.629 mm	0.981 mm
LWP	-0.007 mm	0.017 mm	0.018 mm
LST	1.531 K	1.373 K	2.056 K
RR	-0.013 mm/hr	0.110 mm/hr	0.111 mm/hr
$\varepsilon_{19.35V}$	0.0017	0.0034	0.0038
$\varepsilon_{19.35H}$	0.0019	0.0045	0.0049
$\varepsilon_{22.235V}$	0.0017	0.0034	0.0038
$\varepsilon_{37.0V}$	0.0007	0.0050	0.0051
$\varepsilon_{37.0H}$	0.0017	0.0063	0.0065

B. Cloud Liquid Water Path

The retrieval algorithm for cloud liquid water path (LWP) adopted in our study was introduced in a pair of papers (Weng and Grody 1994; Weng *et al.* 1997).

This algorithm makes use of brightness temperature measurements at both low and high frequencies to retrieve LWP in precipitating and non-precipitating clouds over ocean. Three LWPs are pre-calculated using different channel combinations (19.35 V/22.235 V, 37.0V/22.235 V, and 85.5 H/22.235 V). The final LWP is determined by several criteria, as shown in Eq. 3.7:

$$LWP = \begin{cases} -3.20[\ln(290 - TB_{19v}) - 2.8 - 0.42\ln(290 - TB_{22v})], & LWP > 0.7 \\ -0.44[\ln(290 - TB_{85h}) - 1.6 + 1.35\ln(290 - TB_{22v})], & LWP > 0.28 \text{ and } TPW < 30 \\ -1.66[\ln(290 - TB_{37v}) + 2.9 + 0.35\ln(290 - TB_{22v})], & else \end{cases} \quad . \quad (3.7)$$

This algorithm improves over former LWP retrievals by detecting LWP both in optically thin stratus and low-level clouds, as well as in highly convective clouds. The global LWP retrievals in boreal winter using F-15 and F-16 data are given in Fig. 3.11.

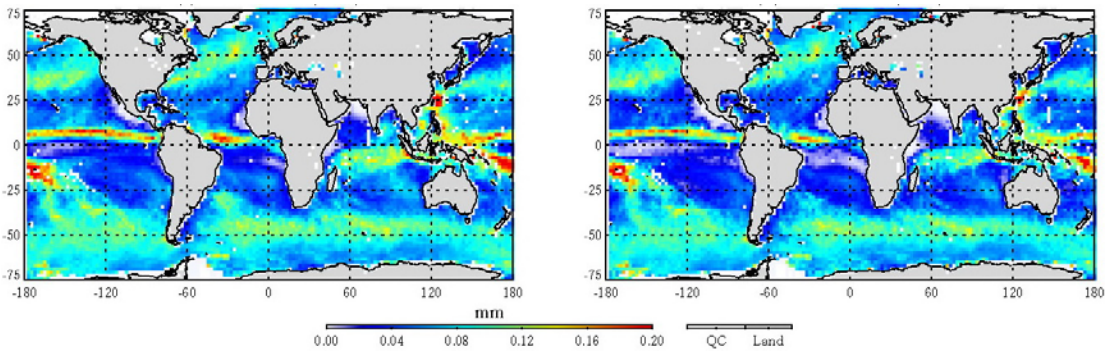

Figure 3.11: Same as Fig. 3.9 but for cloud liquid water path (LWP) retrieval

Cloud liquid water path retrieved from the two sensors shows similarities in their spatial distribution. Some expected features have been captured in the global patterns, such as the presence of strong convection over the western Pacific warm pool, SPCZ, and SACZ. However, along the continental coasts and sea ice edges there are some anomalously large LWP values. This may be caused by a mismatch of TDRs or contamination by surface sea ice. Meanwhile, near the high LWP areas,

some anomalously low points may be due to the saturation of SSMIS imaging channels from heavy precipitation. The correlation between F-15 and F-16 is presented in Fig. 3.10(b) and is nearly linear. The increased scatter at higher LWP is probably due to the mismatch of the scale of the observations and the spatial inhomogeneity of clouds and precipitation. However, the small mean bias and standard deviation indicate that the LWP retrievals from SSMIS are reliable and can be used operationally.

C. Land Surface Temperature

The land surface temperature (LST) algorithm for SSM/I was originally presented in Weng and Grody (1998). As a linear regression algorithm developed from ground truth data, LST can be directly obtained over crop/range, moist and dry soils, and other surface types without identify surface type in advance. SDR measurements at 22.235 GHz V, 37.0 GHz V, and 85.5 GHz V are used in this algorithm as shown by Eq. (3.8):

$$\begin{aligned} LST = \; & 0.02509[1.7167 - 0.005514(TB_{22v})]TB_{22v} \\ & -[0.1083 + 0.001976(TB_{37v})]TB_{37v} \\ & +[1.1763 - 0.000636(TB_{85v})]TB_{85v} \end{aligned} \quad . \qquad (3.8)$$

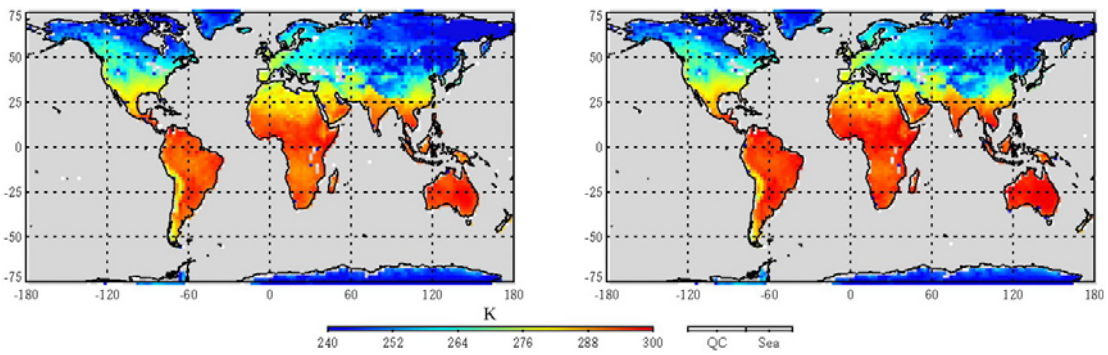

Figure 3.12: Same as Fig. 3.9 but for land surface temperature (LST) retrieval

The global retrieval results can be found in Fig. 3.12(e) and (f). The LST patterns of F-15 and F-16 are highly consistent with each other. Compared to the summer season retrievals (not shown here) which shows the expected changes, most of Eurasia presents a lower LST due to the snow cover. However, it is shown (see Fig. 3.13(a)) that the mean LST of F-15 is about 1.5 K higher than that of F-16. The bias and standard deviation also increase with increasing LST. The outliers with large bias in Fig.3.13(a) are probably caused by measurement mismatches along coastal regions and by the deficiencies in the remapping algorithm which excludes scattering and emission adjustment. Overall, the SSM/I LST retrieval algorithm may be migrated to SSMIS for operational use, but there is still a need to refine the remapping coefficients that convert SSMIS brightness temperatures at 91.655 GHz to SSM/I brightness temperature at 85.5 GHz, since Eq. 3.8 is used for both SSM/I and SSMIS.

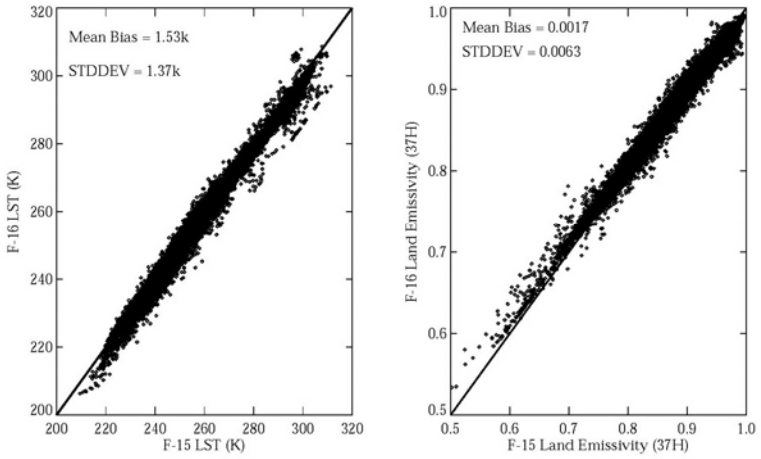

Figure 3.13: Scatter plot of (a) LST (left) and (b) emissivity at 37.0 GHz (right) from DMSP F-15 SSM/I and DMSP F-16 SSMIS Imaging Channels

D. Rain Rate

The rainfall rate (RR) algorithm developed at NESDIS (Ferraro and Marks 1995) makes use of the scattering of upwelling radiation by precipitating cloud ice particles and large raindrops at 85.5 GHz to detect rainfall both over land and oceans. The difference between actual and an estimated (through 19.35 GHz V-POL and 22.235 GHz V-POL observations) brightness temperatures at 85.5 GHz V-POL, which is referred to as the "scattering index" in Grody 1991, is calculated by Eq.(3.9).

$$SI = EST_{TB_{85v}} - TB_{85v} \quad , \qquad (3.9)$$

where,

$$EST_{TB_{85v}} = \begin{cases} 438.5 - 0.46(TB_{19v}) - 1.735(TB_{22v}) + 0.00589(TB_{22v})^2, & land \\ -182.7 - 0.75(TB_{19v}) + 2.543(TB_{22v}) - 0.00543(TB_{22v})^2, & ocean \end{cases}.$$

An indication of rain is obtained if *SI* is greater than 10K. In addition, the LWP retrieval is also used over the oceans to identify the rainfall area. As a result, the minimum detectable rain rate is about 0.5 mm/h over land and 0.2 mm/hr over ocean.

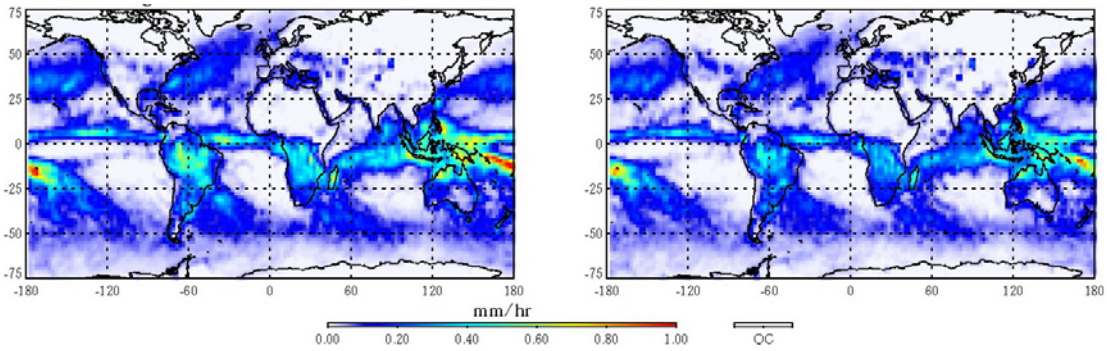

Figure 3.14: Same as Fig. 3.9 but for rain rate (RR) retrieval

Fig. 3.14 display the rain rate retrieval from F-16 (left) and F-15 (right). Over ocean, RR retrievals from each sensor correlate highly to its own high LWP retrieval regions and also between each other. One can also easily discern from the figures the heavy rainfall over certain key areas, such as the western Pacific warm pool and

SPCZ. The smooth continuous RR transition between land and ocean in both figures confirms that the RR retrieval algorithm can correctly capture the rainfall signals both over land and ocean. However, even though the geophysical locations for RR are close to each other over land, the scales are not consistent between F-15 and F-16. As RR is a parameter highly dependent on the scan time, the bias could be very large even when the scan time difference between F-15 and F-16 is around 30 minutes. Therefore, it is yet to be determined whether the source of bias is due to scan time differences or sensor differences. Furthermore, because the RR retrieval also uses the 85.5 GHz channel measurements remapped from 91.655 GHz in F-16 SSMIS via globally derived linear coefficients, the more localized RR retrieval presents a larger bias between F-16 SSMIS and F-15 SSM/I.

E. Sea Ice

Several sea ice concentration and ice age algorithms have been developed for passive microwave radiometers (Rubinstein *et al.* 1994; Markus and Cavalieri 2000). Comparisons between these algorithms have also been performed (Markus and Dokken 2002; Shokr and Markus 2006). To maintain the continuity of our heritage study of sea ice cover, a simple algorithm is used to identify the presence of sea ice. The retrieval function firstly calculates the ice concentration by

$$\begin{aligned} ICE = \; & 91.9 - 2.99(TB_{22v}) + 2.85(TB_{19v}) \\ & - 0.39(TB_{37v}) + 0.50(TB_{85v}) \\ & + 1.01(TB_{19h}) - 0.90(TB_{37h}) \end{aligned} \quad . \qquad (3.10)$$

When ICE is greater than 70%, this point is defined to be covered by sea ice. In our sea ice averaging, the percentage of sea ice present during the three winter months

(December, January, February) is calculated. Fig. 3.15 (a)-(d) presents the sea ice cover retrieved from F-16 and F-15 over the northern and southern polar areas, respectively.

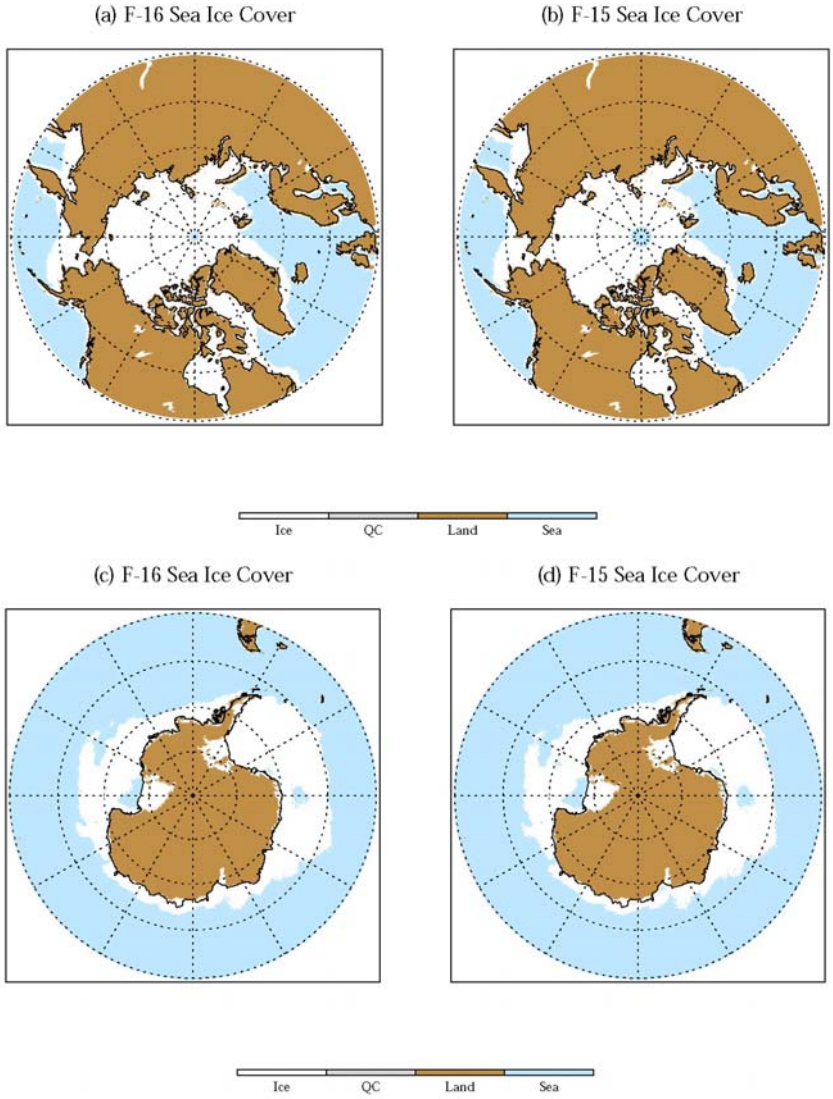

Figure 3.15: Sea ice cover retrieved in North Polar region from (a) F-16 SSMIS and (b) F-15 SSM/I; and in South Polar region from (c) F-16 SSMIS and (d) F-15 SSM/I

The sea ice cover in the northern hemisphere extends south of 50^{o}N both along east coast of North America and the Eurasian continent. Due to the North-

Atlantic current, there is a lack of sea ice in the Barents Sea. Overall, the sea ice cover from F-15 SSM/I and F-16 SSMIS are in good agreement.

F. Snow Cover

The snow coverage retrieval algorithm used in our study was published in a pair of papers by Grody (Grody 1991; Grody and Basist 1996). The method includes measurements at 85.5 GHz to detect shallow snow cover and also screens for precipitation, cold desert, frozen ground, and other signatures which could potentially increase retrieval error. In this algorithm, brightness temperature measurements at 19.35 GHz V-POL, 22.235 GHz V-POL, 37.0 GHz V-POL and 85.5 GHz V-POL are used.

Snow cover retrieved from F-15 and F-16 near the north and south poles are shown in Fig. 3.16 (a), (b), (c), and (d). Because the retrievals are from December 2005 to February 2006, most of areas north of 40^{o}N are covered by snow. Overall, the snow cover retrievals from the two sensors are highly consistent. However, because snow retrieval also uses 85.5 GHz measurements to derive the scattering parameter, the globally derived remapping coefficient may also affect snow cover retrieval. Therefore, stratified remapping coefficients will be developed.

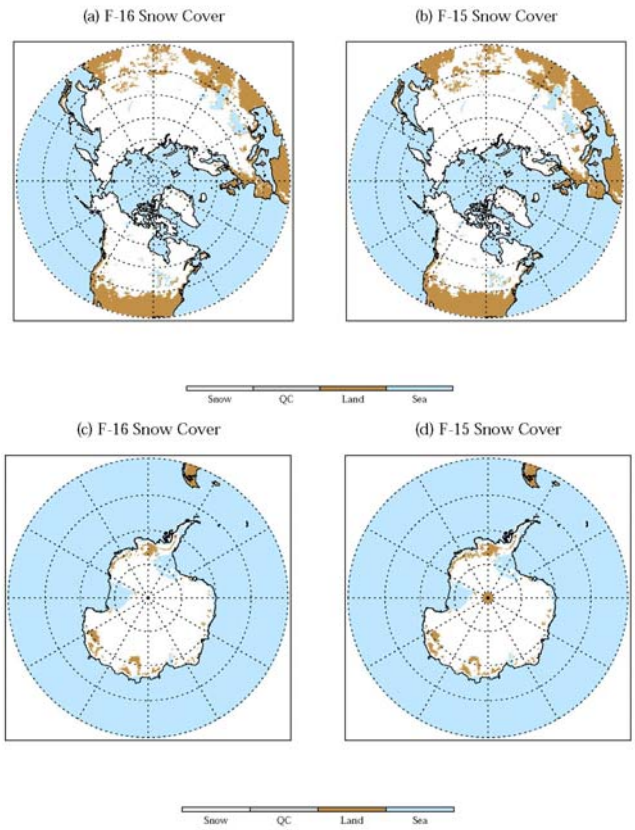

Figure 3.16: Snow cover retrieved in North Polar region from (a) F-16 SSMIS and (b) F-15 SSM/I; and in South Polar region from (c) F-16 SSMIS and (d) F-15 SSM/I

G. Land Emissivity

The land emissivity is an important parameter that can be used to infer some other geophysical parameters, such as soil moisture, vegetation water, and soil wetness. The land emissivity algorithm was published in a pair of papers by Weng (Weng *et al.* 2001; Yan and Weng 2003). For low frequency channels at 19.35 GHz V/H and 37.0 GHz V/H, the emissivities are based on a linear regression relationship among all seven SSM/I-like channel SDR measurements, as shown in Eq. 3.11:

$$\begin{aligned}\varepsilon = \quad & a_0 + a_1(TB_{19v}) + a_2(TB_{19h}) + a_3(TB_{22v}) \\ & a_4(TB_{37v}) + a_5(TB_{37h}) + a_6(TB_{85v}) + a_7(TB_{85h})\end{aligned} \quad . \qquad (3.11)$$

For emissivity at 85.5 GHz V-POL and 85.5 GHz H-POL a nonlinear relationship is built from the 37.0 GHz V and 85.5 GHz V/H data using Eq. 3.12 due to the high scattering effects in both channels:

$$\varepsilon = \begin{array}{l} b_0 + [b_1 + b_2(TB_{37v})](TB_{37v}) \\ [b_3 + b_4(TB_{85v})](TB_{85v}) + [b_5 + b_6(TB_{85h})](TB_{85h}) \end{array} \quad . \quad (3.12)$$

Table 3.7 presents the coefficients in Eq. 3.11 and Eq. 3.12 for each channel. Here, we choose retrievals at 19.35 GHz (H/V) and 37.0 GHz (H/V) for demonstration purposes.

Table 3.7: Land Emissivity Retrieval Coefficients

Channel	$\mathbf{a_0}$	$\mathbf{a_1}$	$\mathbf{a_2}$	$\mathbf{a_3}$	$\mathbf{a_4}$	$\mathbf{a_5}$	$\mathbf{a_6}$	$\mathbf{a_7}$
19.35 V	0.5098	4.4664E-3	-6.0427E-6	-2.5285E-3	-2.3725E-3	9.8163E-4	-2.2269E-3	-1.3193E-3
19.35 H	0.4290	1.0685E-3	4.0082E-3	-2.9672E-3	1.4281E-3	1.7393E-3	-1.0247E-3	-2.2088E-3
22.235 V	0.5098	4.4664E-3	-6.0427E-6	-2.5285E-3	-2.3725E-3	9.8163E-4	-2.2269E-3	-1.3193E-3
37.0 V	0.3186	-1.5225E-3	1.7213E-3	-3.7164E-4	6.5607E-3	8.1213E-4	-1.7678E-3	-1.7250E-3
37.0 H	0.2622	-1.5095E-3	-1.9587E-5	5.0142E-4	6.8795E-4	5.7910E-3	-7.1539E-4	-2.1267E-3
Channel	$\mathbf{b_0}$	$\mathbf{b_1}$	$\mathbf{b_2}$	$\mathbf{b_3}$	$\mathbf{b_4}$	$\mathbf{b_5}$	$\mathbf{b_6}$	
85.5 V	-0.9435	4.1137E-3	-7.0109E-6	1.5677E-2	-3.1055E-5	-6.5089E-3	1.4984E-5	
85.5 H	-0.9788	3.0851E-3	-5.2696E-6	7.4612E-3	-2.2772E-5	2.9755E-3	4.5324E-6	

The results are shown in Fig. 3.17. Because the channel frequency shifts from 85.5 GHz in F-15 SSM/I to 91.655 GHz in F-16 SSMIS, we do not include these two channel emissivities in this comparison.

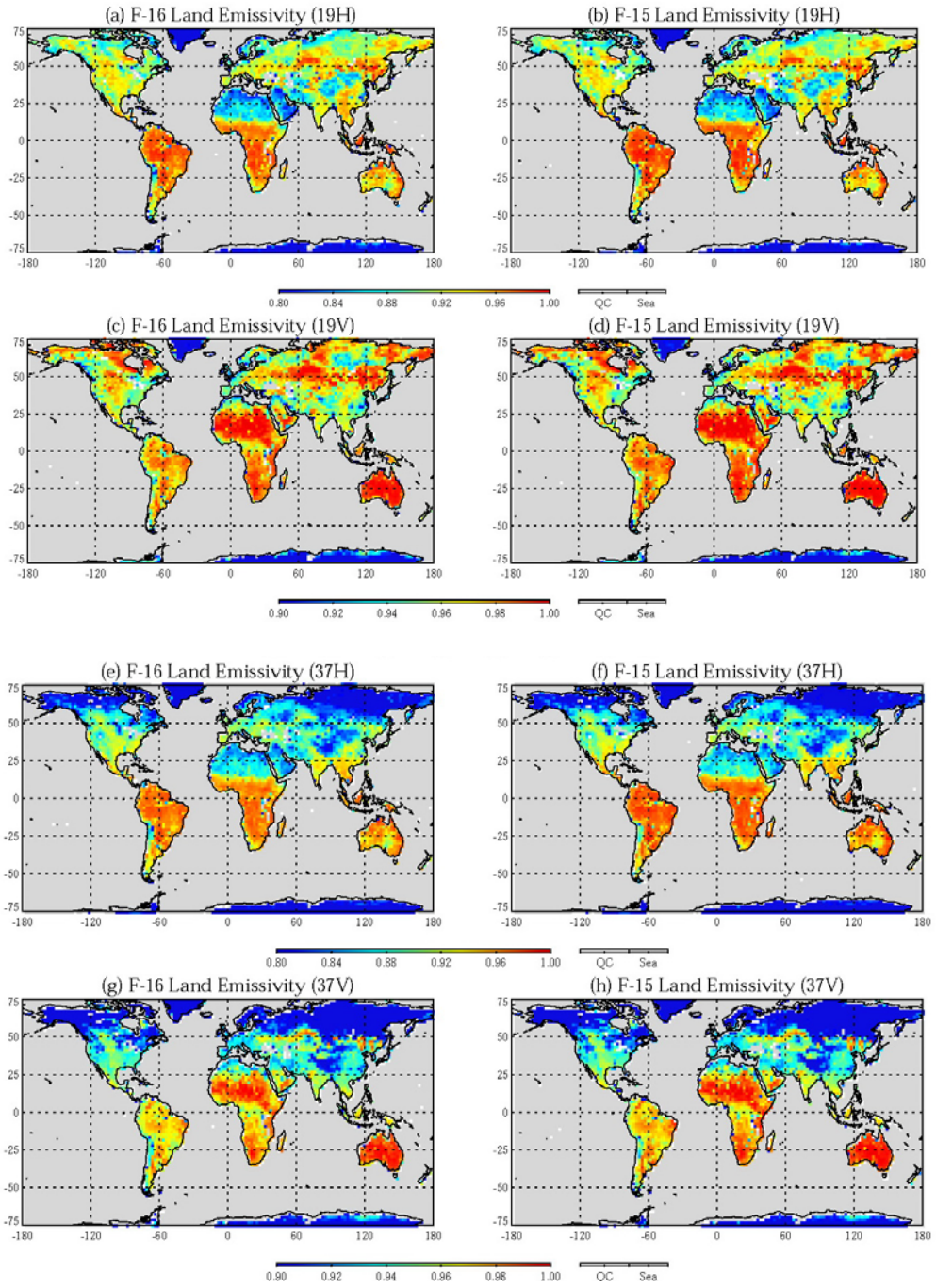

Figure 3.17: Land emissivity retrieved in the 19H channel by (a) F-16 SSMIS and (b) F-15 SSM/I; for 19V by (c) F-16 SSMIS and (d) F-15 SSM/I; for 37H by (e) F-16 SSMIS and (f) F-15 SSM/I; for 37V by (g) F-16 SSMIS and (h) F-15 SSM/I

The retrievals from each sensor capture land surface signatures well. For example, vertical polarization over deserts shows a larger emissivity compared to

horizontal polarization. In addition, emissivity retrieved from 37.0 GHz is more sensitive to snow surface conditions than the 19.35 GHz channels. Generally speaking, the retrievals are very well correlated. However, very similar to the land surface temperature retrieval, the difference between emissivities retrieved for F-16 and F-15 for 37.0 GHz horizontal polarization case is observed over a large dynamic range as the emissivity increases (Fig. 3.13(b)). Furthermore, the differences become larger in the desert and snow cover areas where surface scattering is present.

3.4.3 Assessment of DMSP F-16 SSM/I-like Channels Performance

Orbit data for F-16 SSMIS and F-15 SSM/I have been processed to a 1/3 degree grid for easy comparison. Because the time difference between DMSP F-15 and F-16 is within 30 minutes, most retrieval products will not be affected much by such a small time variation except for the rain rate, which is more temporally variable. The products, including TPW, LWP, LST, Snow Cover, Sea Ice Cover, and land emissivity are retrieved both by SSM/I and SSMIS. It is shown that the retrievals from both sensors demonstrate a high level of agreement with each other. The statistical results based on the seasonally averaged data for TPW, LWP, LST, RR, and emissivity for five SSM/I channels are listed in Table 3.6. Both the relatively small mean bias and standard deviation prove that F-16 SSMIS data can be successfully used for the retrievals previously developed for use with SSM/I channels. However, retrievals sensitive to 85.5 GHz measurements, such as the land surface temperature and the land emissivity, display some biases. For example, over the Sahara desert LST retrieved from F-16 is slightly lower than that from F-15 while

there are no significant biases over non-desert areas. Because the LST retrieval algorithm uses the quadratic term of the vertically polarized 85.5 GHz brightness temperature, the higher scattering features of the 91.655 GHz band in F-16, despite being remapped to 85.5 GHz, might be the source of the biases. Therefore, the F-16 SSMIS to SSM/I remapping algorithm requires further improvement beyond the simple linear remapping algorithm used to correct the change from 85.5 to 91.655 GHz, which cannot account for scattering and emission effects under all weather and surface conditions.

In this chapter, an introduction on DMSP F-16 SSMIS scan geometry, channel frequency, calibration and validation were given to indicate that this new generation microwave instrument may provide high resolution top quality microwave satellite data on cloud physics study, particularly for strong deep convections associated with large ice particles. In the next chapter, an ice cloud parameter retrieval method is introduced and then improved to be applied on SSMIS high frequency channel measurements to infer ice particle effective diameter and ice water path. Retrievals over severe weather conditions, such as hurricane and multiple cell severe storms, and theoretical error analysis as well as indirect comparison to observations will be given to evaluate the retrieval quality.

Chapter 4: Retrieval of Ice Cloud Parameters Using DMSP F-16 SSMIS TDR

In addition to the considerations raised for the retrieval algorithms evaluated in the previous section, additional issues are also notable. For example, rain rate retrievals along coastal regions or along sea ice boundaries always give some non-zero values. This may be due to the mixture of land and ocean or sea ice surface types embodied within a single footprint while using an emission-based algorithm. Fortunately, because DMSP F-16 SSMIS contains not only imaging channels but environmental channels at 150 and 183.31 GHz, new algorithms based on particle scattering will be developed for precipitation estimation. This new SSMIS algorithm will allow rain rate to be inferred by using the direct relationship to cloud ice water path (*IWP*). Meanwhile, the *IWP* retrieval will directly use channel measurements at 91.655 GHz. Thus, there is no need for remapping F-16 SSMIS and SSM/I for precipitation studies.

In this chapter, an retrieval method for precipitation size ice particle effective diameter and *IWP* is going to be introduced and improved so as to be applied on DMSP SSMIS high frequency channels. The application of this algorithm on selected severe weather conditions, such as hurricanes and multicell strong storms, is also going to be presented. The operational *IWP* retrieval from different instruments is used to evaluate our algorithms. The error analysis of the algorithm will be conducted for future improvement.

4.1 Methodology

4.1.1 Radiative Transfer in Ice Clouds

At microwave frequencies, if we assume a single layer of ice cloud, the radiative transfer through an ice cloud layer can be approximated by a two-stream model as shown in the schematic diagram Fig. 4.1.

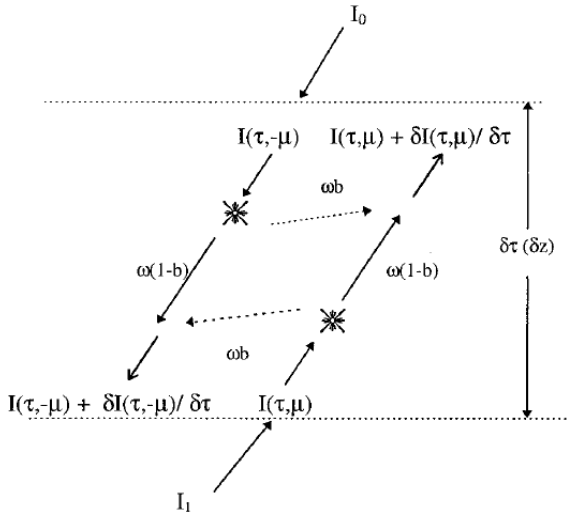

Figure 4.1: Schematic diagram of the two-stream radiative transfer in an ice cloud layer (Weng and Grody, 2000)

From the radiative transfer equation,

$$\mu \frac{dI(\tau,\mu)}{d\tau} = I(\tau,\mu) - \frac{\omega_0}{2}\int_{-1}^{1} P(\mu,\mu')I(\tau,\mu')d\mu' - (1-\omega_0)B_v .$$

With the assumption of a one layer two-stream case, only the zero-th and the first moment of the phase function $P(\mu,\mu') = \sum_{l=0}^{\infty}(2l+1)\chi_l L_l(\mu)L_l(\mu')$ are retained. After mathematic manipulation and the introduction of several approximations (shown in the Appendix), the solution of the radiative transfer equation for such a one layer two-stream model can be obtained as:

$$I(\tau,\mu) = \frac{I(\tau_1,\mu) + I(\tau_0,-\mu)\Omega(1-\varpi^2) + 2B_v\Omega\varpi^2}{1+\Omega(1+\varpi^2)}, \tag{4.1}$$

and

$$I(\tau,-\mu) = \frac{I(\tau_0,-\mu) + I(\tau_1,\mu)\Omega(1-\varpi^2) + 2B_v\Omega\varpi^2}{1+\Omega(1+\varpi^2)}, \tag{4.2}$$

where, Ω is the scattering parameter defined as,

$$\Omega = \frac{\kappa\tau_1}{2\varpi} = \frac{\kappa\tau_1}{2}\sqrt{\frac{1-\omega_0 g}{1-\omega_0}}, \tag{4.3}$$

and where ϖ is a similarity parameter, g is an asymmetry factor in the phase function, and ω_0 is the single scattering albedo.

Because the similarity parameter ϖ is generally smaller than 1 at microwave frequencies, the $\Omega\varpi^2$ term in Eq. 4.1-4.2 is much smaller than 1 and can be ignored with a reasonable approximation. Meanwhile, at the top of atmosphere (TOA), the downward radiance, $I(\tau_0,-\mu)$, is close to null due to the extremely low cosmic background radiation. Therefore, the radiative transfer equation solutions can be simplified to:

$$I(0,\mu) \approx \frac{I(\tau_1,\mu)}{1+\Omega} \tag{4.4}$$

and

$$I(\tau,-\mu) \approx \frac{I(\tau_1,\mu)\Omega}{1+\Omega} \quad . \tag{4.5}$$

The upwelling (Eq. 4.4) and downwelling (Eq. 4.5) radiances (or brightness temperatures) in microwave frequencies are then directly proportional to the incident radiation at the cloud lower boundary, $I(\tau_1,\mu)$. For a space-based platform above the

ice clouds, the upwelling radiance decreases as the scattering parameter increases. Conversely, the downwelling radiance, observed from a ground-based instrument looking upward, increases as the scattering parameter increases. The variation of the scattering parameter may result from changes in the cloud ice water path and particle size. Therefore, the determination of the scattering parameter Ω is critical for the retrieval of *IWP* and *De*.

To determine the relationship between the scattering parameter Ω and *IWP*, the optical depth is introduced as

$$\tau = \int_{z_b}^{z_t} dz \int_0^{\infty} \frac{\pi}{4} D^2 Q_{ext}(x,m) N(D) dD \,, \tag{4.6}$$

where *N(D)* is the particle size distribution function, Q_{ext} is the extinction efficiency of ice particles, *x* is the function of particle size, and *m* is the complex refractive index.

Meanwhile, *IWP* can also be related to the particle size distribution by,

$$IWP = \int_{z_b}^{z_t} dz \int_0^{\infty} \frac{\pi}{6} \rho_{ice} D^3 N(D) dD \,, \tag{4.7}$$

where ρ_{ice} is the ice particle bulk density.

For mono-dispersed particle size, the relation between *IWP* and τ can be derived from Eq. 4.6-4.7 as

$$\tau = \frac{3}{2} \frac{IWP}{\rho_{ice} D} Q_{ext}(x,m) \tag{4.8}$$

so that

$$\Omega(\mu) = \frac{IWP}{\mu \rho_i D} \Omega_N(x,m) \,. \tag{4.9}$$

For poly-dispersed particle size, if we use a gamma function to describe the particle size distribution and define the particle effective diameter as

$$D_e = \frac{\int_0^\infty N(D)D^3 dD}{\int_0^\infty N(D)D^2 dD}, \tag{4.10}$$

the scattering parameter can be shown to be

$$\Omega(\mu) = \frac{IWP}{\mu \rho_i D_e} \Omega_N(x_e, m). \tag{4.11}$$

In either case, the relation between *IWP* and *De* can be given by

$$IWP = \mu \rho_i D_e \frac{\Omega(\mu)}{\Omega_N(x_e, m)}, \tag{4.12}$$

where the normalized scattering parameter is defined as $\Omega_N = \frac{3}{4} Q_{ext}(1 - \omega_0 g)$.

From Eq. 4.12, the *IWP* can be retrieved if the ice particle bulk density, the particle diameter, scattering parameter, and the corresponding normalized scattering parameter are known. In the next section, the determination of these parameters will be introduced for the *IWP/De* retrieval.

4.1.2 Retrieval Algorithms

For one layer ice clouds, when the upwelling brightness temperature at the bottom of ice cloud, $T_b(z_{bottom}, \mu)$, is known, the scattering parameter Ω can be obtained by combining Eqs. 4.4 and 4.5, as shown in Eq. (4.13), to obtain:

$$\Omega(\mu) = \frac{T_b(z_{bottom}, \mu) - T_b(z_{top}, \mu)}{T_b(z_{top}, \mu)}, \tag{4.13}$$

Because brightness temperature at millimeter wavelengths is sensitive to both *IWP* and D_e of precipitating cold cloud ice particles, dual-frequency measurements are required to unambiguously determine both *IWP* and *De* for a given particle bulk density ρ_{ice} (Evans and Stephens 1995b). The theoretical relationship between the normalized scattering parameter (Ω_N) and the particle effective diameter (*De*) is plotted in Fig. 4.2a using simulated data from a simplified radiative transfer model (Weng 1992). The scattering scheme in this model is based on Mie theory, which is used for both scattering and absorbing property determination. Several other assumptions are made. Cloud ice water content is randomly generated within a range of 0 to 0.5 g / m^3. The ice cloud base is set to a height of 9 km with a thickness of 1 km. The ice particle effective diameter randomly varies within a range of 0.1 to 3.5 mm. The incident radiation at the cloud base is set to a constant corresponding to a temperature of 280 K, which indicates a middle level cloud type.

Previous studies have shown that the brightness depression caused by precipitating cold cloud ice particle scattering effects within ice clouds can be accurately captured by microwave bands from 85.5 GHz to 220 GHz, even though the scale varies with the spectrum (Liu and Curry 2000; Weng and Grody 2000; Greenwald and Christopher 2002; Bennartz and Bauer 2003). Because the 183.31±6.6 GHz frequency band is sensitive to middle to high troposphere ice clouds, less affected by surface emissivity, and more sensitive to smaller ice particle sizes compared to 150 GHz, but less affected by the water vapor contents in the near altitudes compared to 183.31±1.0 GHz channel (Muller *et al.* 1994), the

measurements at 91.655 GHz and 183.31±6.6 GHz are chosen in this study for the retrieval to make the retrievals cover a broader ice particle size range.

Shown in Fig. 4.2 is the theoretical relation plotted among ice particle effective diameters, normalized scattering parameters, and the ratio of dual-channel normalized scattering parameters constructed from the model simulations. In Fig. 4.2(a), for extremely small ice particles, the normalized scattering parameters of both 91.655 GHz and 183.31±6.6 GHz approach zero, which indicates that both channels cannot "see" small ice particles. As the ice particle size increases, the sensitivity of both channels also increases but at different rates. The rate of increase for the normalized scattering parameter Ω_N at 183.31±6.6 GHz is higher than for the 91.655 GHz channel. However, Ω_N at 183.31±6.6 GHz quickly reaches its optical limit around 1.5 mm, which means the scattering effect is saturated, while Ω_N at 91.655 GHz continues in an increasing phase for *De* beyond 1.5 mm. The normalized scattering parameter for 91.655 GHz eventually reaches to its optical limitations as the ice particle diameter grows to about 3.0 mm. Meanwhile, the scattering parameter at 183.31±6.6 GHz does not show significant variation but a slight decrease for *De* larger than 1.5 mm. From this simulation plot, it is found that the retrievals are most reliable when the ice particle effective diameters are within 0.5 to 2.5 mm. For ice particles outside this range, the results are not accurate due to the channel optical limitations. It should be mentioned that the outliers around the line are due to the randomly generated ice particle size in model simulations.

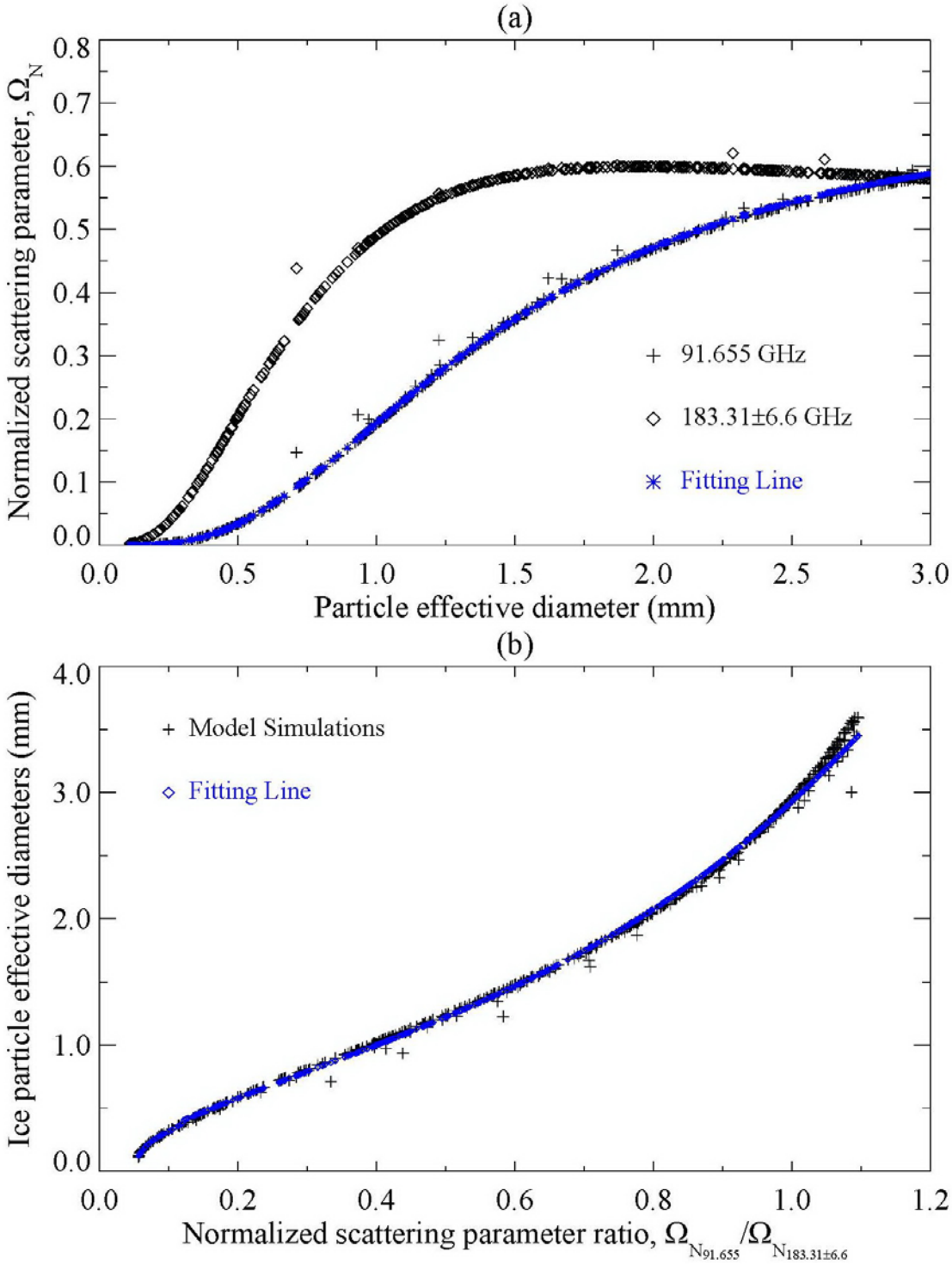

Figure 4.2: (a) Normalized scattering parameter as function of the particle effective diameter derived using a gamma size distribution; (b) the particle effective diameter as a function of the ratio between the scattering parameters at 91.655 and 183.31±6.6 GHz

To determine ice particle effective diameter, *De*, from dual-frequency channels, a scattering parameter ratio *r* for the 91.655 and 183.31±6.6 GHz channels is defined in Eq. 4.14 as

$$r(D_e) = \frac{\Omega_{91.655}}{\Omega_{183.31\pm6.6}} = \frac{\Omega_{N_{91.655}}(x_e, m)}{\Omega_{N_{183.31\pm6.6}}(x_e, m)} \quad . \tag{4.14}$$

Fig. 4.2(b) gives the relationship between the scattering parameter ratio *r* and the particle effective diameter *De* from the model simulations. To infer ice particle effective diameter from the scattering parameter ratio, the multiple regression fit of the normalized scattering parameter at 91.655 GHz and the ice particle effective diameter are also performed using Eqs. 4.15 and 4.16, respectively.

$$D_e = a_0 + a_1 r + a_2 r^2 + a_3 r^3 \tag{4.15}$$

$$\Omega_N = \exp[b_0 + b_1 \ln(D_e) + b_2 \ln^2(D_e) + b_2 \ln^3(D_e)] \tag{4.16}$$

Table 4.1 gives the coefficients for the regression fitting equations. For the dual-frequency measurements at 91.655 and 183.31±6.6 GHz, reliable results are expected when the ratio ranges from 0.2 to 0.8.

Table 4.1: The coefficients used in the D_e and IWP retrieval algorithm

D_e	a_0	a_1	a_2	a_3
	-0.314	4.175	-5.614	5.228
IWP	b_0	b_1	b_2	b_3
	-1.645	1.910	-1.039	0.203

The regression fits of $\Omega_{N_{91.655}}$ and *De* using the derived coefficients are presented by the blue line in Fig. 4.2(a) and (b). If the upwelling brightness

temperature at the bottom of the ice cloud is known, the channel scattering parameter can be calculated by Eq. (4.12). Thus, *De* and *IWP* can be estimated from Eqs. 4.13-4.15 for a given ice particle bulk volume density.

4.1.3 Estimation of Cloud Base Temperature

As described in Eq. 4.13, to get the scattering parameter, brightness temperatures at both top and bottom of an ice cloud need to be known. For one layer ice cloud, the brightness temperature at the cloud top is actually the observation of the instrument. The question goes to how to estimate the cloud base brightness temperature.

Under clear sky conditions, the brightness temperatures approximately follow a linear relationship for microwave frequencies, which indicates that the cloud base upwelling incident brightness temperature at 91.655 and 183.31±6.6 GHz can be estimated from lower frequency channels of 19.35 and 22.235 GHz. For ice cloud covered conditions, because both low frequency microwave channels can penetrate the clouds, these two channels can be used to predict the cloud base temperature with good confidence.

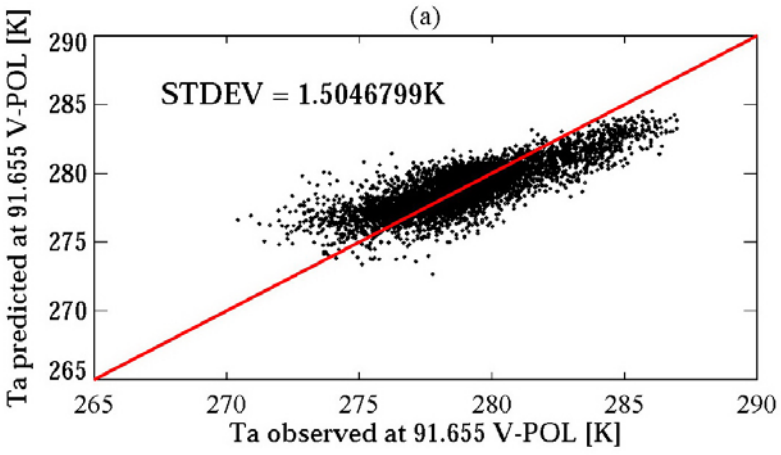

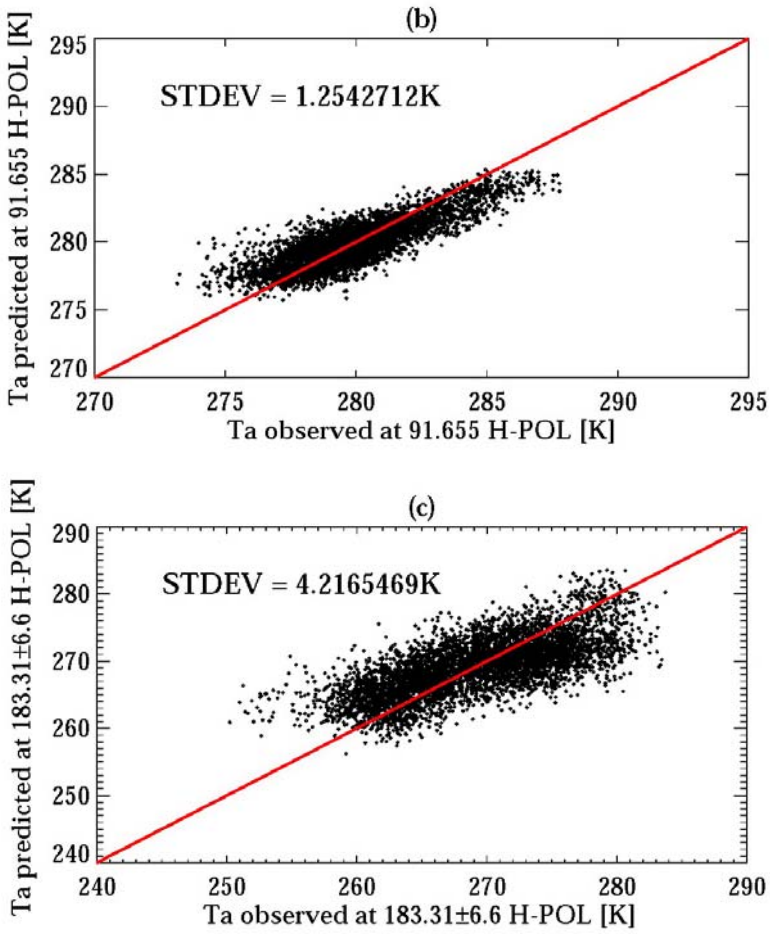

Figure 4.3: Comparison between measurements and estimates based on a regression relationship for the cloud base brightness temperature at several channels: (a) 91.655 GHz V-POL, (b) 91.655 GHz H-POL, and (c) 183.31±6.6 GHz H-POL

In our study, a set of empirical equations constructed between the SSMIS lower frequency channels (19.35 and 22.235 GHz) and higher frequencies (91.655 and 183.31±6.6 GHz) are applied to estimate the ice cloud base brightness temperature. The relation is built by brightness temperatures collected under cloud-free conditions at each matched environmental channel footprint scene. The cloud-free location is identified by cloud liquid water path over ocean (Weng and Grody 1994) and rainfall free over land (Ferraro and Marks 1995) using DMSP SSMIS heritage algorithms.

Shown in Fig. 4.3a-c is the scatter plot of estimated brightness temperatures versus observed brightness temperature at 91.655 and 183.31±6.6 GHz under clear sky conditions over land surface. The statistical analysis shows that the cloud bases can be estimated with a standard deviation of about 1.5 K at 91.655 GHz and about 4.25 K at 183±6.6 GHz over land. Smaller standard deviations are shown in the case of ocean areas due to the smoother surface conditions. However, the relatively bigger standard deviation in the 183.31±6.6 GHz channel also indicates that the prediction of cloud base temperature may introduce additional uncertainties in the retrieval of ice cloud parameters, which will be discussed in the error analysis section.

4.2 Retrieval of Ice Particle Effective Diameter and Ice Water Path

Presented in the Fig. 4.4 is a flow chart for retrieval of *IWP/De* from the original DMSP SSMIS TDR.

As described in previous sections, the original TDR data first undergoes a recalibration process. Then, data from different subunits are footprint matched to the IMG original resolution within about 25 km. The cloud base temperature at 91.655 GHz V-POL and 183.31±6.6 GHz V-POL are estimated using footprint matched 19.35 GHz V/H-POL and 22.235 GHz V-POL. The scattering parameter as well as the ratio of scattering parameters can then be obtained. Finally, both *IWP* and *De* will be retrieved simultaneously by the proposed retrieval algorithm.

In this section, two severe weather cases associated with deep convection are selected to demonstrate the application of the retrieval algorithm. One is the hurricane during landfall; the other is a multicell storm over land.

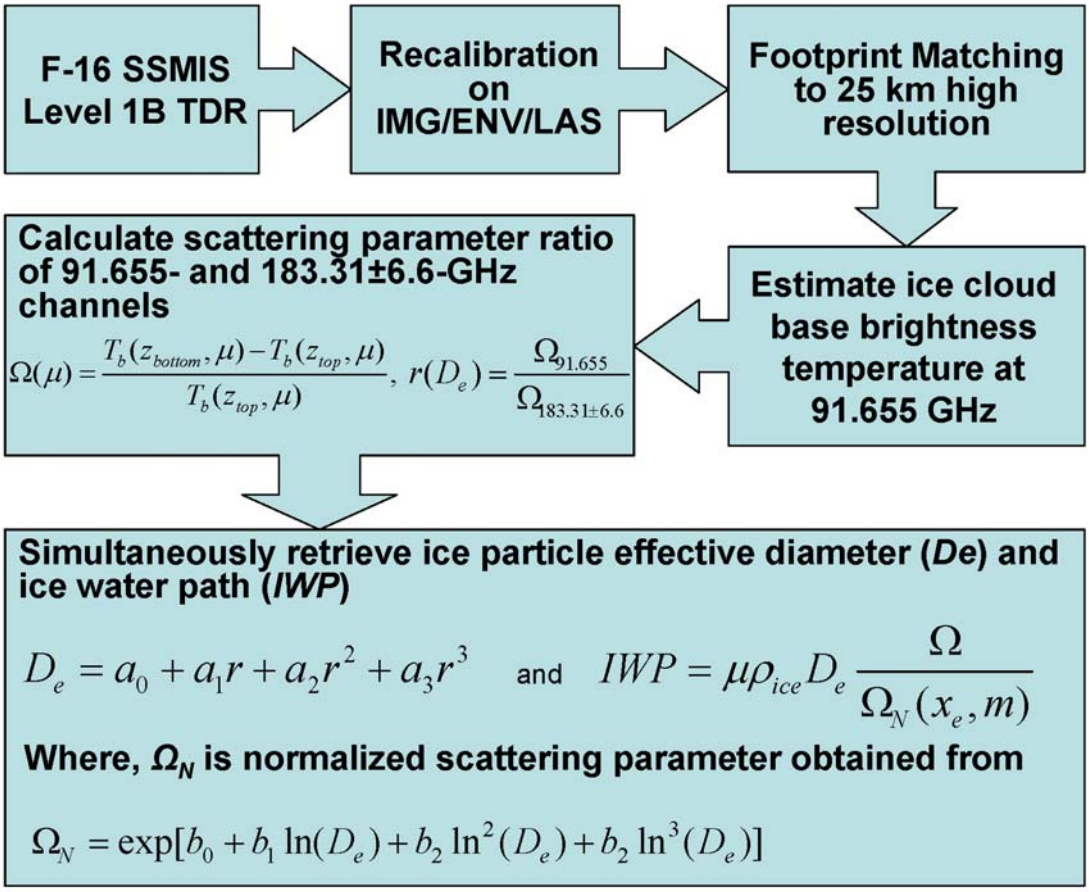

Figure 4.4: Flow chart of the retrieval of IWP/De from DMSP SSMIS TDR

4.2.1 Hurricane Case Study

Hurricane Gustav was one of the most destructive hurricanes of the 2008 Atlantic hurricane season. It caused serious damage and casualties in several countries in the Caribbean and triggered the largest evacuation in United States history. Gustav formed on August 25, 2008 southeast of Haiti and rapidly strengthened into a tropical storm that afternoon and further into a hurricane by early the next day. It remained at Category 2 intensity until landfall on the morning of September 1, 2008 in Louisiana.

The D_e and *IWP* retrievals at the time of landfall of Hurricane Gustav on September 1, 2008 EST are presented in Fig. 4.5a-b. Typical hurricane features, such

as the eyewall, spiral rainfall bands associated with large *IWP* of more than 2 kg/m^2, and D_e close to 1.5 *mm* are consistently present in the *IWP* and *De* retrievals. Because the hurricane moved northeastward after landfall, the maximum spiral rainbands occur to the right side of the hurricane track, where the most dangerous part of the hurricane exists due to the additive effect of the vortex wind speed and the broader atmospheric flow. The relatively calm eye and downdraft areas between the spiral bands are also clearly shown. Away from the eyewall and the heavy rain bands, the ice particle effective diameter shows a large area of quite uniform particle size smaller than 0.3 mm in Fig. 4.5(b), which corresponds well to the scattering parameter optic limits below 0.3 mm in Fig. 4.2(a) for 91.655 GHz. This indicates that the retrieval over these areas might not be as reliable as in other regions.

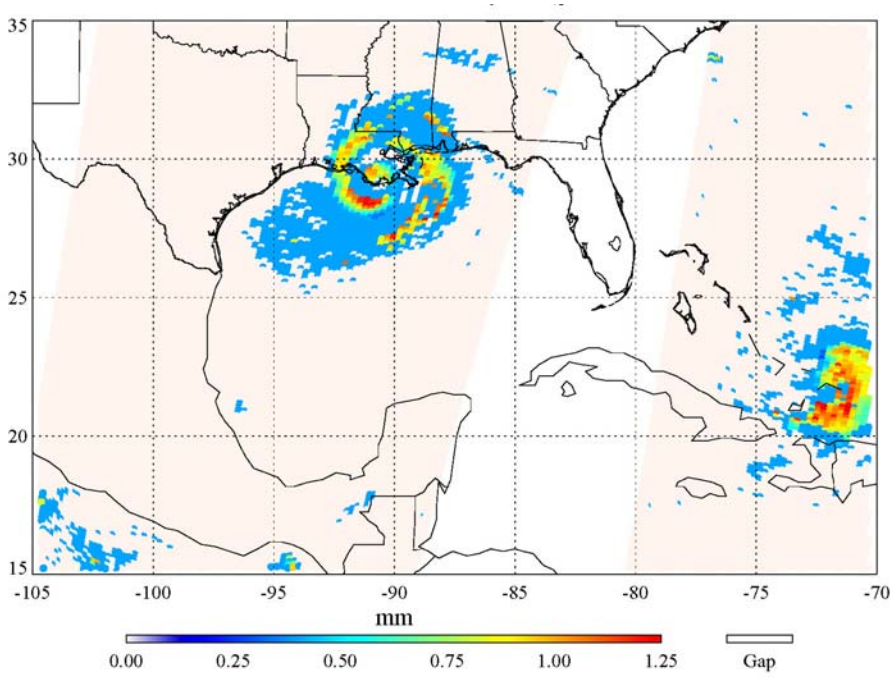

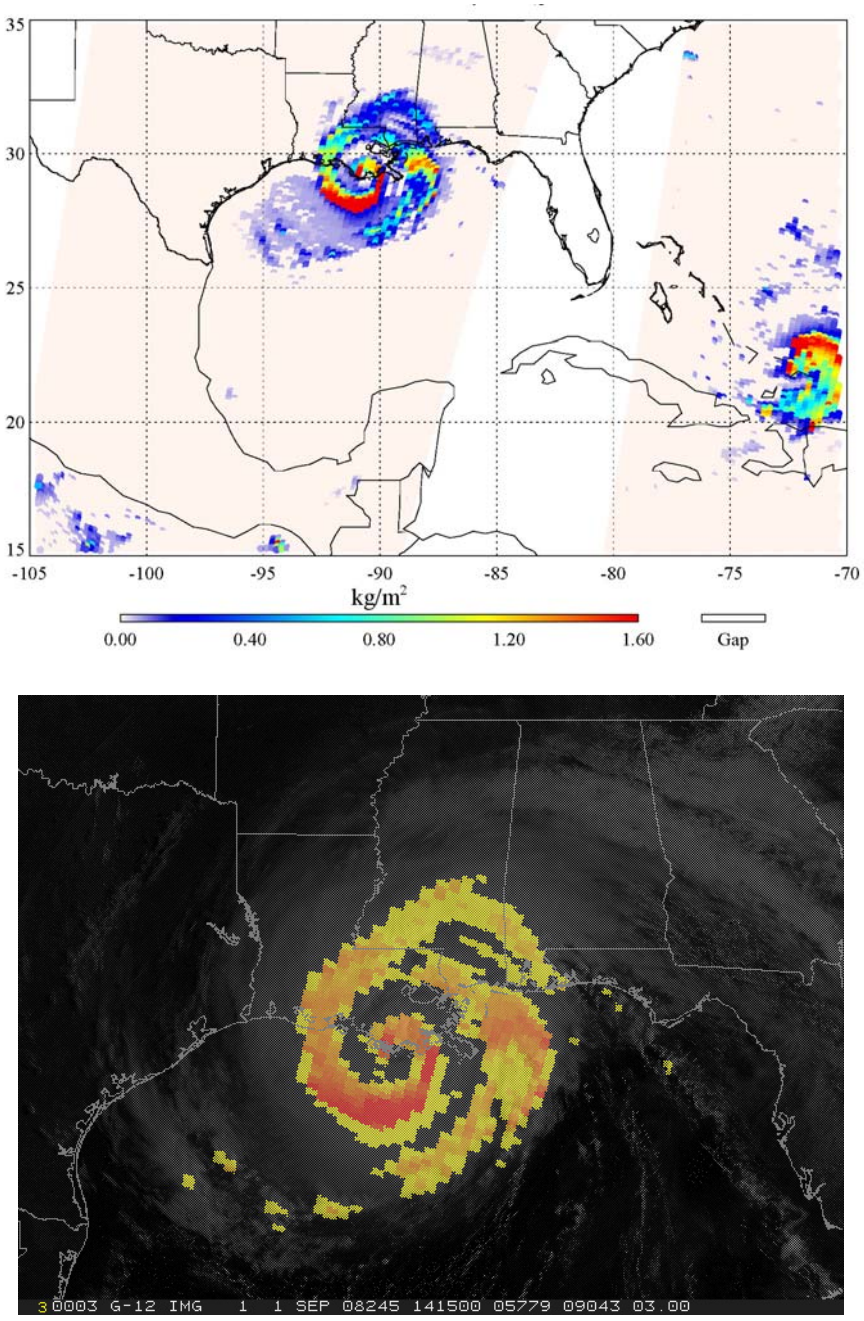

Figure 4.5: (a) Ice particle effective diameter; (b) ice water path; and (c) GOES-12 and ice water path in a superimposed plot for hurricane Gustav at the time of landfall on September 1, 2008 UTC

The smooth transition of D_e and *IWP* from the ocean to the land proves that the estimation of cloud base temperatures for ocean and land are quite accurate. The

surface impacts from different surface types can actually be minimized through the multiple regression prediction method so that the quality of *IWP* retrievals can be assured. Because D_e is only determined by the scattering parameter but the *IWP* is determined by not only by D_e but also the ratio of the scattering parameter and the normalized scattering parameter, as well as the depth of the ice cloud, a large D_e does not necessarily correspond to a large *IWP* or vice versa, which is the reason why the location of maximum *De* is not exactly the same location as the maximum of *IWP*.

However, it should be pointed out that the brightness temperature at 183.31±6.6 GHz may be heavily affected by the water vapor content associated with the ice clouds so that the brightness temperature depression by ice particle scattering effects may be significantly offset, which indicates a smaller scattering parameter in this channel. As a result, the retrieved *De* may be larger than the real value.

Shown in Figure 3c is the superimposed plot of Geostationary Operational Environmental Satellite (GOES-12) visible channel image at 14:15 UTC on September 1, 2008 and the *IWP* retrieval demonstrated earlier. It is observed that most of precipitation ice clouds exist near the hurricane eye, even as the clouds are distributed over a huge area in the visible channel image. Due to its high capability to deep penetrate into clouds for internal structure sensing, the microwave instrument greatly helps to identify the large particles and heavy rainfall locations, which cannot be easily distinguished by visible or infrared channels under such severe weather conditions because of their optical limitations.

4.2.2 Mid-latitude Multicell Storms Case Study

A mid-latitude multicell storm captured by the DMSP F-16 SSMIS during the evening of April 3, 2007 EST is presented in Fig. 4.6a-b.

The multicell storm extended in the northeastern-southwestern direction with a distinct and strong leading-edge thunderstorm belt. There are at least three strong updraft cells clearly shown along the cold forward front line. Because the strong updrafts associated with the supercells are favorable for the creation of large ice particles such as graupel or hail, moderate to large ice particle effective diameters generally exist along the leading edge of the storm.

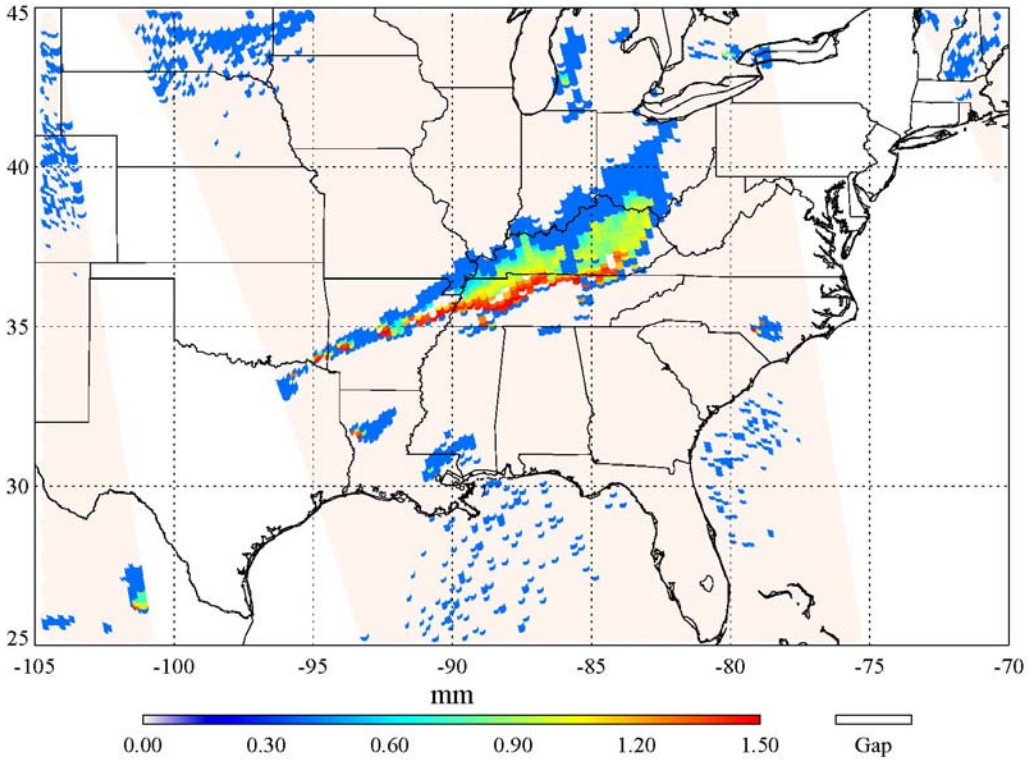

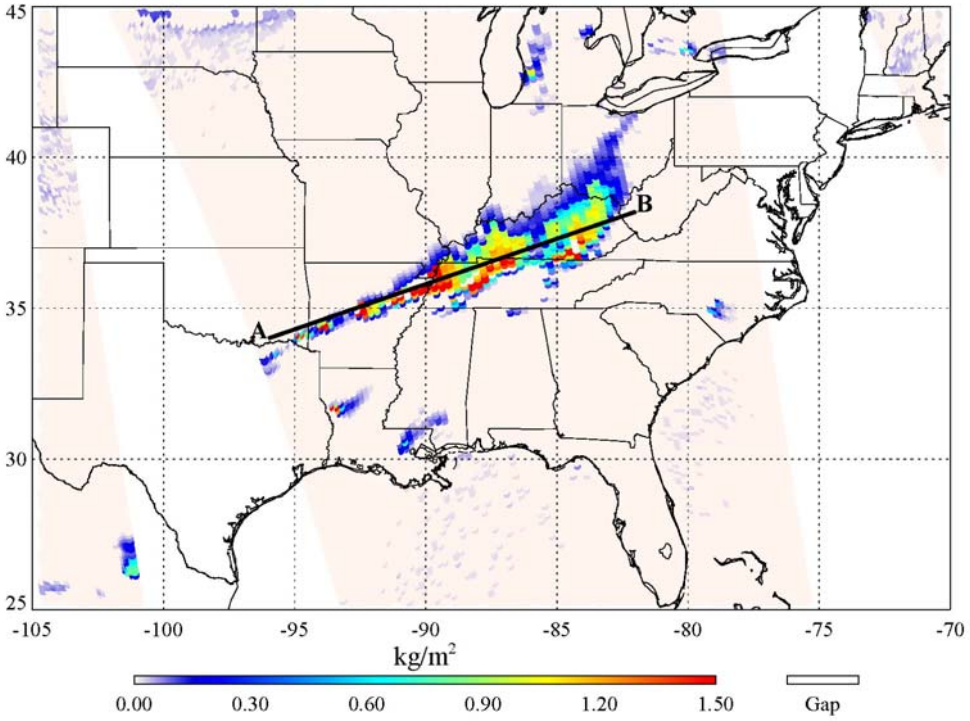

Figure 4.6: Same as in Fig. 4.5, but for mid-latitude multicell storm on April 3, 2008

However, the fairly different discrete distribution pattern shown in the *IWP* figure (Fig 4.6b) once again proves that the *IWP* is not exclusively related to the *De*. Actually, the bulk ice density, scattering parameter, and normalized scattering parameterd interactively determine the *IWP*. Following the leading strong updraft belt, there is a large area of relatively stratified clouds with smaller ice particles.

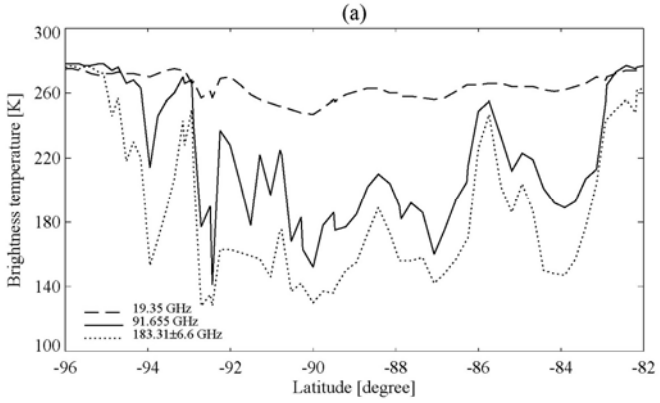

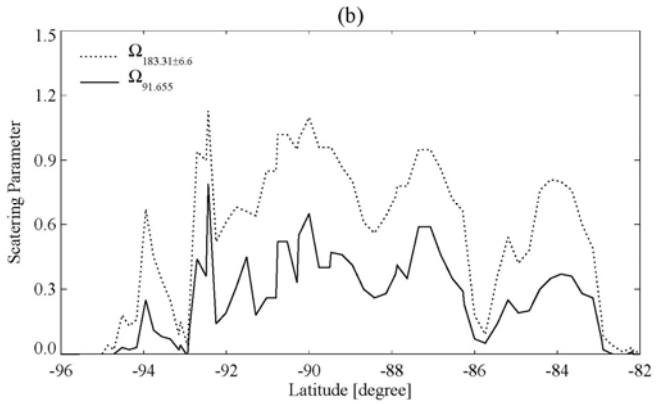

Figure 4.7: (a) The brightness temperature measured by DMSP F-16 SSMIS along the cross-section between A and B at 19.35, 91.655, and 183.31±6.6 GHz; (b) the scattering parameter at 91.655 and 183.31±6.6 GHz.

Fig. 4.7 a-b give the brightness temperature measurements at the 19.35, 91.655, and 183±6.6 GHz channels and the corresponding calculated scattering parameters in the *IWP* retrieval along the cross-section between A and B shown in Fig 4.6(b), respectively. Because the instrument observations actually reflect the cloud top optical signals, the relatively stable brightness temperature at 19.35 GHz indicates that there are very limited impacts on the low frequency channels. However, the lower brightness temperatures at 183±6.6 and 91.655 GHz are the result of particle scattering effects. Most of the brightness temperatures of these two channels are in good correspondence. However, some big brightness temperature depression at 91.655 GHz may not be shown at 183±6.6 GHz, such as between 92^{O}W and 91^{O}W, where the sharp peak to valley change shown in the 91.655 GHz plot is not quite clear at 183±6.6 GHz. A possible explanation is that the clouds within these longitudes are actually in a large mixing phase so that the water vapor effects offset the scattering signal at 183±6.6 GHz. The multiple peaks in the scattering parameter plots indicate that there may be several individual strong updrafts, and the large values also indicate

that these updrafts are also possibly associated with large ice particles, which have been clearly illustrated in the retrievals of D_e and *IWP* even though the magnitudes are smaller than those of the hurricane case.

4.3 Evaluation of IWP Retrievals

The retrieval algorithm in this study is applied for mid-altitude precipitating ice cloud microphysics. Neither direct observations in a recent field campaign for this cloud type nor *IWP* derived from other methods suitable for closely (temporally) matched evaluation are available. For instance, CloudSat IWP retrievals are about 6 hours earlier than the DMSP F-16 SSMIS local scan.

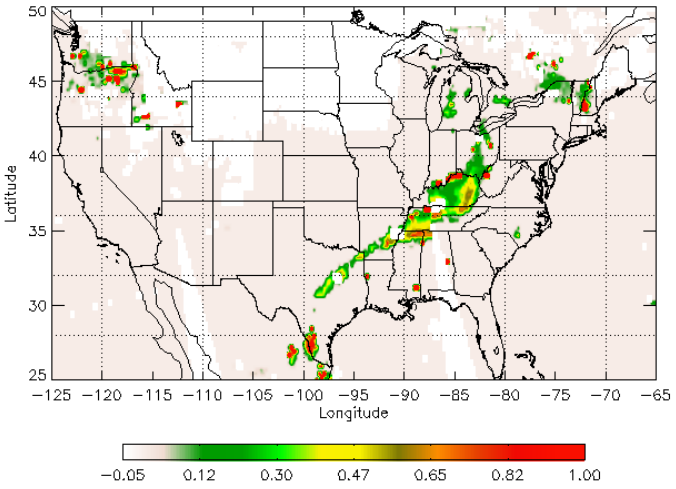

Figure 4.8: Same as in Fig. 4.6(b), except for retrieval from MetOp-A in MSPPS

For qualitative comparison purposes, the *IWP* retrieved from MetOp-A in the Microwave Surface and Precipitation Products System (MSPPS) (Ferraro *et al.* 2005) on the same day is also presented in Fig. 4.8. The MSPPS project is dedicated to the retrieval of near-real-time operational surface and precipitation products using antenna temperatures from the AMSU-A and AMSU-B/MHS instruments on board

NOAA's K/L/M/N/N' series and the EUMETSAT Polar System's (EPS) MetOP series of polar-orbiting satellites. This project has advanced from 5 products at its Day-1 phase to 9 products at the Day-2 phase. The current Day-2 MSPPS products include rain rate and falling snow, total precipitable water, cloud liquid water, snow cover, snow water equivalent, sea ice concentration, ice water path, emissivity (23.8 GHz, 31.4 GHz, and 50.3 GHz), and land surface temperature.

Please note that the local scan time of F-16 is about two hours earlier than that of MetOp-A, so Fig. 4.8 actually indicates results from two hours later than Fig. 4.6. From the figure, the multiple cell structure can still be identified clearly even after two hours of additional development. However, the structure is slightly changed compared to that from DMSP F-16 SSMIS, and the *IWP* in the storm center areas are smaller than those retrieved from F-16, which may be caused by both the dissipation of the weather system and instrument differences. It is also worthwhile to note that there are large areas in the northern part of the American midwest which are flagged as non-retrievable, and these are areas which are resolved in the SSMIS retrievals by applying different coefficients for different surface type estimated from SSMIS low frequency channels.

4.4 Error Analysis of Retrievals

As pointed out earlier, several major uncertainties in the retrievals of cloud ice water path, such as ice particle bulk volume density, scattering parameters, and ice particle effective size, may affect the quality of retrievals. In this section, the error caused by these uncertainties will be discussed.

4.4.1 Error in Ice Particle Effective Diameter Retrieval

The ice particle effective size is obtained through the regression relationsship between *De* and scattering parameter ratio r from Eq. 4.13, derived from the physical model (Weng and Grody 2000). Therefore, the indeterminate error of the particle effective diameter retrieval can be determined by:

$$\frac{\Delta D_e}{D_e} = f_1(D_e, r)\frac{\Delta r}{r}, \tag{4.17}$$

where

$$\frac{\Delta r}{r} = g(T_{B_{bottom}}, T_{B_{top}})\left(\frac{\Delta T_{B_{bottom}}}{T_{B_{bottom}}} - \frac{\Delta T_{B_{top}}}{T_{B_{top}}}\right) . \tag{4.18}$$

$\Delta T_{B_{bottom}}$ and $\Delta T_{B_{top}}$ represent the error of the brightness temperature estimated at the bottom of ice clouds and observed at the top of clouds, respectively.

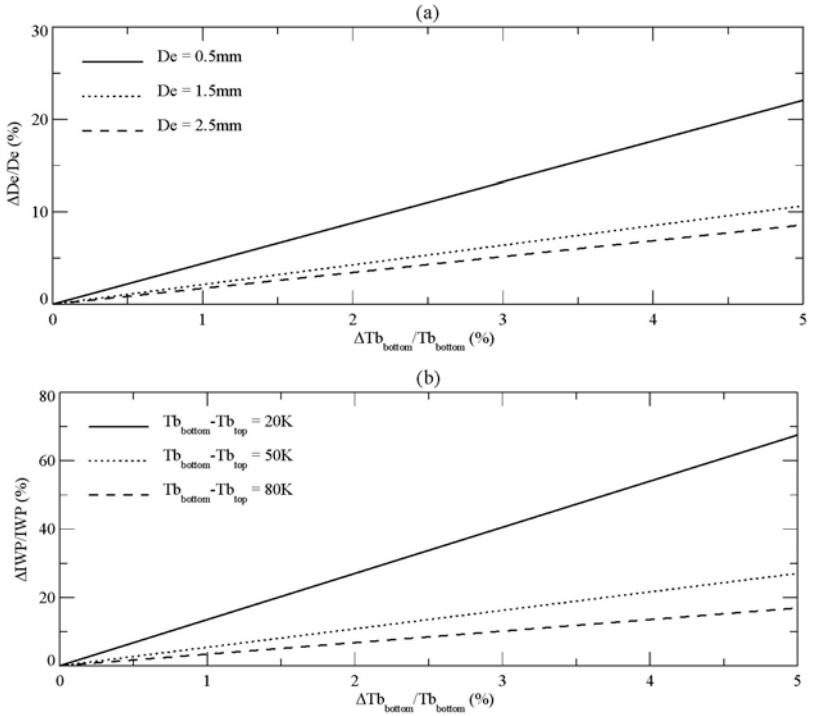

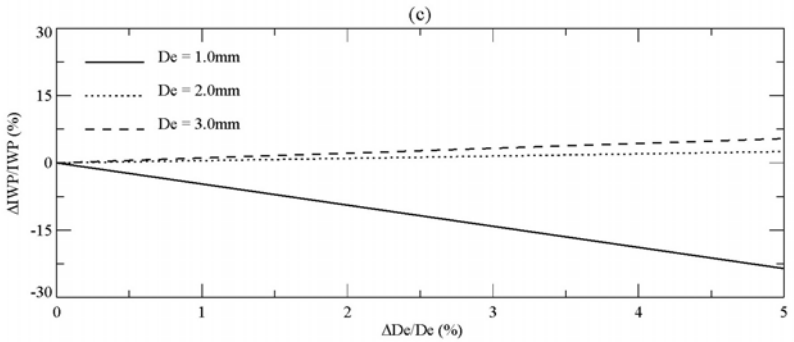

Figure 4.9: The retrieval uncertainties associated with particle effective diameter due to cloud base temperature; (b) ice water path due to cloud base temperature; (c) ice water path due to ice particle effective diameter

With the nonlinear amplifying factor of $f(D_e, r) \times g(T_{B_{bottom}}, T_{B_{top}})$ in Eq. 4.18, the cloud base brightness temperature estimation in both channels, as well as the cloud top brightness temperature detected by the satellites, will affect the particle effective diameter retrieval quality. Figure 4.9a gives the estimation of the impact on the effective diameter retrieval by the cloud base temperature at different particles sizes. It is found that the error in the cloud base temperature will introduce more errors in the smaller ice particle retrievals. However, the impact of cloud base temperature error on *De* retrievals decreases with particle size. A 5K error in the cloud base temperature can result in a 4-8% error for *De* retrievals. As for the cloud top brightness temperature error, the introduced error will not exceed 2% in *De* retrievals because of the relatively low NEΔT at chosen channels.

4.4.2 Error in Ice Water Path Retrieval

Similarly, because the *IWP* retrieval algorithm is a function of ice particle effective diameter, the ice particle bulk volume density, and the scattering parameter, the retrieval error can be analyzed as follows:

$$\frac{\Delta IWP}{IWP} = \frac{\Delta \Omega}{\Omega} + h_1(D_e, \rho_{ice}) \frac{\Delta D_e}{D_e} \quad , \qquad (4.19)$$

where

$$\frac{\Delta \Omega}{\Omega} = \frac{T_{B_{bottom}}}{T_{B_{bottom}} - T_{B_{top}}} \left(\frac{\Delta T_{B_{bottom}}}{T_{B_{bottom}}} - \frac{\Delta T_{B_{top}}}{T_{B_{top}}} \right) \quad . \qquad (4.20)$$

The *IWP* retrieval error is linearly related to the scattering parameter error with the temperature depression, but nonlinearly related to the error of ice particle effective diameter, as shown in Eq. 4.19. The error of the scattering parameter includes two sources from Eq. 4.20. One is from the estimation of the ice cloud base brightness temperature and the other is from instrument noise. For DMSP F-16 SSMIS, the instrument noise of the imager and environmental channels used in this study is smaller than 1K, which alone could only contribute less than 2% of the errors in the scattering parameter for brightness temperature depression higher than 40 K. Thus, the error in estimating the ice cloud base brightness temperature will be a major error source. Fig. 4.9b presents the *IWP* retrieval error caused by the estimated scattering parameter. The error decreases with increasing cloud temperature depression. A 2% error in cloud base temperature estimation will introduce about 10% *IWP* retrieval error for cloud temperature depression greater than 40 K. The effective particle size error demonstrates a different pattern, which is shown in Fig. 4.9c. For smaller ice particles, the underestimate of ice water path increases with the

increase of ice particle size error. On the contrary, the increase of relatively large particle size error causes the overestimat of ice water path increase. .It is also noticed that the error in smaller ice particles has larger impact on the ice water path retrieval.

In this chapter, a precipitation droplet size ice particle effective diameter and ice water path were retrieved simultaneously from DMSP SSMIS high frequency channel measurements at 91.655- and 183.31±6.6 GHz for strong convective cloud types. Error analysis and a direct comparison to currently operational system, MSPPS, ice water path product by different satellite measurements proved that this enhanced ice cloud parameter retrieval algorithm can successfully provide not only comparable retrieval quality but also higher resolution product. In the next chapter, the application of ice cloud parameters on rain rate inference and the generation of global oceanic precipitation climate change time series will be conducted to demonstrate the advantage of DMSP SSMIS data on global climate change study.

Chapter 5: Application of Ice Cloud Parameters to Global Precipitation Climate Change Study

The physical retrieval of rainfall rate over ocean and land by passive and active microwave instruments has been widely explored (Petty 1994; Ferraro and Marks 1995; Petty 1995; Wentz and Spencer 1998; Kummerow *et al.* 2001; Liu and Fu 2001).

DMSP SSMIS high-frequency window channels are also useful in delineating precipitation due to the correlation between ice scattering and the surface rain rate. SSMIS sensitivity to light rain events is significantly improved compared with the previous SSM/I because of the availability of the 150 GHz and double-side band 183.31 GHz channels. Meanwhile, a rain rate of 10 mm/h or larger can also be successfully retrieved due to the use of information at SSMIS 91.655 GHz. In this chapter, the attempt to derive rainfall rate from the retrieved *IWP* is made. The global total precipitation is then estimated from the rainfall rate and used to construct the global precipitation climate change time series since the launch of DMSP F-16. The application of DMSP SSMIS hydrometeor products to global precipitation studies provides a complementary method for monitoring global hydrological climate change.

5.1 Scattering Based Rainfall Rate Retrieval

5.1.1 Methodology

The relationship between the surface rain rate and ice water path is derived using the Goddard precipitation profiling algorithm data sets that contain the profiles of various hydrometeors generated from the cloud models (Kummerow *et al.* 1996).

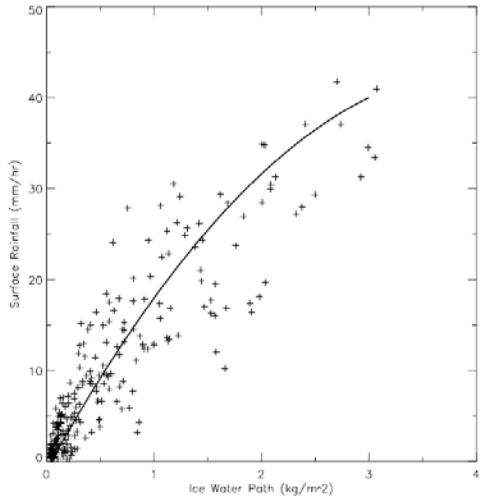

Figure 5.1: Relationship between the surface rainfall rate and cloud ice water path based on the cloud data sets used in the Goddard precipitation profiling algorithm (Weng et al.,2003)

Shown in Figure 5.1 is the relationship between surface rainfall rate and *IWP* based on the Goddard precipitation profiling algorithm generated data sets (Weng *et al.* 2003). Such relationships have been successfully applied to AMSU-B observations, as follows:

$$RR = r_0 + r_1 IWP + r_2 IWP^2 \quad . \qquad (5.1)$$

In most precipitation systems, the rain layer extends above the freezing level, and contains a mixture of water and ice particles. Scattering of the upwelling radiation due precipitation sized ice particles results from within the precipitation layer. Depending upon the cloud microphysics and vertical structures, the *RR* is

retrieved using different sets of coefficients under different cloud types. By adopting similar criteria to those used by the NOAA operational Microwave Surface and Precipitation Products System (MSPPS) (Ferraro *et al.* 2005), the convection index (CI) is always calculated first using three double side-band channels at 183.31±6.6 GHz, 183.31±3 GHz, and 183.31±1 GHz. The *RR* is then derived under different CI conditions.

5.1.2 Comparison to Heritage Rainfall Rate Retrievals

Shown in Fig. 5.2 a-b are rainfall rates of the multicell storm derived from *IWP* and from the heritage retrieval algorithm using the SSM/I-like channels (Ferraro and Marks 1995).

(a)

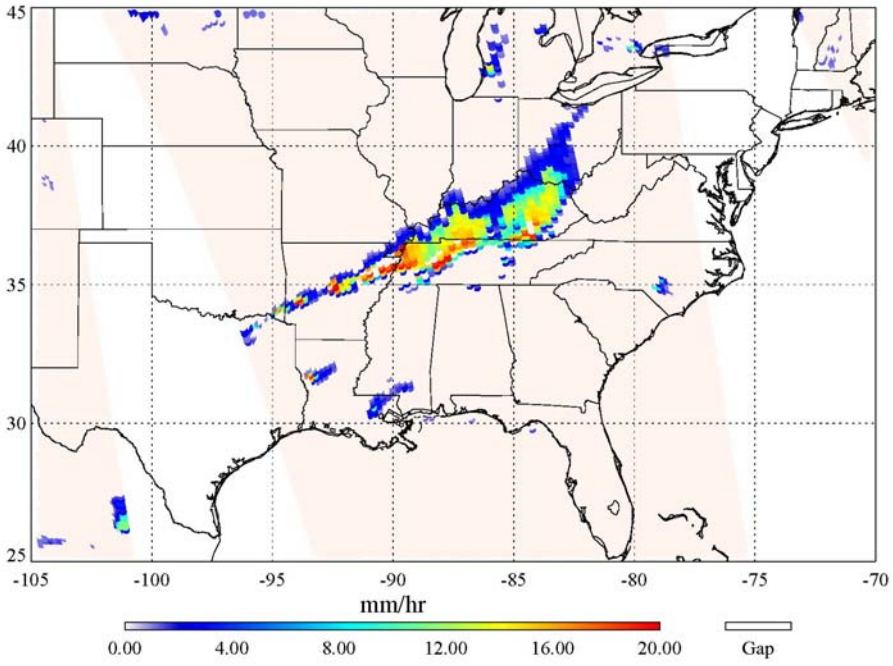

(b)

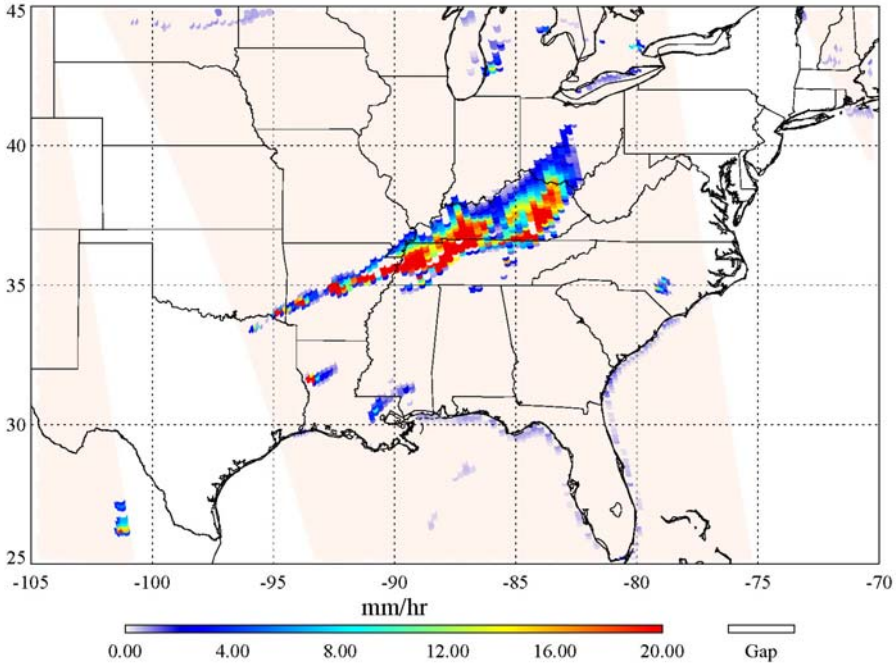

(c)

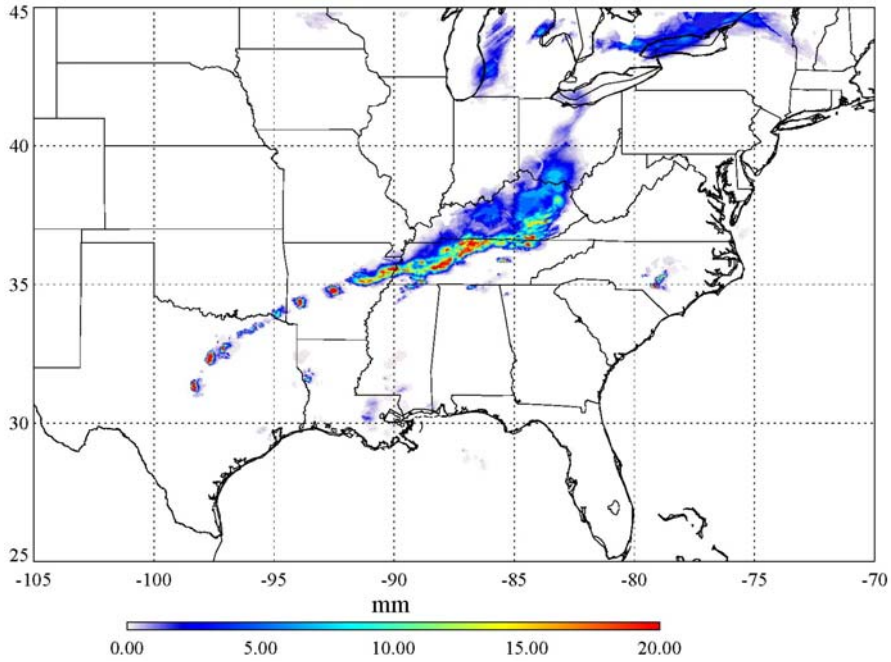

Figure 5.2: (a) rainfall rate derived from ice water path; (b) rainfall rate from NOAA heritage algorithm; and (c) hourly total rainfall derived from the radar reflectivity and gauge observations for the mid-latitude multicell storm on April 4, 2007 (UTC)

It is found that both products well illustrate the multiple heavy rainfall areas corresponding to the multiple cells in the storm. The maximum rainfall rates both

exceed 20 *mm/hr*. However, it should also be noted that the rainfall rate derived from *IWP* is generally smaller than from the heritage algorithm, especially over the stratiform precipitation area, where the smaller *IWP* is dominant, behind the leading strong convection zone. In addition, the new rainfall rate retrieval algorithm can successfully handle the coastal areas without extraordinary contamination due to the mixture of land and ocean signals inside a single *FOV*.

The National Weather Service (NWS) operational synthetic one-hour cumulated rainfall product derived from both radar reflectivity and gauge observations (Fulton *et al.* 1998) around the F-16 SSMIS scan time is presented in Figure 5.2c. For a clear illustration, the scale has been set to the same as the rainfall rate retrieval even thought the units are different. Due to their large difference between F-16 satellite observation FOV and irregular rainfall product geophysical location, point-to-point comparison between SSMIS retrievals and synthetic rainfall observations cannot provide reliable statistic analysis results. Therefore, only a qualitative discussion will be conducted here. From both Fig. 5.2a and 5.2c, the rainfall product clearly shows that the maximum one-hour cumulated rainfall areas along the storm front match very well to the maximum rainfall rates derived from the ice water path by the microwave instrument. The uncertainty still exists in the anvil cloud region behind the leading convection zone, where relatively larger rainfall is shown in the SSMIS retrievals. However, it is noteworthy that, unlike the GOES series satellites, the polar orbital satellite scans a particular geographical location only within a very limited time period so that it is not quite suitable for the analysis of cumulative parameters. Therefore, providing microwave instruments aboard a

geostationary vehicle can dramatically improve the deep cloud property prediction capabilities, especially under the most severe weather conditions.

The new algorithm actually provides an alternative way to retrieve rainfall rate through *IWP* from the DMSP SSMIS series, which was not available preceding the launch of SSMIS. In addition, the rainfall rate retrieved from *IWP* along the coastline performs very well without extraordinary contamination due to the mixture of land and ocean inside the *FOVs*. The top scanning quality, high sampling resolution, and advanced scanning mode of such newly developed microwave sensors could also contribute to better retrieval quality under severe weather conditions.

5.2 Global Oceanic Precipitation Climatology

5.2.1 Methodology

To generate the global total precipitation time series from DMSP SSMIS, the daily rainfall rate is firstly converted to daily precipitation by multiplying the mean value of ascending and descending nodes rainfall rate by 24 within each 0.3 by 0.3 degree grid area. The global total precipitation amount is then obtained by adding all grid point values together. To minimize the uncertainties over snow or ice surfaces, rainfall rate data within only 60^{O}N and 50^{O}S are processed. Because of the scan gaps between orbits, it takes about 5 days to cover the entire global area for DMSP F-16 SSMIS. Therefore, a pentad averaging of daily total precipitation is used to lower the uncertainty introduced by the gaps. In another words, there are approximately 73 pentad averaged time points every year. Simultaneously, two global total precipitation anomaly time series from DMSP F-16 SSMIS are generated for comparison purposes.

One is from the heritage-processed rainfall rate. The other is from the rainfall rate derived using the newer *IWP* retrieval method.

5.2.2 Results and Discussion

Shown in Fig. 5.3 a-b is the global oceanic total precipitation and frequency pentad anomaly time series derived from *IWP* using the method mentioned above for the period between January 2005 and September 2009.

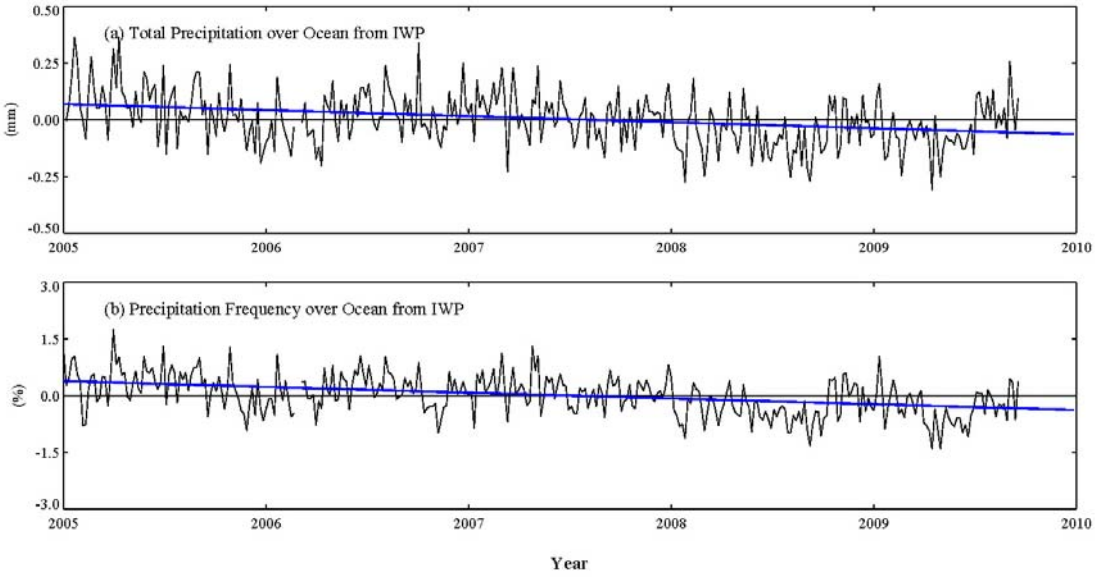

Figure 5.3: Climate anomaly time series between January 2005 to September 2009 of oceanic (a) total precipitation derived from IWP, and (b) precipitation frequency

It is clearly shown that both global total precipitation and precipitation frequency over ocean have a decreasing trend during the study period. The trend is equal to about 0.27 *mm* per decade.

For comparison purposes, the same CDR products from heritage RR retrieval are also presented in Fig. 5.4 a-b.

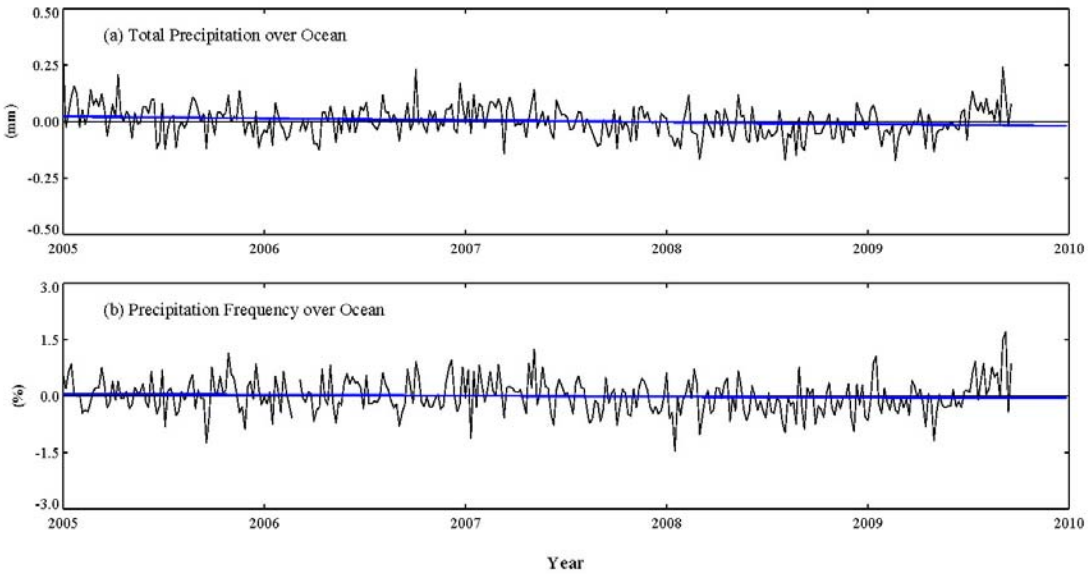

Figure 5.4: Same as in Fig. 5.3, but from heritage RR retrieval

Similarly, both CDR products display a decreasing trend during the same period of time. The only difference is the scale of change. As shown in Table 5.1, the heritage RR derived total precipitation decreases at only one third of the rate of the *IWP* derived precipitation. The statistical analysis also found that the 5 year mean precipitation from the *IWP* algorithm is also about one third higher than from the heritage algorithm, which indicates that the *RR* derived from *IWP* is generally larger than from the heritage *RR* retrieval.

However, it is also noteworthy that the rainfall rate is a high variance regional parameter, one which could dramatically change within minutes. The climate data record constructed from 5 years of F-16 SSMIS data might not be reliably reflect the reality, even though the T-test score given in Table 5.1 indicates that the climate change trends obtained from the time series are statistically significant.

Table 5.1: Statistical Analysis of Precipitation Climate Data Records

Parameter	Mean	Change Rate	T-test Score
Precipitation (heritage)	1.20 mm	-0.08±0.05 mm/decade	-3.45
Precipitation Frequency	9.71 %	-0.23±0.40 %/decade	-1.38
Precipitation (IWP)	1.97 mm	-0.27±0.07 mm/decade	-6.74
Precipitation Frequency	8.66 %	-1.53±0.45 %/decade	-9.01

In this chapter, rain rate was retrieved from ice cloud parameters and qualitatively compared to surface synthetic hourly precipitation observations from radar reflectivity and gauge measurements. Analysis results demonstrated that this scattering-base algorithm can improve rain rate accuracy, particularly for strong convections. Global oceanic precipitation climate data records were generated from 5-year (2005-2009) DMSP F-16 SSMIS data using this enhanced rain rate retrieval results. Comparison was made to that generated from heritage emission-base rain rate retrievals for the same period of time. Both climate change time series, even presented in different change rates, clearly showed decreasing trends in both the global oceanic precipitation amount and rainfall frequency between 2005 and 2009, which is also well consistent to what was obtained from inter-sensor calibrated DMSP SSM/I (F8-F15) generated climate data records (Sun *et al.* 2008; Yang *et al.* 2009). Our study has proved that DMSP SSMIS series data can safely be used in global climate change study if accurate inter-sensor calibration schema can be carefully applied and product retrieval algorithms are successfully improved.

Chapter 6: Summary and Future Work

6.1 Summary

The joint Air Force and Navy Defense Meteorological Satellite Program launched the newly developed SSMIS in 2005, which contains the functionality of the heritage DMSP sounder (SSM/T and SSM/T-2) and imager (SSMI/I) in a single integrated conically scanning instrument with additional channels to profile the mesosphere. It is the first time that atmospheric soundings can be derived by a sole instrument with a constant viewing geometry. This benefit encourages the satellite data user to develop/improve previous scattering based retrieval algorithms because the scan view angle is considered a major issue in the development of those algorithms.

Preliminary assessments of SSMIS TDR data show that numerous calibrations related issues were still not identified until the satellite was flying in space. These issues include the main reflector face frequency dependent emission, warm/cold calibration count solar intrusions, and calibration nonlinearity errors. The microwave instrument calibration/validation group has proposed a set of corrections to fix those problems successfully. Model simulations and product evaluations prove that SSMIS data can be safely used for retrieving microwave based hydrometer parameters generated after such effective calibration preprocessor corrections are applied to the TDR data.

Retrievals of hydrological and surface parameters from F-16 SSMIS are demonstrated herein using the SSM/I algorithms. The products are compared for three months of data from both sensors. All F-16 TDRs have been reprocessed as the experimental TDR data for these tests. The procedure for TDR to SDR correction and the remapping of F-16 SSMIS imaging channels to F-15 SSM/I is based on the algorithm from NRL. After the reprocessing of F-16 SSMIS data, contamination of measured antenna temperatures, direct solar radiation, cross polarization coupling, and antenna spillover are effectively reduced. The F-16 SSMIS to SSM/I imaging channel remapping is a critical step in our study because it allows us to apply the same algorithms for the two instruments. Both satellites' orbit data have been processed to a 1/3 degree grid. Because of the time difference between DMSP F-15 and F-16 is about 30 minutes, most retrieval products will not be affected much by such a small time variation except for the rain rate, which is relatively more temporally variable. Products comparisons, including TPW, LWP, LST, Snow Cover, Sea Ice Cover, and land emissivity have been presented here. It is shown that the retrievals from both sensors demonstrate a high level of agreement with each other. Both the relatively small mean bias and standard deviation prove that F-16 SSMIS data can be successfully used for retrievals previously developed for use with SSM/I channels only.

As the 150 GHz and three double side-band 183.31 GHz channels are also integrated into SSMIS, a new algorithm is then developed to potentially retrieve the ice particle effective diameter and ice water path from the DMSP SSMIS high resolution environmental unit measurements at 91.655 GHz and 183.31±6.6 GHz.

For a single cloud layer, the upwelling and downwelling radiances are nearly independent of the cloud layer temperature and are directly linked to the cloud droplets scattering parameter Ω, which can be derived from the brightness temperatures at the bottom and top of the ice cloud. The ratio of the scattering parameters measured at 91.655 GHz and 183.31±6.6 GHz is directly used to estimate the ice particle effective diameter D_e when ice particlse are near millimeter or precipitation droplet size. The relationship between particle effective diameter and the scattering parameter is established by assuming a gamma size distribution for ice particles. The *IWP* is retrieved from the particle effective diameter and scattering parameter with a known ice particle bulk density.

Several major sources in the retrieval errors of particle effective diameter and ice water path are identified and analyzed. The uncertainties in estimating the ice cloud base brightness temperature using the lower frequency channels may contribute up to 10% of retrieval errors in the ice particle effective diameter. The particle effective diameter retrieval is not sensitive to the exponential parameter in the gamma size distribution. The uncertainties of the *IWP* retrievals come from the errors of estimating the ice cloud base temperature and particle effective diameter. Particularly, an overestimate of the particle effective diameter will lead to an underestimate of *IWP* for smaller particles, and a lower cloud temperature depression will introduce more errors in *IWP* retrievals.

The algorithm is tested under severe weather conditions of hurricanes and multicell storms. The derived rainfall rates are also analyzed and shown to provide very comparable results to those retrieved by the NOAA heritage rate algorithm using

measurements at lower than 91.655 GHz. This new algorithm shows less contamination over coastal areas where the heritage algorithm has more errors, and hence the new method can be potentially useful to generate better operational products for the DMSP SSMIS series instruments. It is also worthwhile to note that the ice particle bulk density displays wide variations, though this is a critical parameter in the *IWP/De* retrieval; so, any method that provides more accurate values for this parameter will greatly help to improve the retrieval quality.

The *RR* derived from *IWP* is also used to construct a global total precipitation analysis between 50^{O}S and 65^{O}N. The global total precipitation anomaly time series from SSMIS since January 2005 is generated to demonstrate a satellite data-based global hydrological series for climate studies. For comparison purposes, the same time series generated from the heritage *RR* algorithm was also produced in parallel. Both anomaly time series present a decreasing trend in the global precipitation amount, which indicates that the earth is in a global drought phase. Meanwhile, the rainfall coverage is also decreasing during the past 5 years, which further supports the above conclusion. The application of new algorithms for use in global climate change studies is critical, as the climate science community believes that satellite data will continue to play a central role in future studies.

6.2 Future Work

It is noteworthy that there are several assumptions which have been made to simplify the complicated radiative transfer equations. In practice, cases of multiple

layer ice clouds are quite common. The estimation of the ice cloud base temperature in those cases may be difficult, but is critical for more accurate *IWP* retrievals.

The ice particle shape is assumed to be spherical so that the scattering properties used in the equations are relatively stable in the forward model simulations. However, several studies have shown that ice clouds are actually composed of a number of different ice particle shapes, which each have quite different scattering properties in reality. Therefore, improvements of the particle scattering scheme may significantly improve retrieval quality.

In this study, the satellite measurements at 91.655 and 183.31±6.6 GHz are used for the retrievals. However, it is well known that 183.31±6.6 GHz is quite sensitive to the water vapor content, which is actually always closely associated with precipitating cold clouds. Because of the uncertainty provided by the water vapor emission effects, the scattering signals may be strongly and nonlinearly offset so that smaller scattering parameters will be obtained. With the retrieval algorithm presented here, a smaller scattering parameter at 183.31±6.6 GHz indicates that the ice particle effective diameter retrieval will be bigger, and so will the value for the *IWP*. The presence of an upward bias in the retrieval for *IWP* can be indirectly concluded by examining the global precipitation time series, where it is observed that the *IWP*-derived global precipitation is larger than that from the heritage rainfall rate algorithm. Fortunately, 150 GHz measurements are also available aboard SSMIS, which can serve as another candidate for use in this retrieval algorithm. As a channel with less water vapor contamination, measurements at 150 GHz may help to improve the ice cloud parameter retrieval quality.

The process of evaluating the retrieved products for precipitating clouds is very important to guide development on how to improve the algorithms. The best evaluation sources are *in situ* observations from field campaigns, which are not available since the launch of SSMIS. Another method is to compare the results to reliable retrievals from other instruments or algorithms, such as CloudSAT. Unfortunately, the huge time gap between CloudSAT and F-16 SSMIS orbits (more than 6 hours) makes such a comparison unreliable for evaluation of such temporally sensitive products. Therefore, other indirect evaluation methods, such as via radar observations, may allow the best comparisons possible.

Appendix

The derivation of angular dependent two-stream model solutions:

From Radiative Transfer Equation,

$$\mu \frac{dI(\tau,\mu)}{d\tau} = I(\tau,\mu) - \frac{\omega_0}{2}\int_{-1}^{1} P(\mu,\mu')I(\tau,\mu')d\mu' - (1-\omega_0)B_v ,$$

where Phase function $P(\mu,\mu') = \sum_{l=0}^{\infty}(2l+1)\chi_l L_l(\mu)L_l(\mu')$, and $L_l(\mu)$ are Legendre polynomials and $\chi_l = \frac{1}{2}\int_{-1}^{1} d\mu' P(\mu,\mu')L_l(\mu')$ is the *l*-th moment of the phase function. For the two-stream model, the zero-th and first moments are retained. At the zero-th moment ($l = 0$), $\chi_l = \chi_0 = 1$, which is the normalization of the phase function (from the definition of phase function) and $L_l(\mu) = L_0(\mu) = 1$. At the first moment, $\chi_l = \chi_1 = g$ refers to an asymmetry factor and $L_l(\mu) = L_1(\mu) = \mu$. Therefore, the phase function can be written as:

$P(\mu,\mu') = 1 + 3g\mu\mu'$.

By Gaussian Quadrature, an integration function can be approximated by a discrete summation, such as by

$$\int_{-1}^{1} f(x)dx = \sum_{i=-n}^{n} a_i f(x_i) .$$

So then, the scattering term in radiative function can be written as

$$\int_{-1}^{1} P(\mu,\mu')I(\tau,\mu')d\mu' = \sum_{i=-n}^{n} a_i P(\mu,\mu_i)I(\tau,\mu_i) ,$$

where a_i is the weight and $a_i = a_{-i}$, $\mu_{-j} = -\mu_j$ and $\sum_{i=-n}^{n} a_i = 2$.

Using the two-stream model phase function, we obtain

$$\int_{-1}^{1} P(\mu,\mu')I(\tau,\mu')d\mu' = \sum_{i=-n}^{n} a_i(1+3g\mu\mu_i)I(\tau,\mu_i).$$

For the simplest case, let $n=1$, $a_{-1} = a_1 = 1$ and $\mu_{-1} = -\mu_1$; the scattering term is changed to

$$\begin{aligned}\sum_{i=-n}^{n} a_i(1+3g\mu\mu_i)I(\tau,\mu_i) &= a_{-1}(1+3g\mu\mu_{-1})I(\mu_{-1}) + a_1(1+3g\mu\mu_1)I(\mu_1)\\ &= (1+3g\mu\mu_{-1})I(\mu_{-1}) + (1+3g\mu\mu_1)I(\mu_1)\\ &= (1-3g\mu\mu_1)I(-\mu_1) + (1+3g\mu\mu_1)I(\mu_1)\\ &= I(\tau,-\mu_1) + I(\tau,\mu_1) + 3g\mu\mu_1\left[I(\tau,\mu_1) - I(\tau,-\mu_1)\right]\end{aligned}.$$

Introducing the Eddington approximation:

$$I(\tau,\mu) = I_0(\tau) + \mu I_1(\tau).$$

Then,

$$I(\tau,-\mu_1) + I(\tau,\mu_1) = I_0(\tau) - \mu_1 I_1(\tau) + I_0(\tau) + \mu_1 I_1(\tau) = 2I_0(\tau)$$

$$3g\mu\mu_1\left[I(\tau,\mu_1) - I(\tau,-\mu_1)\right] = 3g\mu\mu_1\left[I_0(\tau) + \mu_1 I_1(\tau) - I_0(\tau) + \mu_1 I_1(\tau)\right] = 2\times 3g\mu\mu_1 I_1(\tau)$$

By replacing corresponding terms in the radiative transfer equations and separating the upwelling and downward parts:

$$\mu_1 \frac{dI(\tau,\mu_1)}{d\tau} = I(\tau,\mu_1) - \frac{\omega_0}{2}\left[a_{-1}(\chi_0 + 3\chi_1\mu\mu_1)I(\tau,\mu_{-1}) + a_1(\chi_0 + 3\chi_1\mu\mu_1)I(\tau,\mu_1)\right] - (1-\omega_0)B_v$$

and

$$-\mu_1 \frac{dI(\tau,-\mu_1)}{d\tau} = I(\tau,-\mu_1) - \frac{\omega_0}{2}\left[a_{-1}(\chi_0 + 3\chi_1\mu\mu_1)I(\tau,-\mu_{-1}) + a_1(\chi_0 + 3\chi_1\mu\mu_1)I(\tau,-\mu_1)\right] - (1-\omega_0)B_v$$

.

If we apply $a_{-1} = a_1 = 1$, $\mu_{-1} = -\mu_1 = \frac{1}{\sqrt{3}}$ (averaged value), $\chi_0 = 1$, and $\chi_1 = g$, the previous equations can be changed to:

$$\mu_1 \frac{dI(\tau,\mu_1)}{d\tau} = I(\tau,\mu_1) - \frac{\omega_0}{2}\left[(1-\chi_1\mu_1^2)I(\tau,-\mu_1) + (1+\chi_1\mu_1^2)I(\tau,\mu_1)\right] - (1-\omega_0)B_v$$

and

$$-\mu_1 \frac{dI(\tau,\mu_1)}{d\tau} = I(\tau,-\mu_1) - \frac{\omega_0}{2}\left[(1-\chi_1\mu_1^2)I(\tau,\mu_1) + (1+\chi_1\mu_1^2)I(\tau,-\mu_1)\right] - (1-\omega_0)B_v .$$

Combining both $I(\tau,\mu_1)$ and $I(\tau,-\mu_1)$ terms on the right hand side, we obtain:

$$\mu_1 \frac{dI(\tau,\mu_1)}{d\tau} = \left[1 - \frac{\omega_0}{2}(1+\chi_1\mu_1^2)\right]I(\tau,\mu_1) - \frac{\omega_0}{2}(1-\chi_1\mu_1^2)I(\tau,-\mu_1) - (1-\omega_0)B_v$$

and

$$-\mu_1 \frac{dI(\tau,\mu_1)}{d\tau} = -\frac{\omega_0}{2}(1-\chi_1\mu_1^2)I(\tau,\mu_1) + \left[1 - \frac{\omega_0}{2}(1+\chi_1\mu_1^2)\right]I(\tau,-\mu_1) - (1-\omega_0)B_v .$$

Let us define the following terms, and insert $\chi_1 = g$ and $\mu_{-1} = -\mu_1 = \frac{1}{\sqrt{3}}$, arriving at:

$$h_1 = 1 - \frac{\omega_0}{2}(1+\chi_1\mu_1^2) = 1 - \frac{\omega_0}{2}(1+g) = 1 - \omega_0\left(1 - \frac{1-g}{2}\right) = 1 - \omega_0(1-b),$$

$$h_2 = -\frac{\omega_0}{2}(1-\chi_1\mu_1^2) = -\omega_0\left(\frac{1-g}{2}\right) = -\omega_0 b .$$

Taking the derivative of τ, the two-stream radiative transfer functions can be written as:

$$\mu_1 \frac{d^2I(\tau,\mu_1)}{d\tau^2} = h_1 \frac{dI(\tau,\mu_1)}{d\tau} + h_2 \frac{dI(\tau,-\mu_1)}{d\tau}$$

and

$$-\mu_1 \frac{d^2I(\tau,-\mu_1)}{d\tau^2} = h_2 \frac{dI(\tau,\mu_1)}{d\tau} + h_1 \frac{dI(\tau,-\mu_1)}{d\tau} .$$

To resolve the above functions, we use $\frac{dI(\tau,\mu_1)}{d\tau}$ and $\frac{dI(\tau,-\mu_1)}{d\tau}$ from the above equations to obtain:

$$\mu_1 \frac{d^2I(\tau,\mu_1)}{d\tau^2} = \frac{h_1}{\mu_1}\left[h_1 I(\tau,\mu_1) + h_2 I(\tau,-\mu_1) - (1-\omega_0)B_v\right] - \frac{h_2}{\mu_1}\left[h_2 I(\tau,\mu_1) + h_1 I(\tau,-\mu_1) - (1-\omega_0)B_v\right]$$

and

$$-\mu_1 \frac{d^2I(\tau,-\mu_1)}{d\tau^2} = \frac{h_2}{\mu_1}\left[h_1 I(\tau,\mu_1) + h_2 I(\tau,-\mu_1) - (1-\omega_0)B_v\right] - \frac{h_1}{\mu_1}\left[h_2 I(\tau,\mu_1) + h_1 I(\tau,-\mu_1) - (1-\omega_0)B_v\right]$$

.

Rearranging the equations, then:

$$\frac{d^2I(\tau,\mu)}{d\tau^2} = \frac{h_1^2 - h_2^2}{\mu^2} I(\tau,\mu) - \frac{h_1 - h_2}{\mu^2}(1-\omega_0)B_v$$

and

$$\frac{d^2I(\tau,-\mu)}{d\tau^2} = \frac{h_1^2 - h_2^2}{\mu^2} I(\tau,-\mu) - \frac{h_1 - h_2}{\mu^2}(1-\omega_0)B_v .$$

Define $\kappa_1^2 = \frac{h_1^2 - h_2^2}{\mu^2}$, $\kappa_2^2 = \frac{h_1 - h_2}{\mu^2}(1-\omega_0)$ and we have:

$$\frac{d^2I(\tau,\mu)}{d\tau^2} = \kappa_1^2 I(\tau,\mu) - \kappa_2^2 B_v$$

and

$$\frac{d^2I(\tau,-\mu)}{d\tau^2} = \kappa_1^2 I(\tau,-\mu) - \kappa_2^2 B_v .$$

To obtain the solutions to the above, we define the general solution and specific solution by:

$$I(\tau,\mu) = C^+ e^{\kappa\tau} + D^+ e^{-\kappa\tau} + \frac{\kappa_2^2}{\kappa_1^2} B_v = C^+ e^{\kappa\tau} + D^+ e^{-\kappa\tau} + B_v$$

and

$$I(\tau,-\mu) = C^{-}e^{\kappa\tau} + D^{-}e^{-\kappa\tau} + \frac{\kappa_2^2}{\kappa_1^2}B_v = C^{-}e^{\kappa\tau} + D^{-}e^{-\kappa\tau} + B_v,$$

where

$$\frac{\kappa_2^2}{\kappa_1^2} = \frac{(h_1-h_2)(1-\omega_0)}{h_1^2-h_2^2} = \frac{1-\omega_0}{h_1+h_2} = \frac{1-\omega_0}{1-\omega_0} = 1 \Rightarrow \kappa_1^2 = \kappa_2^2 = \kappa^2 = \frac{(1-\omega_0)(1-\omega_0 g)}{\mu^2} \text{ (eigen}$$

value).

Substituting back into the equations, we get:

$$C^{+}\kappa e^{\kappa\tau} - D^{+}\kappa e^{-\kappa\tau} = \frac{h_1}{\mu}\left(C^{+}e^{\kappa\tau} + D^{+}e^{-\kappa\tau} + B_v\right) + \frac{h_2}{\mu}\left(C^{-}e^{\kappa\tau} + D^{-}e^{-\kappa\tau} + B_v\right) - \frac{1-\omega_0}{\mu}B_v$$

and

$$C^{-}\kappa e^{\kappa\tau} - D^{-}\kappa e^{-\kappa\tau} = -\frac{h_1}{\mu}\left(C^{+}e^{\kappa\tau} + D^{+}e^{-\kappa\tau} + B_v\right) - \frac{h_1}{\mu}\left(C^{-}e^{\kappa\tau} + D^{-}e^{-\kappa\tau} + B_v\right) + \frac{1-\omega_0}{\mu}B_v.$$

Combining C^{+}, C^{-}, D^{+}, and D^{-}, and setting $\tau = 0$ at TOA for the above equations:

$$(\kappa - \frac{h_1}{\mu})C^{+} - (\kappa + \frac{h_1}{\mu})D^{+} = \frac{h_2}{\mu}C^{-} + \frac{h_2}{\mu}D^{-} + \frac{(h_1+h_2)-(1-\omega_0)}{\mu}B_v$$

and

$$\frac{h_2}{\mu}C^{+} + \frac{h_2}{\mu}D^{+} = -(\kappa + \frac{h_1}{\mu})C^{-} + (\kappa - \frac{h_1}{\mu})D^{-} - \frac{(h_1+h_2)-(1-\omega_0)}{\mu}B_v$$

because $h_1 + h_2 = 1-\omega_0$, $\frac{(h_1+h_2)-(1-\omega_0)}{\mu}B_v = 0$ in the above equations.

Now let us define $m_1 = \kappa - \frac{h_1}{\mu}$, $m_2 = \kappa + \frac{h_1}{\mu}$ and $m_3 = \frac{h_2}{\mu}$, so the above equations can

be written as:

$$m_1C^{+} - m_2D^{+} = m_3C^{-} + m_3D^{-}$$

and

$$m_3 C^+ + m_3 D^+ = -m_2 C^- + m_1 D^- .$$

After combining the two equations together, we obtain

$$(m_1 + m_3)C^+ + (m_3 - m_2)D^+ = (m_3 - m_2)C^- + (m_1 + m_3)D^- .$$

And next we obtain the relationships:

$$C^+ = \frac{m_3 - m_2}{m_3 + m_1} C^- = \frac{h_2 - h_1 - \kappa\mu}{h_2 - h_1 + \kappa\mu} C^- = \frac{h_2 - h_1 - \sqrt{h_1^2 - h_2^2}}{h_2 - h_1 + \sqrt{h_1^2 - h_2^2}} C^- = \frac{1 + \sqrt{\frac{1-\omega_0}{1-\omega_0 g}}}{1 - \sqrt{\frac{1-\omega_0}{1-\omega_0 g}}} C^- = \frac{1+\varpi}{1-\varpi} C^-$$

and

$$D^+ = \frac{m_3 + m_1}{m_3 - m_2} D^- = \frac{h_2 - h_1 + \kappa\mu}{h_2 - h_1 - \kappa\mu} D^- = \frac{h_2 - h_1 + \sqrt{h_1^2 - h_2^2}}{h_2 - h_1 - \sqrt{h_1^2 - h_2^2}} D^- = \frac{1 - \sqrt{\frac{1-\omega_0}{1-\omega_0 g}}}{1 + \sqrt{\frac{1-\omega_0}{1-\omega_0 g}}} D^- = \frac{1-\varpi}{1+\varpi} D^-$$

,

with similarity parameter $\varpi = \sqrt{\frac{1-\omega_0}{1-\omega_0 g}}$.

Let

$$C^+ = K\frac{1+\varpi}{2} = Kv\,,\ C^- = K\frac{1-\varpi}{2} = Ku$$

and $D^+ = H\frac{1-\varpi}{2} = Hu\,, D^- = H\frac{1+\varpi}{2} = Hv$, where *K* and *H* are ratios.

Inserting terms back into the radiative transfer equation solutions (general plus specific), we get:

$$I(\tau,\mu) = Kve^{\kappa\tau} + Hue^{-\kappa\tau} + B_v\,,$$

$$I(\tau,-\mu) = Kue^{\kappa\tau} + Hve^{-\kappa\tau} + B_v .$$

At the top of the cloud ($\tau = \tau_0$), the downward radiation is

$$Kue^{\kappa\tau_0} + Hve^{-\kappa\tau_0} = I(\tau_0,-\mu) - B_v = I_0 ,$$

while at the bottom of cloud ($\tau = \tau_1$), upward radiation is

$$Kve^{\kappa\tau_1} + Hue^{-\kappa\tau_1} = I(\tau_1,\mu) - B_v = I_1 .$$

Then, solving the above equations:

$$H = \frac{I_0 ve^{\kappa\tau_1} - I_1 ue^{\kappa\tau_0}}{v^2 e^{\kappa(\tau_1-\tau_0)} - u^2 e^{-\kappa(\tau_1-\tau_0)}}$$

and

$$K = \frac{I_1 ve^{-\kappa\tau_0} - I_0 ue^{-\kappa\tau_1}}{v^2 e^{\kappa(\tau_1-\tau_0)} - u^2 e^{-\kappa(\tau_1-\tau_0)}} .$$

Substituting both *H* and *K* back into the solutions, finally:

$$I(\tau,\mu) = \frac{I_1(v^2 e^{\kappa(\tau-\tau_0)} - u^2 e^{-\kappa(\tau-\tau_0)}) + I_0(uve^{\kappa(\tau_1-\tau)} - uve^{-\kappa(\tau_1-\tau)})}{v^2 e^{\kappa(\tau_1-\tau_0)} - u^2 e^{-\kappa(\tau_1-\tau_0)}} + B_v$$

and

$$I(\tau,-\mu) = \frac{I_1(uve^{\kappa(\tau-\tau_0)} - uve^{-\kappa(\tau-\tau_0)}) + I_0(v^2 e^{\kappa(\tau_1-\tau)} - u^2 e^{-\kappa(\tau_1-\tau)})}{v^2 e^{\kappa(\tau_1-\tau_0)} - u^2 e^{-\kappa(\tau_1-\tau_0)}} + B_v$$

.

At the top of the cloud, $\tau = \tau_0 = 0$. There, we have:

$$I(\tau,\mu) = \frac{I_1(v^2 - u^2) + I_0 uv(e^{\kappa\tau_1} - e^{-\kappa\tau_1})}{v^2 e^{\kappa\tau_1} - u^2 e^{-\kappa\tau_1}} + B_v$$

and

$$I(\tau,-\mu) = \frac{I_0(v^2 - u^2) + I_1 uv(e^{\kappa\tau_1} - e^{-\kappa\tau_1})}{v^2 e^{\kappa\tau_1} - u^2 e^{-\kappa\tau_1}} + B_v .$$

For typical cirrus clouds (thin layer), $\kappa\tau_1 < 1$.

By applying a Taylor series expansion, $e^{\kappa\tau_1} \approx 1+\kappa\tau_1$ and $e^{-\kappa\tau_1} \approx 1-\kappa\tau_1$ to the first equation we have

$$I(\tau,\mu) = \frac{I_1(v^2-u^2) + I_0 uv(2\kappa\tau_1)}{v^2(1+\kappa\tau_1) - u^2(1-\kappa\tau_1)} + \frac{B_v(v^2-u^2) + B_v(v^2+u^2)\kappa\tau_1}{v^2(1+\kappa\tau_1) - u^2(1-\kappa\tau_1)}.$$

Because $I_1 = I(\tau_1,\mu) - B_v$ and $I_0 = I(\tau_0,-\mu) - B_v$, the above solution can be changed to

$$I(\tau,\mu) = \frac{I(\tau_1,\mu)(v^2-u^2) + I(\tau_0,-\mu)uv(2\kappa\tau_1) + B_v\kappa\tau_1(v-u)^2}{v^2(1+\kappa\tau_1) - u^2(1-\kappa\tau_1)}.$$

The same is true for $I(\tau,-\mu)$, so we get

$$I(\tau,-\mu) = \frac{I(\tau_0,-\mu)(v^2-u^2) + I(\tau_1,\mu)uv(2\kappa\tau_1) + B_v\kappa\tau_1(v-u)^2}{v^2(1+\kappa\tau_1) - u^2(1-\kappa\tau_1)}.$$

As we defined earlier, $u = \frac{1-\varpi}{2}$ and $v = \frac{1+\varpi}{2}$, so then $v^2-u^2 = \varpi$, $(v-u)^2 = \varpi^2$, $vu = \frac{1-\varpi^2}{4}$, and $v^2+u^2 = \frac{1+\varpi^2}{2}$.

Using these in the above two solutions:

$$I(\tau,\mu) = \frac{I(\tau_1,\mu)\varpi + I(\tau_0,-\mu)\kappa\tau_1\frac{1-\varpi^2}{2} + B_v\kappa\tau_1\varpi^2}{\varpi + \kappa\tau_1\frac{1+\varpi^2}{2}}$$

and

$$I(\tau,-\mu) = \frac{I(\tau_0,-\mu)\varpi + I(\tau_1,\mu)\kappa\tau_1\frac{1-\varpi^2}{2} + B_v\kappa\tau_1\varpi^2}{\varpi + \kappa\tau_1\frac{1+\varpi^2}{2}}.$$

Let us define a scattering parameter, $\Omega = \frac{\kappa\tau_1}{2\varpi} = \frac{\kappa\tau_1}{2}\sqrt{\frac{1-\omega_0 g}{1-\omega_0}}$, so then:

$$I(\tau,\mu) = \frac{I(\tau_1,\mu) + I(\tau_0,-\mu)\Omega(1-\varpi^2) + 2B_v\Omega\varpi^2}{1+\Omega(1+\varpi^2)}$$

and

$$I(\tau,-\mu) = \frac{I(\tau_0,-\mu) + I(\tau_1,\mu)\Omega(1-\varpi^2) + 2B_v\Omega\varpi^2}{1+\Omega(1+\varpi^2)}.$$

For small ice particles (compared to the wavelength), $\Omega\varpi^2 << 1$ and at TOA, $I(\tau_0,-\mu) \to 0$ due to the very low cosmic background radiation, then we simplify solutions to:

$I(0,\mu) \approx \frac{I(\tau_1,\mu)}{1+\Omega} \Rightarrow T_b^+ = \frac{T_b(\tau_1,\mu)}{1+\Omega} \Rightarrow \Omega = \frac{T_b(\tau_1,\mu) - T_b^+}{T_b^+}$ (Upward radiation at top of cloud)

and

$I(\tau,-\mu) \approx \frac{I(\tau_1,\mu)\Omega}{1+\Omega}$ (Downward radiation at τ),

and for thin cirrus clouds we may assume $I(\tau_0,-\mu) \sim B_v \sim I(\tau_1,\mu)$.

Therefore, the above solutions can be simplified to:

$$I(\tau,\mu) \approx \frac{I(\tau_1,\mu) + I(\tau_0,-\mu)\Omega}{1+\Omega}$$

and

$$I(\tau,-\mu) \approx \frac{I(\tau_0,-\mu) + I(\tau_1,\mu)\Omega}{1+\Omega}.$$

Furthermore, if it is assumed that $\Omega << 1$ then $I(\tau_0,-\mu)\Omega \sim 0$, $I(\tau_1,\mu)\Omega \sim 0$ and $I(\tau_0,-\mu) \sim I(\tau_1,\mu) \sim B_v$.

The solutions can then be written as:

$$I(\tau,\mu) \approx \frac{I(\tau_1,\mu)+2B_v\Omega\varpi^2}{1+\Omega(1+\varpi^2)} \Rightarrow T_b = \frac{T_b(\tau_1,\mu)+2T_{Cloud}\Omega\varpi^2}{1+\Omega(1+\varpi^2)}$$

and

$$I(\tau,-\mu) \approx \frac{I(\tau_0,-\mu)+2B_v\Omega\varpi^2}{1+\Omega(1+\varpi^2)} \Rightarrow T_b = \frac{T_b(\tau_0,-\mu)+2T_{Cloud}\Omega\varpi^2}{1+\Omega(1+\varpi^2)}.$$

Please note that this assumption will be invalid for large optical thickness.

Because the similarity parameter $\varpi << 1$,

$$T_b^+ = \frac{T_b(\tau_1,\mu)}{1+\Omega} \Rightarrow \Omega = \frac{T_b(\tau_1,\mu)-T_b^+}{T_b^+},$$

where,

T_b^+: Upwelling brightness temperature obtained by satellite;

$T_b(\tau_1,\mu)$: Incident brightness temperature (91GHz and 150GHz) at bottom of cloud layer, obtained by empirical relationship from lower frequencies (19GHz, 22GHz, and 37GHz);

$T_b(\tau_0,-\mu)$: Incident brightness temperature at top of cloud layer;

T_{Cloud}: cloud physical temperature in K;

g: Asymmetry factor in phase function.

Bibliography

Ackerman, S. A. and W. L. Smith, 1990: Inferring Cloud Microphysical Properties from High Resolution Spectral Measurements inthe 8-13 μm Window Region. *the Seventh Conference on Atmpspheric Radiation*, Boston, Mass, 6-8.

Adler, R. F., R. A. Mack, N. Prasad, H. Y. M. Yeh, and I. M. Hakkarinen, 1990: Aircraft Microwave Observations and Simulations of Deep Convection from 18 to 183 GHz. Part I: Observations. *Journal of Atmospheric and Oceanic Technology*, **7,** 377-391.

Alishouse, J. C., S. A. Snyder, J. Vongsathorn, and R. R. Ferraro, 1990: Determination of Oceanic Total Precipitable Water from the SSM/I. *IEEE Transactions on Geoscience and Remote Sensing*, **28,** 811-816.

Arking, A. and J. D. Childs, 1985: Retrieval of Cloud Cover Parameters from Multispectral Satellite Images. *J Appl Meteorol*, **24,** 322-333.

Barkstrom, B. R., 1984: The earth radiation budget experiment (ERBE). *Bulletin of the American Meteorological Society*, **65,** 1170-1185.

Barkstrom, B. R. and G. L. Smith, 1985: The earth radiation budget experiment: Science and implementation. *Reviews of Geophysics*, **24,** 379-390.

Bennartz, R. and P. Bauer, 2003: Sensitivity of microwave radiances at 85-183 GHz to precipitating ice particles. *Radio Science*, **38,** MAR 40-41 - MAR 40-48.

Brown, P. R. A., A. J. Illingworth, A. J. Heymsfield, G. M. McFarquhar, K. A. Browning, and M. Gosset, 1995: The Role of Spaceborne Millimeter-Wave Radar in the Global Monitoring of Ice Cloud. *J Appl Meteorol*, **34,** 2346-2366.

Buehler, S. A., C. Jimenez, K. F. Evans, P. Eriksson, B. Rydberg, A. J. Heymsfield, C. J. Stubenrauch, U. Lohmann, C. Emde, and V. O. John, 2007: A concept for a satellite mission to measure cloud ice water path, ice particle size, and cloud altitude. *Quarterly Journal of the Royal Meteorological Society*, **133,** 109-128.

Cao, C., F. Weng, M. Goldberg, X. Wu, H. Xu, and P. Ciren, 2005: Intersatellite Calibration of Polar-orbiting Radiometers using the SNO/SCO Method. Storming Media.

Chang, F.-L. and Z. Li, 2005a: A Near-Global Climatology of Single-Layer and Overlapped Clouds and Their Optical Properties Retrieved from Terra/MODIS Data Using a New Algorithm. *Journal of Climate*, **18,** 4752-4771.

——, 2005b: A New Method for Detection of Cirrus Overlapping Water Clouds and Determination of Their Optical Properties. *J Atmos Sci*, **62,** 3993-4009.

Cofield, R. E. and P. C. Stek, 2006: Design and field-of-view calibration of 114-660-GHz optics of the Earth observing system microwave limb sounder. *IEEE Transactions on Geoscience and Remote Sensing*, **44,** 1166-1181.

Deeter, M. N. and K. F. Evans, 2000: A novel ice-cloud retrieval algorithm based on the millimeter-wave imaging radiometer (MIR) 150-and 220-GHz channels. *J Appl Meteorol*, **39,** 623-633.

Donovan, D. P. and A. C. A. P. v. Lammeren, 2001: Cloud effective particle size and water content profile retrievals using combined lidar and radar observations. Part 1: Theory and simulations. *Journal of Geophysical Research*, **106,** 27425-27448.

Donovan, D. P. and Coauthors, 2001: Cloud effective particle size and water content profile retrievals using combined lidar and radar observations. Part 2: Comparison with IR radiometer and in situ measurements of ice clouds. *Journal of Geophysical Research*, **106,** 27449-27464.

Evans, K. F. and G. L. Stephens, 1995a: Microwave Radiative-Transfer through Clouds Composed of Realistically Shaped Ice Crystals. Part I: Single Scattering Properties. *J Atmos Sci*, **52,** 2041-2057.

——, 1995b: Microwave Radiative-Transfer through Clouds Composed of Realistically Shaped Ice Crystals. Part II: Remote-Sensing of Ice Clouds. *J Atmos Sci*, **52,** 2058-2072.

Evans, K. F., S. J. Walter, A. J. Heymsfield, and M. N. Deeter, 1998: Modeling of submillimeter passive remote sensing of cirrus clouds. *J Appl Meteorol*, **37,** 184-205.

Evans, K. F., J. R. Wang, P. E. Racette, G. Heymsfield, and L. Li, 2005: Ice Cloud Retrievals and Analysis with the Compact Scanning Submillimeter Imaging Radiometer and the Cloud Radar System during CRYSTAL FACE. *J Appl Meteorol*, **44,** 839-859.

Ferraro, R. R. and G. F. Marks, 1995: The Development of SSM/I Rain-Rate Retrieval Algorithms Using Ground-Based Radar Measurements. *Journal of Atmospheric and Oceanic Technology*, **12,** 755-770.

Ferraro, R. R., F. Weng, N. C. Grody, L. Zhao, H. Meng, C. Kongoli, P. Pellegrino, S. Qiu, and C. Dean, 2005: NOAA operational hydrological products derived from the Advanced Microwave Sounding Unit. *IEEE Transactions on Geoscience and Remote Sensing*, **43,** 1036-1049.

Flamant, P. H., V. Noel, H. Chepfer, M. Quante, O. Danne, V. Giraud, and J. Pelon, 2000: Particle sizes in cirrus cloud during the Carl'99 campaign: 29 April and

14 May case studies. *Int. Radiation Symp.*, St. Petersburg, Russia, Research Institute of Physics.

Fu, Q. and K. N. Liou, 1993: Parameterization of the Radiative Properties of Cirrus Clouds. *J Atmos Sci*, **50,** 2008-2025.

Fulton, R. A., J. P. Breidenbach, D. J. Seo, D. A. Miller, and T. O'Bannon, 1998: The WSR-88D rainfall algorithm. *Weather and Forecasting*, **13,** 377-395.

Gasiewski, A. J., 1992: Numerical sensitivity analysis of passive EHF and SMMW channels to tropospheric water vapor, clouds, and precipitation. *IEEE Transactions on Geoscience and Remote Sensing*, **30,** 859-870.

Giraud, V., J. C. Buriez, Y. Fouquart, F. Parol, and G. Seze, 1997: Large-Scale Analysis of Cirrus Clouds from AVHRR Data: Assessment of Both a Microphysical Index and the Cloud-Top Temperature. *J Appl Meteorol*, **36,** 664-675.

Greenwald, T. J. and S. A. Christopher, 2002: Effect of cold clouds on satellite measurements near 183 GHz. *Journal of Geophysical Research-Atmospheres*, **107,** 4170.

Grody, N. C., 1991: Classification of Snow Cover and Precipitation Using the Special Sensor Microwave Imager. *Journal of Geophysical Research-Atmospheres*, **96,** 7423-7435.

Grody, N. C. and A. N. Basist, 1996: Global identification of snowcover using SSM/I measurements. *IEEE Transactions on Geoscience and Remote Sensing*, **34,** 237-249.

Hahn, C. J., S. G. Warren, J. London, R. M. Chervin, and R. Jenne, 1982: Atlas of Simultaneous Occurrence of Different Cloud Types over the Ocean. *NCAR Tech. Note TN-201+STR*, **209-212**.

Hakkarinen, I. M. and R. F. Adler, 1988: Observations of precipitating convective systems at 92 and 183 GHz: Aircraft results. *Meteorology and Atmospheric Physics*, **38,** 164-182.

Heymsfield, A. J., S. Lewis, A. Bansemer, J. Iaquinta, L. M. Miloshevich, M. Kajikawa, C. Twohy, and M. R. Poellot, 2002: A general approach for deriving the properties of cirrus and stratiform ice cloud particles. *J Atmos Sci*, **59,** 3-29.

Heymsfield, G. M., J. M. Shepherd, S. W. Bidwell, W. C. Boncyk, I. J. Caylor, S. Ameen, and W. S. Olson, 1996: Structure of Florida Thunderstorms Using

High-Altitude Aircraft Radiometer and Radar Observations. *J Appl Meteorol*, **35,** 1736-1762.

Inoue, T., 1985: On the temperature and effective emissivity determination of semi-transparent cirrus clouds by bi-spectral measurements in the 10 μm window region. *Journal of the Meteorological Society of Japan*, **63,** 88-99.

Intrieri, J. M., W. L. Eberhard, and G. L. Stephens, 1990: Preliminary comparison of lidar and radar backscatter as a means of assessing cirrus radiative properties. *Seventh Conf. on Atmospheric Radiation*, San Francisco, CA, Amer. Meteor. Soc., 354-356.

King, M. D., W. P. Menzel, Y. J. Kaufman, D. Tanr, B. C. Gao, S. Platnick, S. A. Ackerman, L. A. Remer, R. Pincus, and P. A. Hubanks, 2003: Cloud and aerosol properties, precipitable water, and profiles of temperature and water vapor from MODIS. *IEEE Transactions on Geoscience and Remote Sensing*, **41,** 442-458.

Kummerow, C., W. S. Olson, L. Giglio, N. Center, and M. D. Greenbelt, 1996: A simplified scheme for obtaining precipitation and verticalhydrometeor profiles from passive microwave sensors. *IEEE Transactions on Geoscience and Remote Sensing*, **34,** 1213-1232.

Kummerow, C., Y. Hong, W. S. Olson, S. Yang, R. F. Adler, J. McCollum, R. Ferraro, G. Petty, D. B. Shin, and T. T. Wilheit, 2001: The evolution of the Goddard Profiling Algorithm (GPROF) for rainfall estimation from passive microwave sensors. *J Appl Meteorol*, **40,** 1801-1820.

Kunkee, D. B., S. D. Swadley, G. A. Poe, Y. Hong, and M. F. Werner, 2008: Special Sensor Microwave Imager Sounder (SSMIS) Radiometric Calibration Anomalies—Part I: Identification and Characterization. *IEEE Transactions on Geoscience and Remote Sensing*, **46,** 1017-1033.

Liou, K. N., 1986: Influence of Cirrus Clouds on Weather and Climate Processes - a Global Perspective. *Monthly Weather Review*, **114,** 1167-1199.

Liou, K. N., S. C. Ou, Y. Takano, F. P. J. Valero, and T. P. Ackerman, 1990: Remote Sounding of the Tropical Cirrus Cloud Temperature and Optical Depth Using 6.5 and 10.5 μm Radiometers during STEP. *J Appl Meteorol*, **29,** 716-726.

Liou, K. N., Y. Gu, Q. Yue, and G. McFarguhar, 2008: On the correlation between ice water content and ice crystal size and its application to radiative transfer and general circulation models. *Geophysical Research Letters*, **35**.

Liu, C. and A. J. Illingworth, 2000: Toward more accurate retrievals of ice water content from radar measurements of clouds. *J Appl Meteorol*, **39,** 1130-1146.

Liu, G. and J. A. Curry, 1998: Remote sensing of ice water characteristics in tropical clouds using aircraft microwave measurements. *J Appl Meteorol*, **37,** 337-355.

——, 1999: Tropical ice water amount and its relations to other atmospheric hydrological parameters as inferred from satellite data. *J Appl Meteorol*, **38,** 1182-1194.

——, 2000: Determination of ice water path and mass median particle size using multichannel microwave measurements. *J Appl Meteorol*, **39,** 1318-1329.

Liu, G. and Y. Fu, 2001: The Characteristics of Tropical Precipitation Profiles as Inferred from Satellite Radar Measurements. *Journal of the Meteorological Society of Japan*, **79,** 131-143.

Mace, G. G., T. P. Ackerman, P. Minnis, and D. F. Young, 1998: An examination of cirrus cloud characteristics using data from millimetre wave radar and lidar: The 24 April SUCCESS case study. *Geophysical Research Letters*, **25,** 1133-1136.

Mace, G. G., E. E. Clothiaux, and T. P. Ackerman, 2001: The composite characteristics of cirrus clouds: Bulk properties revealed by one year of continuous cloud radar data. *Journal of Climate*, **14,** 2185-2203.

Mace, G. G., Y. Zhang, S. Platnick, M. D. King, P. Minnis, and P. Yang, 2005: Evaluation of cirrus cloud properties derived from MODIS data using cloud properties derived from ground-based observations collected at the ARM SGP site. *J Appl Meteorol*, **44,** 221-240.

Markus, T. and D. J. Cavalieri, 2000: An enhancement of the NASA Team sea ice algorithm. *IEEE Transactions on Geoscience and Remote Sensing*, **38,** 1387-1398.

Markus, T. and S. T. Dokken, 2002: Evaluation of late summer passive microwave Arctic sea ice retrievals. *IEEE Transactions on Geoscience and Remote Sensing*, **40,** 348-356.

Minnis, P., K. N. Liou, and Y. Takano, 1993a: Inference of Cirrus Cloud Properties Using Satellite-observed Visible and Infrared Radiances. Part I: Parameterization of Radiance Fields. *J Atmos Sci*, **50,** 1279-1304.

Minnis, P., P. W. Heck, and D. F. Young, 1993b: Inference of Cirrus Cloud Properties Using Satellite-observed Visible and Infrared Radiances. Part II: Verification of Theoretical Cirrus Radiative Properties. *J Atmos Sci*, **50,** 1305-1322.

Mo, T., 2007: Postlaunch Calibration of the NOAA-18 Advanced Microwave Sounding Unit-A. *IEEE Trans. Geosci. Remote Sens.*, **45,** 1928-1937.

Mugnai, A. and E. A. Smith, 1988: Radiative Transfer to Space through a Precipitating Cloud at Multiple Microwave Frequencies. Part I: Model Description. *J Appl Meteorol*, **27,** 1055-1073.

Muller, B. M., H. E. Fuelberg, and X. Xiang, 1994: Simulations of the effects of water vapor, cloud liquid water, and ice on AMSU moisture channel brightness temperatures. *J Appl Meteorol*, **33,** 1133-1154.

Nakajima, T. and M. D. King, 1990: Determination of the Optical Thickness and Effective Particle Radius of Clouds from Reflected Solar Radiation Measurements. Part I: Theory. *J Atmos Sci*, **47,** 1878-1893.

Okamoto, H., S. Iwasaki, M. Yasui, H. Horie, H. Kuroiva, and H. Kumagai, 2003: An algorithm, for retrieval of cloud microphysics using 91-GHz cloud radar and lidar. *Journal of Geophysical Research*, **108,** 4226.

Ou, S. C., K. N. Liou, W. M. Gooch, and Y. Takano, 1993: Remote sensing of cirrus cloud parameters using advanced very-high-resolution radiometer 3. 7-and 10. 9- μm channels. *Applied Optics*, **32,** 2171-2180.

Ou, S. C., K. N. Liou, Y. Takano, N. X. Rao, Q. Fu, A. J. Heymsfield, L. M. Miloshevich, B. Baum, and S. A. Kinne, 1995: Remote Sounding of Cirrus Cloud Optical Depths and Ice Crystal Sizes from AVHRR Data: Verification Using FIRE II IFO Measurements. *J Atmos Sci*, **52,** 4143-4158.

Ou, S. C., K. N. Liou, M. D. King, and S. C. Tsay, 1999: Remote Sensing of Cirrus Cloud Parameters Based on a 0.63-3.7 μm Radiance Correlation Technique Applied to AVHRR Data. *Geophysical Research Letters*, **26,** 2439-2440.

Petty, G. W., 1994: Physical retrievals of over-ocean rain rate from multichannel microwave imagery. Part I: Theoretical characteristics of normalized polarization and scattering indices. *Meteorology and Atmospheric Physics*, **54,** 79-99.

——, 1995: Frequencies and Characteristics of Global Oceanic Precipitation from Shipboard Present-Weather Report. *Bulletin of the American Meteorological Society*, **76,** 1593-1616.

Platnick, S., M. D. King, S. A. Ackerman, W. P. Menzel, B. A. Baum, J. C. Riedi, and R. A. Frey, 2003: The MODIS cloud products: algorithms and examples from Terra. *IEEE Transactions on Geoscience and Remote Sensing*, **41,** 459-473.

Pollinger, W. and P. Wendling, 1984: A bispectral method for the height determination of optically thin ice clouds. *Contrib. Atmos. Phys*, **57,** 269-281.

Racette, P., R. F. Adler, J. R. Wang, A. J. Gasiewski, D. M. Jakson, and D. S. Zacharias, 1996: An Airborne Millimeter-Wave Imaging Radiometer for

Cloud, Precipitation, and Atmospheric Water Vapor Studies. *Journal of Atmospheric and Oceanic Technology*, **13,** 610-619.

Read, W. G., A. Lambert, J. Bacmeister, R. E. Cofield, L. E. Christensen, D. T. Cuddy, W. H. Daffer, B. J. Drouin, E. Fetzer, and L. Froidevaux, 2007: Aura Microwave Limb Sounder upper tropospheric and lower stratospheric H_2O and relative humidity with respect to ice validation. *Journal of Geophysical Research-Atmospheres*, **112,** D24S35.

Riedi, J., M. Doutriaux-Boucher, P. Goloub, and P. Couvert, 2000: Global distribution of cloud top phase from POLDER/ADEOS I. *Geophysical Research Letters*, **27,** 1707-1710.

Rogers, R. R. and M. K. Yau, 1989: *A short course in cloud physics*. third ed. Vol. 113, *International Series in Natural Philosphy*, Elsevier.

Rolland, P., K. N. Liou, M. D. King, S. C. Tsay, and G. M. McFarquhar, 2000: Remote sensing of optical and microphysical properties of cirrus clouds using Moderate-Resolution Imaging Spectroradiometer channels- Methodology and sensitivity to physical assumptions. *Journal of Geophysical Research*, **105,** 11.

Rossow, W. B. and R. A. Schiffer, 1991: ISCCP Cloud Data Products. *Bulletin of the American Meteorological Society*, **72,** 2-20.

Rossow, W. B. and Y. C. Zhang, 1995: Calculation of surface and top of atmosphere radiative fluxes from physical quantities based on ISCCP data sets 2. Validation and first results. *Journal of Geophysical Research-Atmospheres*, **100,** 1167-1197.

Rossow, W. B. and R. A. Schiffer, 1999: Advances in Understanding Clouds from ISCCP. *Bulletin of the American Meteorological Society*, **80,** 2261-2287.

Rubinstein, I. G., D. M. Nazarenko, and S. Tam, 1994: Passive microwave systems. *Remote Sensing of Sea Ice and Icebergs***,** 177-257.

Runheng, H. and K. N. Liou, 1984: Remote sounding of the cirrus optical depth and temperature from 3.7 and 11 micrometer windows. *Advances in Atmospheric Sciences*, **1,** 150-164.

Sassen, K. and Z. Wang, 2002: Cirrus cloud ice water content radar algorithm evaluation using an explict cloud microphysics model. *J Appl Meteorol*, **41,** 620-628.

Shokr, M. and T. Markus, 2006: Comparison of NASA Team2 and AES-York ice concentration algorithms against operational ice charts from the Canadian ice service. *IEEE Transactions on Geoscience and Remote Sensing*, **44,** 2164-2175.

Slingo, A. and J. M. Slingo, 1988: The response of a general circulation model to cloud longwave radiative forcing. I: Introduction and initial experiments. *Quarterly Journal of the Royal Meteorological Society*, **114,** 1027-1062.

Smith, E. A. and A. Mugnai, 1988: Radiative Transfer to Space through a Precipitating Cloud at Multiple Microwave Frequencies. Part II: Results and Analysis. *J Appl Meteorol*, **27,** 1074-1091.

Spencer, R. W., W. S. Olson, R. Z. Wu, D. W. Martin, J. A. Weinman, and D. A. Santek, 1983: Heavy Thunderstorms Observed over Land by the Nimbus-7 Scanning Multichannel Microwave Radiometer. *J. Climate Appl. Meteor.*, **22,** 1041-1046.

Spencer, R. W., H. M. Goodman, and R. E. Hood, 1989: Precipitation Retrieval over Land and Ocean with the SSM/I: Identification and Characteristics of the Scattering Signal. *Journal of Atmospheric and Oceanic Technology*, **6,** 254-273.

Stephens, G. L. and P. J. Webster, 1981: Clouds and Climate - Sensitivity of Simple Systems. *J Atmos Sci*, **38,** 235-247.

Stephens, G. L., A. Slingo, M. J. Webb, P. J. Minnett, P. H. Daum, L. Kleinman, I. Wittmeyer, and D. A. Randall, 1994: Observations of the Earth's Radiation Budget in relation to atmospheric hydrology 4. Atmospheric column radiative

cooling over the world's oceans. *Journal of Geophysical Research-Atmospheres*, **99,** 18,585-518,604.

Stephens, G. L., D. G. Vane, R. J. Boain, G. G. Mace, K. Sassen, Z. Wang, A. j. Illingworth, E. J. O'Connor, W. B. Rossow, S. L. Durden, S. D. Miller, R. T. Austin, A. Benedetti, and C. Mitrescu, 2002: The CloudSat Mission and The A-Train. *Bulletin of the American Meteorological Society*, **83**.

Stephens, G. L., 2005: Cloud Feedbacks in the Climate System: A Critical Review. *Journal of Climate*, **18,** 237-273.

Stephens, G. L. and C. D. Kummerow, 2007: The remote sensing of clouds and precipitation from space: A review. *J Atmos Sci*, **64,** 3742-3765.

Stephens, G. L., D. G. Vane, S. Tanelli, E. Im, S. Durden, M. Rokey, D. Reinke, P. Partain, G. G. Mace, R. Austin, T. L'Ecuyer, J. Haynes, M. Lebsock, K. Suzuki, D. Waliser, D. Wu, J. Kay, A. Gettelman, Z. Wang, and R. Marchand, 2008: CloudSat mission: Performance and early science after the first year of operation. *Journal of Geophysical Research*, **113,** D00A18.

Stone, R. S., G. L. Stephens, C. M. R. Platt, and S. Banks, 1990: The Remote Sensing of Thin Cirrus Cloud Using Satellites, Lidar and Radiative Transfer Theory. *J Appl Meteorol*, **29,** 353-366.

Stubenrauch, C. J., R. Holz, A. Chedin, D. L. Mitchell, and A. J. Baran, 1999: Retrieval of cirrus ice crystal sizes from 8. 3 and 11. 1 μm emissivities determined by the improved initialization inversion of TIROS-N Operational Vertical Sounder observations. *Journal of Geophysical Research*, **104,** 31793-31808.

Su, H., W. G. Read, J. H. Jiang, J. W. Waters, D. L. Wu, and E. J. Fetzer, 2006a: Enhanced positive water vapor feedback associated with tropical deep convection: New evidence from Aura MLS. *GEOPHYSICAL RESEARCH LETTERS*, **33,** L05709.

Su, H., D. E. Waliser, J. H. Jiang, J. Li, W. G. Read, J. W. Waters, and A. M. Tompkins, 2006b: Relationships of upper tropospheric water vapor, clouds and SST: MLS observations, ECMWF analyses and GCM simulations. *GEOPHYSICAL RESEARCH LETTERS*, **33,** L22802.

Sun, N., F. Weng, R. Ferraro, and S. Yang, 2008: Prototype Demonstration of Special Sensor Microwave Imager (SSM/I) Based Climate Data Records (CDRs) During 1992-2006 After Inter-sensor Calibration. *The 4th International Precipitation Working Group Conference*, Beijing, China.

Sun, N. and F. Weng, 2008: Evaluation of Special Sensor Microwave Imager/Sounder (SSMIS) Environmental Data Records. *IEEE Transactions on Geoscience and Remote Sensing*, **46,** 1006-1016.

——, 2009: Retrieval of Cloud Ice Water Path from Special Sensor Microwave Imager/Sounder (SSMIS). *Journal of Applied Meteorology and Climate*, **Submitted**.

Szejwach, G., 1982: Determination of Semi-Transparent Cirrus Cloud Temperature from Infrared Radiances: Application to METEOSAT. *J Appl Meteorol*, **21,** 384-393.

Tian, L. and J. A. Curry, 1989: Cloud Overlap Statistics. *Journal of Geophysical Research-Atmospheres*, **94,** 9925-9935.

Tinel, C., J. Testud, J. Pelon, R. J. Hogan, A. Protat, J. Delanoe, and D. Bouniol, 2005: The Retrieval of Ice-Cloud Properties from Cloud Radar and Lidar Synergy. *J Appl Meteorol*, **44,** 860-875.

Uttal, U., R. A. Kropfli, W. L. Ebenhard, and J. M. Intrieri, 1990: Observations of mid-latitude, continental cirrus clouds using a 3.2 cm radar: Comparisons with 10.6 μm lidar observations. *Seventh Conf. on Atmospheric Radiation*, San Francisco, CA, Amer. Meteor. Soc., 349-353.

Vivekanandan, J., J. Turk, and V. N. Bringi, 1991: Ice Water Path Estimation and Characterization Using Passive Microwave Radiometry. *J Appl Meteorol*, **30,** 1407-1421.

Wang, J. R., G. Liu, J. D. Spinhirne, P. Racette, and W. D. Hart, 2001: Observations and retrievals of cirrus cloud parameters using multichannel millimeter-wave radiometric measurements. *Journal of Geophysical Research*, **106**.

Warren, S. G., C. J. Hahn, and J. London, 1985: Simultaneous Occurrence of Different Cloud Types. *Journal of Climate and Applied Meteorology*, **24,** 658-667.

Weinman, J. A. and J. L. Schols, 1992: A model to retrieve precipitation rate profiles from airborne radar and radiometer measurements. *Specialist Meeting on Microwave Radiometry and Remote Sensing Applications*, E. R. Westwater, Ed., National Technical Information Service, 460-466.

Weng, F., 1992: A multi-layer discrete-ordinate method for vector radiative transfer in a vertically-inhomogeneous, emitting and scattering atmosphere. Part I: Theory. *J. Quant. Spectrosc. Radiat. Transfer*, **47,** 19-33.

Weng, F. and N. C. Grody, 1994: Retrieval of Cloud Liquid Water Using the Special Sensor Microwave Imager (SSM/I). *Journal of Geophysical Research-Atmospheres*, **99,** 25535-25551.

Weng, F., N. C. Grody, R. Ferraro, A. Basist, and D. Forsyth, 1997: Cloud liquid water climatology from the special sensor microwave/imager. *Journal of Climate*, **10,** 1086-1098.

Weng, F. and N. C. Grody, 1998: Physical retrieval of land surface temperature using the special sensor microwave imager. *Journal of Geophysical Research-Atmospheres*, **103,** 8839-8848.

——, 2000: Retrieval of ice cloud parameters using a microwave imaging radiometer. *J Atmos Sci*, **57,** 1069-1081.

Weng, F., B. Yan, and N. C. Grody, 2001: A microwave land emissivity model. *Journal of Geophysical Research-Atmospheres*, **106,** 20115-20123.

Weng, F., L. Zhao, R. R. Ferraro, G. Poe, X. Li, and N. C. Grody, 2003: Advanced microwave sounding unit cloud and precipitation algorithms. *Radio Science*, **38,** 8068-8079.

Wentz, F. J. and R. W. Spencer, 1998: SSM/I Rain Retrievals within a Unified All-Weather Ocean Algorithm. *J Atmos Sci*, **55,** 1613-1627.

Wielicki, B. A., B. R. Barkstrom, E. F. Harrison, R. B. Lee Iii, G. Louis Smith, and J. E. Cooper, 1996: Clouds and the Earth's Radiant Energy System (CERES): An Earth Observing System Experiment. *Bulletin of the American Meteorological Society*, **77,** 853-868.

Wilheit, T. T., A. T. C. Chang, J. L. King, E. B. Rodgers, R. A. Nieman, B. M. Krupp, A. S. Milman, J. S. Stratigos, and H. Siddalingaiah, 1982: Microwave

Radiometric Observations Near 19.35, 92 and 183 GHz of Precipitation in Tropical Storm Cora. *J Appl Meteorol*, **21,** 1137-1145.

Wu, D. L., J. H. Jiang, and C. P. Davis, 2006: EOS MLS cloud ice measurements and cloudy-sky radiative transfer model. *IEEE Transactions on Geoscience and Remote Sensing*, **44,** 1156-1165.

Wu, D. L., J. H. Jiang, W. G. Read, R. T. Austin, C. P. Davis, A. Lambert, G. L. Stephens, D. G. Vane, and J. W. Waters, 2008: Validation of the Aura MLS cloud ice water content measurements. *Journal of Geophysical Research-Atmospheres*, **113,** D15S10.

Wu, M. L. C., 1987: A Method for Remote Sensing the Emissivity, Fractional Cloud Cover and Cloud Top Temperature of High-Level, Thin Clouds. *J Appl Meteorol*, **26,** 225-233.

Wu, R. and J. A. Weinman, 1984: Microwave radiances from precipitating clouds containing aspherical ice, combined phase, and liquid hydrometeors. *Journal of Geophysical Research*, **89,** 7170-7178.

Yan, B. and F. Weng, 2003: Ten-year (1993-2002) time-series of microwave land emissivity. *Microwave Remote Sensing of the Atmosphere and Environment III. Edited by Kummerow, Christian D.; Jiang, JingShang; Uratuka, Seiho. Proceedings of the SPIE*, **4894,** 278-286.

——, 2007: Recalibration of Special Sensor Microwave Imager and Sounder lower atmospheric sounding channels. *Journal of Atmospheric and Oceanic Technology*.

——, 2008: Intercalibration Between Special Sensor Microwave Imager/Sounder and Special Sensor Microwave Imager. *IEEE Transactions on Geoscience and Remote Sensing*, **46,** 984-995.

Yang, S., F. Weng, N. Sun, and B. Yan, 2009: Special Sensor Microwave Imager (SSM/I) Intersensor Calibration and Impact on Total Precipitable Water/Precpitation Trend. *Journal of Applied Meteorology and Climatology*.

Zhang, Y. C., W. B. Rossow, and A. A. Lacis, 1995: Calculation of surface and top of atmosphere radiative fluxes from physical quantities based on ISCCP data sets 1. Method and sensitivity to input data uncertainties. *Journal of Geophysical Research-Atmospheres*, **100,** 1149-1165.

Zhao, L. and F. Weng, 2002: Retrieval of ice cloud parameters using the advanced microwave sounding unit. *J Appl Meteorol*, **41,** 384-395.